E.T.S.Ingeniería Industrial

Department of Mechanical Engineering and Fluid Mechanics

Numerical and experimental study of the hydrodynamic efficiency of a tidal energy extraction system and its effect on the re-suspension of sea bed sediments

Thesis submitted by Daniel Cebrián Robles for the degree of Doctor at University of Malaga

2014

Doctoral program: Biogeochemical dynamics of flows and their applications

Supervised by:

Joaquín Ortega Casanova

Ramón Fernández Feria

E.T.S.Ingeniería Industrial

Departamento de Ingeniería Mecánica y Mecánica de fluidos

Estudio numérico y experimental de la eficiencia hidrominámica de un sistema de extracción de las energías de las mareas y su efecto en la resuspensión de los sedimentos en el fondo marino.

Tesis realizada por Daniel Cebrián Robles para el título de doctor por la Universidad de Málaga

2014

Programa de doctorado: Dinámica de los flujos biogeoquímicos y sus aplicaciones

Dirigida por:

Joaquín Ortega Casanova

Ramón Fernández Feria

Dr. D. Joaquín Ortega Casanova y Dr. D. Ramón Fernández Feria

Departamento de Ingeniería Mecánica y Mecánica de Fluidos de la Universidad de Málaga

CERTIFICAN

Que D. Daniel Cebrián Robles, ha realizado bajo su dirección la tesis doctoral titulada NUMERICAL AND EXPERIMENTAL STUDY OF THE HYDRODYNAMIC EFFICIENCY OF A TIDAL ENERGY EXTRACTION SYSTEM AND ITS EFFECT ON THE RE-SUSPENSION OF SEA BED SEDIMENTS que se recoge en la presente memoria, cumpliendo todos los requisitos legales para optar al grado INTERNACIONAL de DOCTOR, por lo que autoriza su lectura y defensa pública en la Escuela Técnica Superior de Ingenieros Industriales de la Universidad de Málaga.

Y para que así conste y tenga los efectos oportunos, firmo el presente certificado en

Málaga, a 11 de Julio de 2014

Dr. D. Joaquín Ortega Casanova   Dr. D. Ramón Fernández Feria

Dedicado a
mi familia
Dedicated to
my family

Acknowledgments

Quiero empezar agradeciendo este trabajo a todas las personas que me han apoyado y aconsejado en estos años de duro trabajo.

En especial, a mi familia por haber estado desde el principio hasta el final animándome y ayudándome en las dificultades, sin ellos este trabajo no hubiera sido posible.

También quiero agradecerle la dedicación, la constancia, el apoyo y el conocimiento de mis directores de tesis Ramón Fernández Feria y Joaquín Ortega Casanova. Ellos han sido la pieza fundamental y la piedra angular de la tesis.

No me puedo olvidar de los compañeros de trabajo que me han informado y ayudado en aquellas dificultades durante el desarrollo de la tesis. Carlos del Pino Peñas por ponerme en contacto con personas interesantes y darme ánimo en los momentos oportunos; a Luís Parras Anguita por las numerosas charlas físicas e informáticas y el apoyo técnico; a José Velázquez Navarro por su buena y permanente disposición a apoyarme; a Sergio Pinazo Ortega por su apoyo inestimable en el canal hidráulico.

Al Ministerio de Educación por la beca de movilidad en Nottingham University.

Abstract

This work aims to contribute to the research being done on marine renewable energy of tidal currents. A device for capturing the energy of the tides through a set of sails moved by the stream has been chosen to design the best configuration of the blades and thus generate more power, trying not to erode the seabed and thereby harming the environment (TidalSail S.A., 2014). For this, we studied the aerodynamic of the sails as flat plates moved at different velocities U, against to the current velocity V, different separations between the flat plates, and different angles of insidence in relation to the current. The Reynolds number and the semi-aspect ratio of the plates were kept constants, $Re = 5.66 \cdot 10^4$ and $sAR = 3$ respectively. A numerical code validated with experimental results by Pelletier & Mueller (2000) was used in the numerical simulations. Two turbulent models have been considered and compared, the $k - \omega$ and $k - \epsilon$ models, finding that the $k - \omega$ model was the best reproducing the experimental data. A train of infinity sails, in cascade configuration, allowed to study and analyze the best aerodynamic configuration of the assembly.

In the second part of the thesis work, the scour generated by the flat plates and the current on the seabed has been simulated experimentally in a hydraulic channel, seeking for the optimal height that must be set so that the environmental impact is as low as possible. For this, the Reynolds number

was fixed at maximum achieved in the hydraulic channel to examine the impact of turbulence in the scour process. The available hydraulic channel had very small dimensions and did not permit the use of standard techniques for 3D surface reconstruction. For this reason, we have designed and implemented a methodology and a code in Matlab that allows to reconstruct 3D patterns by a series of projected lines in parallel on the surface to scan. Reconstruction of the submerged surface was obtained in actual dimensions. With this technique were measured the amount of sand that it is eroded, the volume of the generated dunes, the contour of the sand, the underwater 3D surface reconstruction and the surface profiles in different planes. This experimental study has been made for different heights of the flat plate from the seabed, h, and different angles of the flat plate with respect to the current, α, for a given Reynolds number (maximum allowed by the hydraulic channel), given width of the flat plate, and given type of sand.

Contents

List of Figures

XXII

List of Tables

Chapter 1

Introduction

1.1 Background

The marine energies have an important role in the renewable energies due to the fact that about 71 percent of the Earth's surface is water-covered, and the oceans hold about 96.5 percent of all Earth's water (U.S. Geological Survey, 2014). Furthermore, the vast and powerful ocean could have enough energy to meet worldwide demand for power many times over (Pelc & Fujita, 2002).

The general advantages of the renewable energies could be applied to the sea energy:

1. It contributes to respect and conserve natural resources for use in future generations and produces no residue difficult to treat (Ossai *et al.*, 2014).

2. They are native. There is a distinctive resource that can be used as renewable energy in each location (Droege, 2008).

3. It generates a energy independence for a country by using their own

energy resources and not depend on the raw material of other countries (Heide *et al.*, 2010).

4. The energy mix of all renewable energies can largely replace the fossil energy (Heide *et al.*, 2010; Droege, 2008).

5. These energies are seemingly endless for the human being.

However, there are some drawbacks that should be investigated:

1. There is an irregularity in the generation of renewable energy. There is not always wind, waves ... However, in the case of tidal energy considered in this work, the tides are predictable and there exist areas with constant ocean currents. In any case, the intermittency could be solved by the energy mix (Heide *et al.*, 2010).

2. The integration in the environment has to be considered to reduce the environmental impact: Whether noise, visual impact, risk to the wildlife, etc. (Shields *et al.*, 2009). In relation to this, the marine energy is the focus of researchers to improve the technologies ensuring that the new developed systems do not harm the marine environment (Pelc & Fujita, 2002).

3. They need specific sites, that is, certain resources are only found in certain locations.

Among all types of extraction energy systems from the ocean or sea, it is possible summarize them in five main areas:

1. Tidal energy. It is the energy that harness the rise and fall of sea level (C., 2003).

2. Energy of marine currents. Use of the kinetic energy of currents, including tidal currents. There is a difference between tidal energy in general and tidal current energy, and their relation is not the same in all sites: the first is related to the potential energy due to the vertical movement of the sea level (rise and fall), the second to the horizontal flow, generated by tides, which is very intense in certain places (C., 2003).

3. Ocean thermal energy. Harnessing of the thermal gradient between the surface and the seabed (Rajagopalan & Nihous, 2013).

4. Saline energy gradient. The difference in salt concentration of the water produces a movement whose energy can be extracted (Jia *et al.*, 2014).

5. Wave power. There are many techniques to extract the energy of the ocean waves (Fadaeenejad *et al.*, 2014).

Among all these, in this thesis it is studied a device that captures the kinetic energy of tidal currents. In theory, there is a dissipation of 3000 million kilowatts with the rise and fall of tides of which one third is generated in the shallow seas (C., 2003). The conversion of the kinetic energy of river or sea currents into electricity is commonly made by systems of turbines and other non-turbines devices (Khan *et al.*, 2009; Rourke *et al.*, 2010). Since tidal power has potential to play an important part in the future of sustainable energy, there are many research work to improve these systems, but most of these systems are proof-of-concept or part-system R&D stage (Roc *et al.*, 2014; Khan *et al.*, 2009).

1.2 Tidal Sail device

Figure 1.1: Sketch of the design of flat plate cascade (TidalSail S.A., 2014).

In this context, a Norwegian company has developed a new non-turbine device consisting of a cascade of 'sails' that are moved by the sea current in a fixed direction (see Fig. 1.1) to finally generate electricity (TidalSail S.A., 2014). The sails are linked to a rail that supports and allows movement in one direction, as shown in Fig. 1.2. Furthermore, the rail has three sides creating a equilateral triangle shape with mooring in every corner (see Fig. 1.3 for more details), so that it is more efficient with less space. The system has characteristics that make it advantageous over other similar devices for capturing energy from currents, such as (see TidalSail S.A., 2014, for details):

- The sails have a slow enough movement so that minimize the harm to the fauna. A problem that show up with turbine devices.

- Optimizing its design, it is possible to get much more flow power with a smaller area. Furthermore, the production plant is equals to 30 conventional turbines with a slow motion.

- The system is invisible, and thus no visual impact.

- The device weight against energy produced is much less than other systems

- The moving parts of the device have a corrosion treatments and lubricating that no harm the environment.

- The sails are auto cleaned, auto adjusted and operate very slowly.

- This compacted structure allows to extract energy not only from the sea but also from rivers.
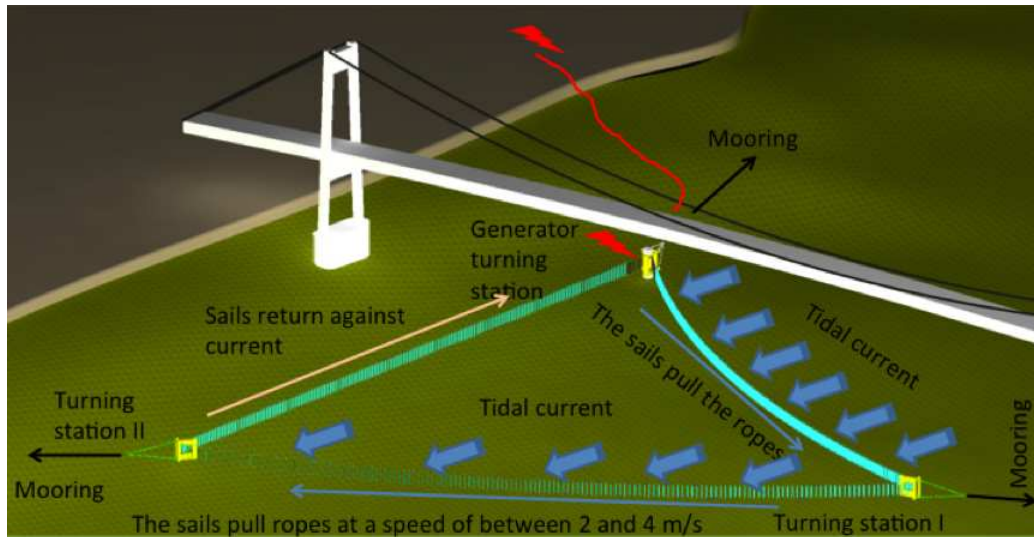
Figure 1.2: Sketch of the tidal energy system of the sail device of the Norwegian company TidalSail S.A. (2014).

Figure 1.3: Sketch of the mooring for the tidal energy system of the Norwegian company (TidalSail S.A., 2014).

Tidal Sails company has a small scale demonstrator operating in a stream outside Haugesund, Norway, with a nominal capacity of 28KW. But it is ready to scale up the range of several MW. The hydrodynamic forces work exactly the same in any scale (TidalSail S.A., 2014).

For the device be efficient and have a great potential for energy extraction some fundamental hydrodynamic problems on the drag and lift characteristics of a cascade of sails moving in a particular configuration in relation to the tidal current have to be analyzed. This is one of the objectives of the thesis, and for that the device is simplified to a cascade of flat plates moving perpendicularly to the flow of the tide, which is one of the configurations of greatest interest. For this study, a numerical code with appropriate turbulence model has been disaggregated.

A drawback of this device is its impact on the seabed, which can be eroded. Obviously, it is important an optimization of the height of the device and the anchors to the seabed to protect the marine environment and prevent sand particles have access to mobile parts that can get to damage the system. This is the second objective of the thesis, for which an experimental study

has been carried out in a sediment water channel.

1.3   Objectives and outline of this thesis

The chapters of this thesis are arranged as an introduction in the Chapter 1, where it is described the advantages and disadvantages the renewable energy systems that extract the tidal current energy and the objectives of this thesis.

The first part of this thesis is a review of previous works on aerodynamics of flat plates, which are used to study an optimal configuration of a device that extract the tidal energy in order to get the maximum power. For it, in the Chapter 2 is showed the aerodynamic coefficients for one, two, three and an infinite set of flat plates, in a cascade configuration for different angles and Reynolds number. For this study, different configurations are carried out using turbulent models for the simulation. In addition, $k - \epsilon$ and $k - \omega$ turbulence models are compared to use the best fits for experimental results. At the end, researching the optimal maximum power point for a cascade of flat plates. For this, the sails have to have a certain angle with respect to the direction of the current, a optimal velocity of the flat plates with respect to the current and the best separation between them.

The goal of the second part is a review of previous works on sedimentation and scour caused by objects on the seabed in order to know the best configuration that must to have the device that extract energy from the tidal without harm the environment. Seeking and applying the best methodology for the underwater three dimensional surface reconstruction that it resulted to be the creation of a new code and methodology for this purpose in the Chapter 3. With this code, the best configuration of the flat plates height with respect to the seabed has been researched for different angles of inci-

dence in relation to the current and different heights. For this, the Reynolds number and the semi-aspect ratio has been fixed to $Re = 5.66 \cdot 10^4$ and $sAR = 3$ respectively in the Chapter 4.

In the end there is a discussion of the conclusions and future possible works encouraged by this thesis, in the Chapter 5.

Chapter 2

Flat plates model of the tidal current energy converter

2.1   Introduction

In the Chapter 1 is possible to see the tidal energy systems in the Fig. 1.2. The aim of this chapter is to get the maximum power of the tidal current and for this it is necessary to use turbulent models in order to simulate the marine current, such as the experimental result of Fedoul *et al.* (2014). For that, it is used the turbulent libraries for incompressible flows of OpenFOAM. There are multiples methods that may be used (Ferziger & Perić, 1996). The first one is called Reynolds-average simulations (RAS) (Iaccarino *et al.*, 2003). The governing equations are solved as a average. The use of RAS resolve better the equations close to the wall in general. Large eddy simulation (LES) is another method that allow to resolve zones of great turbulences much better that the RAS method, so that may be improved the calculation of the equations in the computational domain (Sagaut & Drikakis, 2010). There are other models as Detached eddy simulation (DES) (Spalart, 2009)

and Direct numerical simulations (DNS) (Ferziger & Perić, 1996). The first of two is an hybrid method that operate between RAS and LES and the second one solves the equations of Navier-Stokes without turbulent model needing much longer of calculation. Among all of these methods is used RAS method because the aim is calculate the aerodynamic coefficients through the flat plate surface that give information of the forces that move the sails. OpenFOAM has different models for the RAS method, for instance, $k-\epsilon$ and $k-\omega$. The first one simulates the turbulence using two parameters k and ϵ and the results are really good in the flow study. In this work is analyzed the $k-\epsilon$ and $k-\omega$ methods to know which one is better for calculate the aerodynamic coefficients. The study of Pelletier & Mueller (2000) is used to validate the turbulent models that OpenFOAM has.

2.2   Formulation of the problem

The flow in the study of the aerodynamic coefficients is cosidered as an incompressible flow of a uniform (tidal or river) current of velocity $\mathbf{V}$ through a cascade of rectangular flat plates of chord length c and height b moving at a velocity $\mathbf{U}$ perpendicular to the current $\mathbf{V}$ (see Fig. 2.1(a)). The separation between the parallel plates is s and their incidence (stagger) angle γ. For the numerical simulations it is convenient to use a reference frame moving with the plates in which the x axis coincides with the direction of the relative velocity $\mathbf{W}$ (Fig. 2.1(b)). In this reference frame, the effective angle of attack in relation to the relative velocity is $\alpha = \gamma - \theta$, where θ is the angle between the current velocity $\mathbf{V}$ and the relative velocity $\mathbf{W}$.

The Reynolds number based on the current speed $V(\equiv |\mathbf{V}|)$ and the chord

length c,

$$Re = \frac{Vc}{\nu},\qquad\qquad(2.1)$$

where ν is the kinematic viscosity, will be fixed in all the numerical simulations to a characteristic value (see Sec. 2.3). For this given Re, we shall analyze the effect that the cascade speed U, the separation between plates s, and the stagger angle γ (or angle of attack α) have on the power extracted from the current. That is, we shall vary the non-dimensional parameters γ,

$$\xi \equiv \frac{U}{V} = \tan\theta,\ \text{ and } \sigma \equiv \frac{c}{s},\qquad\qquad(2.2)$$

to find out the values of these parameters that maximize the power extracted from the current for a given Re and for the configuration of Fig. 2.1(a) where the cascade moves perpendicularly to the current.

From a numerical point of view, we shall compute the total (pressure plus viscous) force $\mathbf{F}$ that the fluid exerts on a plate in the cascade when the incident flow speed is W and the angle
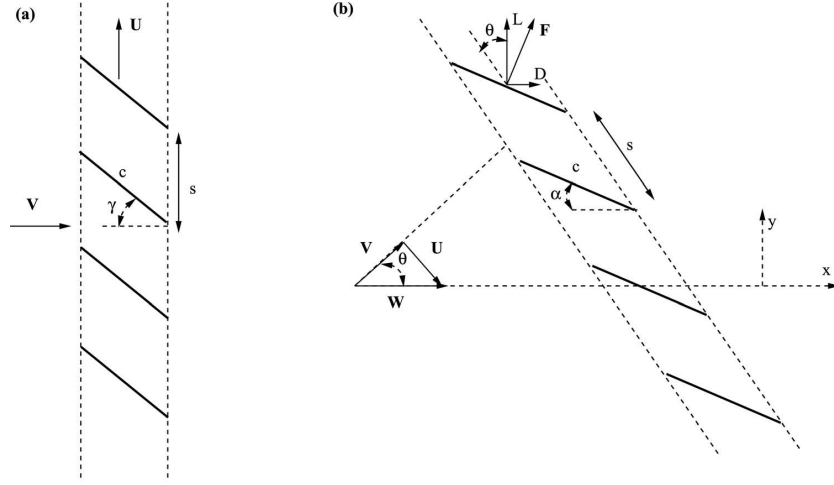
Figure 2.1: Sketch of the cascade of flat plates moving perpendicularly to the incident current $\mathbf{V}$ (a) and in the reference frame where the plates are steady and the relative velocity $\mathbf{W}$ is in the x-direction (b).

of attack is α; this force is decomposed in a "lift" component L and "drag" component D (see Fig. 2.1(b)). The Reynolds number based on W is related to (Eq. 2.1) by

$$Re_W \equiv \frac{Wc}{\nu} = \frac{Re}{\cos\theta} = Re\sqrt{1+\xi^2}. \tag{2.3}$$

For given Re_W, ξ, and solidity σ, we shall compute the nondimensional lift and drag coefficients,

$$C_L = \frac{L}{\frac{1}{2}\rho W^2 cb}, C_D = \frac{D}{\frac{1}{2}\rho W^2 cb}, \tag{2.4}$$

where ρ is the fluid density, for increasing values of α. This process will be repeated for different values of ξ (that also modifies Re_W, see Eq. 2.3) and σ. At the end, we will be interested on how these parameters affect the effective power extracted to the current, which is proportional to (see

Fig. 2.1(b))

$$P_U = (L\cos\theta - D\sin\theta)U. \tag{2.5}$$

We define the following power coefficient:

$$C_P \equiv \frac{P_U}{\frac{1}{2}\rho V^3 cb} = (C_L - \xi C_D)\xi\sqrt{1 + \xi^2}, \tag{2.6}$$

which will be optimized in relation to γ, ξ and σ for given Re and aspect ratio b/c. Note that C_L and C_D will be obtained from the numerical simulations as functions of α for different values of σ and ξ, being

$$\gamma = \alpha + \theta = \alpha + \arctan(\xi). \tag{2.7}$$

2.3 CFD methodology, equations and validation of the turbulent models

The governing equations are the Reynolds-averaged Navier-Stokes equations for an incompressible flow (constant density ρ), which can be written as

$$\nabla \cdot v = 0, \tag{2.8}$$

$$\frac{\partial \mathbf{v}}{\partial t} + \nabla \cdot (\mathbf{v}\mathbf{v}) = -\nabla p + \nabla \cdot [(\nu + \nu_t)(\nabla \mathbf{v} + (\nabla \mathbf{v})^T)], \tag{2.9}$$

where $\mathbf{v}$ is the mean velocity field, p the mean kinematic pressure (pressure divided by ρ) field, and ν_t is the kinematic eddy viscosity. For the numerical computations we used the open source CFD software package

OPENFOAM®, produced by OpenCFD Ltd, OpenFOAM (2014) with different two-equation turbulence models to compute ν_t,Rodi (2000),Cebeci (2004).

In particular, we used two different turbulence models: a Re-Normalisation Group (RNG) $k-\epsilon$ model Yakhot *et al.* (1992) and a Shear Stress Transport (SST) $k-\omega$ model, Menter (1994) both implemented in the OPENFOAM toolbox. The turbulence model equations and some numerical details are summarized in Appendix A. To select the best upstream values of the different turbulent variables for the present problem, together with the optimum computational grid, we simulated numerically the three-dimensional (3D) flow around a single flat plate with semispan aspect ratio(semi)-aspect ratio (sAR)=3,$Re_W = 8x10^4$ and different angles of attack (see Fig. 2.2) for the computational domain and mesh). The reasons for selecting this test case were that there exist accurate experimental data for the lift and drag coefficients obtained in a water tunnel by Pelletier & Mueller (2000) and that both the aspect ratio and the Reynolds number are in the range of interest for the tidal flow around the submerged sails in the device that motivated the present study TidalSail S.A. (2014). Smaller values of sAR, between 1 and 3, would also be appropriate. Note that the plane $z = 0$ (see Fig. 2.2) is a symmetry plane in the computational domain, both for the single flat plate and for the cascade, thus reducing to half the number of mesh nodes needed in the numerical computations. This configuration and the plate geometry coincide with those considered experimentally for a single plate Pelletier & Mueller (2000).
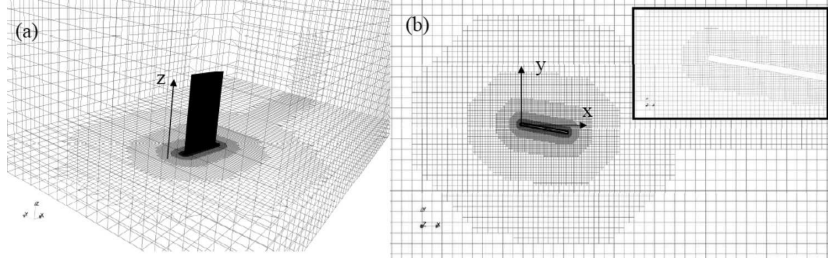
Figure 2.2: (a) General view of the computational domain and mesh with 3300198 cells used in the computations for the 3D flow around a flat plate with sAR=3 and angle of incidence $\alpha = 10^\text{o}$. (b) Plan view of the mesh with a detail of the leading edge of the plate. The dimensions of the computational domain are: $-3c \leq x \leq 7c$, $-c(3 + \sin c) \leq \text{y} \leq 3c$, and $0 \leq z \leq 4.5c$.

The boundary conditions used in the numerical computations are the following: In the inlet section $x = -3c$ (see Fig. 2.2) a uniform velocity in the $x-$direction was fixed, given by the selected Reynolds number, together with zero normal gradient (called "slip" condition in the OPENFOAM toolbox) for the pressure and fixed given values for the turbulent parameters. These upstream values of the turbulent parameters were varied to best fit the numerical results (see Table 2.1 and discussion below). In the outlet section, far downstream the plate ($x = 7c$), the pressure was set constant to its reference value (zero) and "inlet/outlet" conditions were used for the velocity and turbulent parameters. On the upper ($z = 4.5c$) and lateral surfaces (see Fig. 2.2) slip conditions were used for all the variables, while symmetry conditions were used on the lower surface ($z = 0$) where the flat plate is anchored. Finally, at the solid wall surfaces of the flat plate the velocity was set to zero, a slip condition was used for the pressure, and several specific wall conditions, implemented in the OPENFOAM toolbox and using standard wall functions, were used for k, ϵ and ω in the different models (see

the Appendix for these and other computational details). To generate the computational mesh we used the OPENFOAM "snappyHexMesh" program, with the imported form of the flat plate (see inset in Fig. 2.2(b)), which was previously generated using MATLAB. To solve the equations, we used the "GAMG—Generalised geometric-algebraic multi-grid" solver for the pressure, and the "smoothSolver" for the remaining variables, both implemented in the OPENFOAM toolbox OpenFOAM (2014). They are based on iterative methods for sparse linear systems Saad (2003).

Most of the reported computations were made in a computer cluster with 5 nodes and up to 22 parallel processors managed by the Linux Ubuntu server 10.04. Not all the nodes have the same characteristics, so that there existed a great variety of computational performances when using different combinations of the number of nodes and the number of parallel processors. It suffices to say here that the computation speed for a typical case reported below was increased almost 13 times when using all the 5 nodes with 22 parallel processors, in relation to just one 64-bit processor Intel(R) Core(TM) 2CPU 6600 at 2.66 GHz and 2.99GB of RAM.

To check the accuracy of the numerical results against the experimental data cited above we selected different meshes, and several upstream values of the turbulent kinetic energy (k_∞), dissipation (ϵ_∞), and specific dissipation rate (ω_∞) in the two turbulence models. In particular, for each set of upstream turbulent parameters considered (about five sets for each turbulence model), and for several angles of attack, a grid independent study was conducted using meshes with increasing resolution (see below). The numerical results converged appropriately in most cases, but the agreement of these converged numerical results with the experimental ones depended on the set of turbulent parameters used. To simplify the presentation of this compar-

Case	Number of Mesh cells	Turbulent model Parameter values	CPU time (h) $\delta t(s)$
1	983941	RNG $-k-\epsilon$	42.6
		$k_\infty = 0.0074, \epsilon_\infty = 0.032$	10^{-2}
2	3300198	RNG $-k-\epsilon$	206.8
		$k_\infty = 0.0074, \epsilon_\infty = 0.032$	6×10^{-3}
3	3300198	RNG $-k-\epsilon$	171.4
		$k_\infty = 0.096, \epsilon_\infty = 0.00552$	7×10^{-3}
4	5208203	RNG $-k-\epsilon$	611.6
		$k_\infty = 0.0074, \epsilon_\infty = 0.032$	6×10^{-3}
5	983941	SST $-k-\omega$	23.0
		$k_\infty = 0.0074, \omega_\infty = 0.389$	8.3×10^{-3}
6	3300198	SST $-k-\omega$	265.9
		$k_\infty = 0.0074, \omega_\infty = 0.389$	1.4×10^{-2}
7	3300198	SST $-k-\omega$	284.5
		$k_\infty = 0.0096, \omega_\infty = 0.05175$	7×10^{-3}
8	5208203	SST $-k-\omega$	563.7
		$k_\infty = 0.0074, \omega_\infty = 0.389$	6×10^{-3}

Table 2.1: Number of mesh cells and upstream values of the turbulence model parameters in each one of the 8 different computational cases considered in Fig. X for the flow around a single flat plate (k in m^2/s^2, ϵ in m^2/s^3 and ω in s^{-1}). Also included in the last column is the computational time in hours to advance 10^{-1} units of non-dimensional time for $\alpha = 10^\text{o}$ (see Fig. 4(d)), using just one CPU and the mean time step Δt (see main text).

ison with the experimental results, we report here only 8 different cases, as summarized in Table 2.1: 3 different grids with increasing number of cells, combined with two different sets of parameters for each turbulence model in the case of the "medium" mesh (that depicted in Fig. 2.2), and only one of the sets of parameters for each turbulence model in the cases of the "coarse" and the "fine" meshes (although all the other upstream turbulence model parameters were also checked with these meshes). The coarse and the fine meshes had a similar distribution of cells in each model but with smaller and larger number of cells, respectively (see Table 2.1). On the other hand, the values of the upstream turbulence model parameters for each set given in Table 2.1 correspond to those recommended for each model in the OPENFOAM toolbox 8 for similar 3D aerodynamic flows and Reynolds numbers (cases 3 and 7), and those computed by us using the turbulence intensity and its streamwise variation rate measured in a wind tunnel facility in our laboratory, for the given Reynolds number (remaining cases). Many more values of k_∞ ; ϵ_∞ and ω_∞ were tested, but we report here only a selection of them, including the cases that best fitted the experimental data for each model. Table 2.1 contains also information about the computational time and the time step. At each instant the time step was adjusted to a Courant number of 0.2, and Table 2.1 shows the approximately constant values reached after the initial transient.

Some results for $\alpha = 10^{\circ}$ are shown in Fig. 2.3 and 4. In particular, Fig. 2.3 shows the eddy viscosity contours when computed with both turbulence models (cases 2 and 6 in Table 2.1). Note that their values and distributions are quite different, explaining the significant differences in the lift and drag coefficients computed with each model observed below. Figure 4 shows some relevant results when the parameters of case 6 are used: a de-

tail of the final steady state of the non-dimensional streamwise velocity and pressure fields in the vicinity of the flat plate, the final values of the pressure and friction coefficients on the upper and lower surfaces of the plate, and the temporal evolutions of the lift and drag coefficients. The pressure and friction coefficients, C_p and C_f, are both made dimensionless with $\frac{1}{2}\rho W^2$, and it is observed that C_f is much smaller than C_p. Note also in Fig. 4(d) the oscillations at the initial stages of the numerical simulations, which are due to the fact that the computations started with the flow at rest. However, a steady state was already reached at non-dimensional time $tW/c \simeq 0.40$ (the results plotted in Figs. 4(a)–4(c) are for $tW/c = 0.5$).
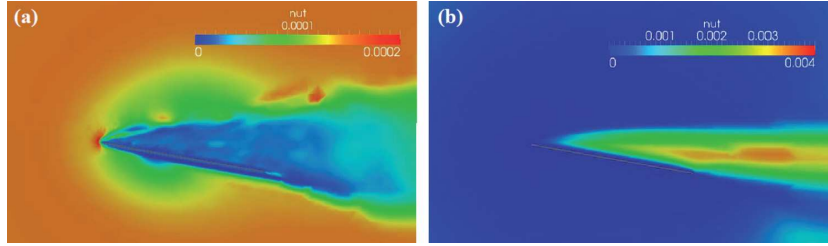
Figure 2.3: Contours of the computed eddy viscosity ν_t on a portion of the middle plane $z = 1.5c$ for the 3D flow around a flat plate with sAR =3, $Re_W = 8 \times 10^4$ and $\alpha = 10^o$ when the RNG $-k - \epsilon$ and the SST $-k - \omega$ turbulence models are used. In particular, (a) corresponds to case 2 in Table I and (b) to case 6.

Figure 5 contains the comparison of the experimental results of Pelletier & Mueller (2000) for the lift and drag coefficients as functions of the angle of attack α with the values of C_L and C_D computed numerically with each one of the 8 cases given in Table 2.1. It is clear from this figure that the SST $-k-\omega$ model works much better for this problem than the RNG $-k-\epsilon$ model, especially when the second set of upstream turbulent parameters mentioned

above is used. In addition, it is observed that the results obtained with the medium mesh practically coincide with those obtained with the fine mesh. Therefore, we selected the medium mesh, since the computational time and memory are both much smaller than for the fine mesh, together with the SST $-k-\omega$ turbulent model with k_∞ and ω_∞ given by the second set of parameters. That is, we selected the parameters of case 6 in Table 2.1 for most of the computations reported below.

However, for higher values of the angle of attack than those depicted in Fig. 5 (i.e., $\alpha \gtrsim 20$, for which no previous experimental data exist to compare with), we used the fine mesh in the computations (case 8 in Table 2.1). In fact, to check the accuracy of the numerical results we also calculated the relative errors of each mesh using Richardson extrapolation, Richardson (1911) in addition to the above comparison with previous experimental results. Particularly, we computed the fourth-order estimate of C_L for each α with Richardson extrapolation using the medium and fine meshes (grid refinement ratio $r \simeq 1.6$; see, e.g., Roache (1998) for the details), and with this value estimated the relative errors in C_L when computed with the medium and the fine meshes, respectively, for each α. Table 2.2 contains the results. One can observe that for $\alpha = 25^o$ and 30° the relative errors estimated for the mean final values of C_L are not sufficiently small when obtained with the medium mesh, while they remain acceptable when using the fine mesh. This is a consequence of the oscillatory behavior of the wake behind the flat plate, due to vortex shedding after flow separation, when the angle of attack $\alpha \gtrsim 20$ (Sec. IV). Therefore, we used the fine mesh in the computations of the flow around a single plate when $\alpha > 20^o$, and the medium mesh for $\alpha \leq 20^o$.
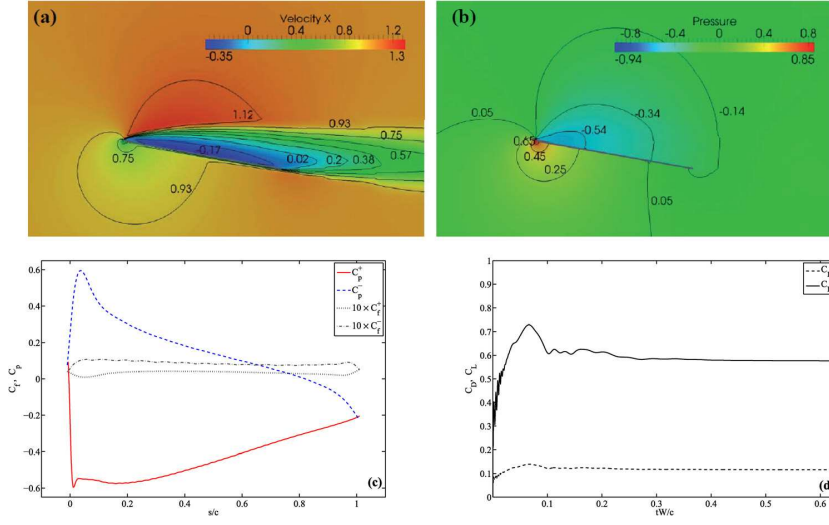
Figure 2.4: Plan view of the computed non-dimensional streamwise velocity component (a) and pressure (b) contours on a portion of the middle plane $z = 1.5c$ for the 3D flow around a flat plate with sAR=3, $Re_W = 8 \times 10^4$ and $\alpha = 10^o$ when the parameters of case 6 in Table 2.1 are used. The results are for the final steady state; the velocity is non-dimensionalized with the incident speed W and the pressure with $\frac{1}{2}\rho W^2$. (c) Distribution of the pressure and friction coefficients, C_p and C_f , on the upper ($^+$) and lower ($^-$) surfaces of the plate for the same time (s is the coordinate along the plate; note that (b) is the distribution of C_p on $z = 1.5c$). (d) Computed temporal evolutions of C_L and C_D.
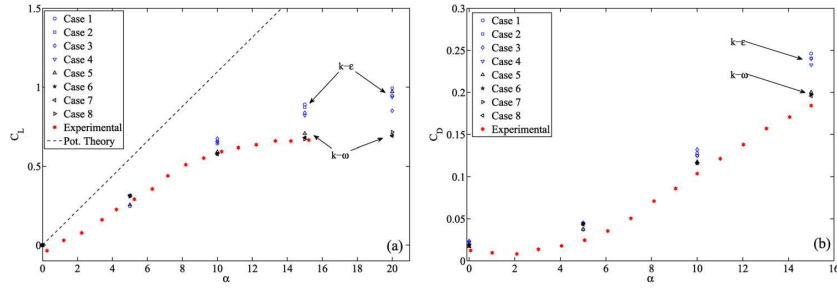
Figure 2.5: Comparison between the experimental results of Pelletier & Mueller (2000) for C_L (a) and C_D (b) vs. the angle of attack α for a flat plate with sAR=3 and $Re_W = 8 \times 10^4$ and the numerical results obtained which each one of the 8 cases given in Table 2.1. For reference sake, the potential 2D flow result $C_L = 2\pi \sin \alpha$ is also included in (a)

For a cascade of flat plates, the mesh used in the numerical computations reported below is similar to, and has the same resolution of, the medium one depicted in Fig. 2.2 for a single plate, but containing several flat plates in a computational domain such that one may set periodic boundary conditions (see Fig. 6). In particular, all the boundary conditions are the same as those described above for the case of a single flat plate, except for the cyclic boundary conditions for all the fluid variables (including the turbulent functions k, ϵ and ω) which are set between the "inclined" surfaces partially seen in the plan view depicted in Fig. 6. We have selected this configuration and domain size, with at least three plates (width $3s$ perpendicular to the cyclic plane, where s is the separation between plates), to simplify the numerical implementation, since it was easier to adjust the number of plates to a fixed periodic domain (sometimes we had to add fractions of a plate) than to change the shape and the size of the computational domain whenever the separation between plates or the angle of attack was varied.

To select the appropriate mesh for each angle of attack, we also esti-

$\alpha(\circ)$	Error in $C_L(\%)$ 1 plate Medium mesh	Error in $C_L(\%)$ 1 plate Fine mesh
5	1.45	0.36
10	1.00	0.25
15	1.94	0.48
20	4.16	1.04
25	38.81	9.70
30	37.11	9.28

Table 2.2: Estimations of the relative errors in the final mean value of C_L for a single plate computed with the medium and fine meshes, in relation to the extrapolated Richardson estimate, for different values of α.

mated the relative numerical errors in C_L using Richardson extrapolation with medium and fine meshes (see Table III). Now, the computational errors with the medium mesh were acceptable (much below 10% in most cases) even for high values of the angle of attack, as a consequence of the fact that the flow remains attached to the plates in the cascade (see Sec. IV). Therefore, since the necessary computational time and memory are both much larger with the fine mesh than with the medium mesh, we used the medium one in all the computations reported below for a cascade of flat plates.
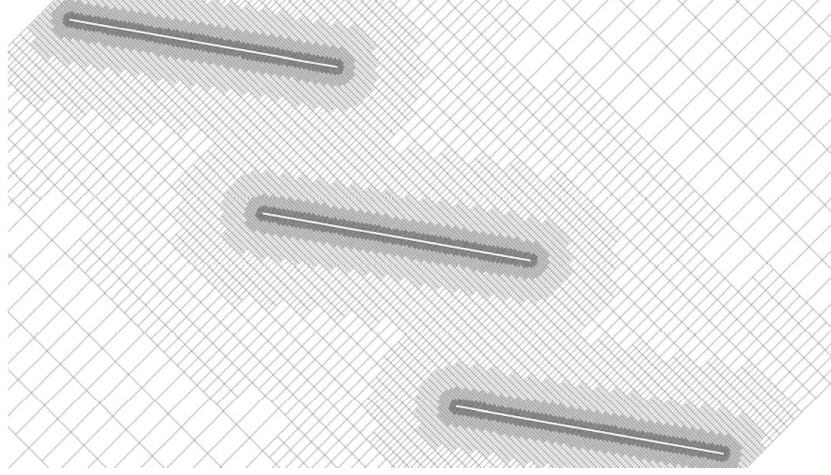
Figure 2.6: Plan view (constant z) of a detail of the (medium) computational mesh used in the numerical simulations for the cascade of flat plates with $\xi = U/V = 1(\theta = 45°)$, $\sigma = c/s = 1$ and $\alpha = 10°$. It is similar to that depicted in Fig. 2.2, but with a periodic array of three flat plates. The computational domain is (x along the cyclic plane and y perpendicular to it):$-3c \leq x \leq 3c, 0 \leq y \leq 3s, 0 \leq z \leq 4.5c$. The total number of cells is 6123575.

2.4 Results and discussion

We have performed a series of numerical simulations using the numerical code discussed above with the objective of finding out the optimum configuration of the cascade of flat plates that extracts the maximum power from a given tidal current. In particular, we fixed $Re = 5.66 \cdot 10^4$ (which corresponds to $Re_W = 8 \cdot 10^4$ for $\xi = 1$) and sAR=3, as the reference values (like in Sec. III XXX), and looked for the optimum value of α (or γ) which yields the maximum C_P when ξ and σ are varied. These results are compared with the corresponding ones for an isolated flat plate.

The main aerodynamic effect of a cascade in relation to a single blade is that the lift coefficient of each element in the cascade could be substantially increased in relation to the same isolated element if the stagger angle and the separation between blades are conveniently selected, as already predicted from the two-dimensional potential theory of a cascade of flat plates (see,e.g., Weinig (1964) in particular, for $\gamma \rightarrow 90^o$ and $\sigma \approx 1$, the 2D potential lift tends to infinity). When viscous and 3D effects are taken into account, this potential increase in the lift coeffi- cient cannot be so pronounced as predicted by the 2D potential theory, but still it may be very significant, mainly due to the "streaming" effect of the cascade, that delays the stall as the angle of attack is increased. Thus, higher lift coefficients can be attained for a plate in a cascade than for an isolated plate when the angle of attack is sufficiently high and the lift of the single plate has already dropped. However, as we shall see, the drag coefficient for the plate in the cascade may be larger than for an isolated plate, and the lift coefficient may be smaller, depending on the particular configuration, so that the global effect of lift and drag coefficients on C_P has to be analyzed for all the different configurations, or different values of γ, ξ and σ.

$\alpha(°)$	Error in $C_L(\%)$ cascade Medium mesh	Error in $C_L(\%)$ cascade Fine mesh
5	2.19	0.55
10	0.59	0.15
15	5.85	1.46
20	0.33	0.08
25	0.27	0.07
30	2.32	0.58

Table 2.3: Estimations of the relative errors in the final mean value of C_L for a plate in a cascade computed with the medium and fine meshes, in relation to the extrapolated Richardson estimate, for different values of α. ($\xi = 1, \sigma = 1, \text{sAR} = 3, Re_W = 8 \cdot 10^4$)
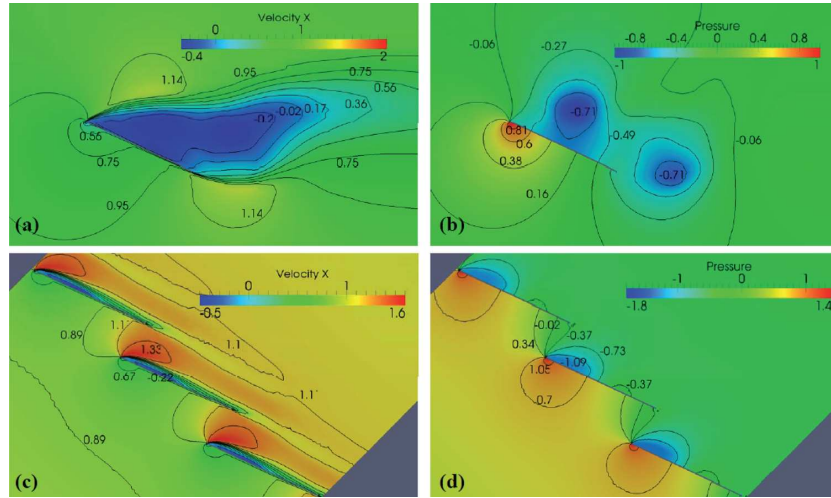
Figure 2.7: Plan view of the computed non-dimensional streamwise velocity component and pressure fields (the velocity is scaled with W and the pressure with $\frac{1}{2}\rho W^2$) on a portion of the middle plane $z = 1.5c$ for the 3D flow around a single flat plate (a) and (b), and a cascade with $\sigma = 1$ and $\xi = 1$ (c) and (d), for $\alpha = 25°$ (sAR=3, $Re_W = 8 \cdot 10^4$).

To illustrate this, Fig. 2.7 and Fig. 2.8 show a comparison between the velocity and pressure fields around a single plate and through a cascade of flat plates with $\xi = \sigma = 1$ and $\alpha = 25^{\text{o}}$. For this angle of attack, the single flat plate is already stalled, and the wake behind it becomes oscillatory due to the vortex shedding, as it is clear in the time evolution of C_D and C_L of Fig. 2.8(c) (the images in Fig. 2.7(a) and (b) correspond to an instant of time after the permanent oscillatory regime has been reached, and one can clearly identify two vortices in the pressure field picture of Fig. 2.7(b), which are evolving in time). On the contrary, the flow in the cascade for this high angle of attack is still attached to the plates, with just a narrow region of flow recirculation on the upper surfaces of the plates close to the leading edge. This divergence between the flow regimes in the two configurations starts at a value of α between 15° and 20°, above which the flow over a single plate becomes separated and the mean value of C_L ceases to increase like in the case of a cascade (see Fig. 2.9). The oscillatory wake is clearly observed for angles of attack α above 25°, approximately, as indicated in Fig. 2.9 by the error bars attached to the mean values of C_L and C_D for a single plate, which measure the amplitude of the computed oscillations around their mean values. The amplitude of the oscillations in C_L and C_D for an isolated plate is even larger for $\alpha = 30^{\text{o}}$ than for $\alpha = 25^{\text{o}}$ (see Fig. 2.10(a)). In contrast, for the cascade, a stationary steady state is always reached for all the values of a considered here (up to $\alpha = 30^{\text{o}}$), and C_L keep increasing with α (see Fig. 2.9(a)). As a consequence, the maximum value of the power coefficient (6) for the cascade (which in the present configuration with $\xi = 1$ is given by $C_P = \sqrt{2}(C_L - C_D)$) is reached at a relatively high value of α, and C_P becomes larger than for an isolated plate (see Fig. 2.11). It is worth commenting here that although the maximum in the mean value of C_P for an isolated plate is

reached in this case for an angle α in the same range than for a cascade, the large oscillations in C_L and C_D, due to the oscillatory wake behind the plate for these high values of α, make useless this maximum of C_P for an isolated plate from a practical point of view. Thus, the other relative maximum of C_P for a single plate, reached for a smaller value of α (see Fig. 2.11), is the most interesting one from practical point of view. In either case, this maximum of C_P is, in the present configuration, smaller than that for a plate in a cascade.

Figure 2.8: Distribution of the pressure and friction coefficients, C_p and C_f , on the upper ($^+$) and lower ($^-$) surfaces for an isolated plate (a), and for a plate in the cascade (b), for the same cases of Fig. 2.7 (c) and (d): Computed temporal evolutions of C_L and C_D for the same cases of Fig. 2.7
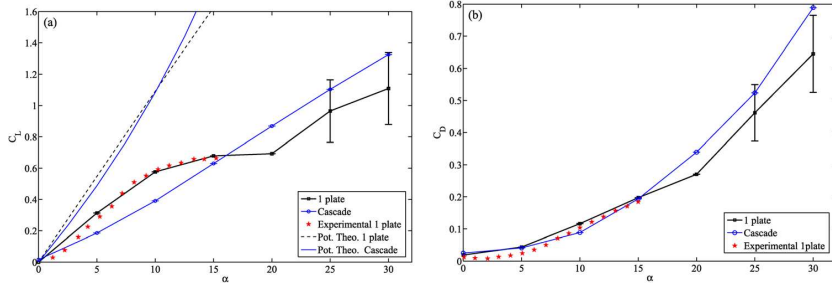
Figure 2.9: Comparison between C_L (a) and C_D (b) vs. α for an isolated plate and for a cascade with $\sigma = 1$ and $\xi = 1$ (sAR=3, $Re_W = 8\dot{1}0^4$). The error bars indicate the amplitude of the temporal oscillations around their mean values due to the oscillatory wake behind an isolated flat plate. The experimental results for a single plate by Pelletier & Mueller (2000) are included. Also included in (a) for reference sake is the 2D potential flow result $C_L = 2\pi \sin \alpha$ sin a for a single plate and the corresponding potential result for a cascade of flat plates Weinig (1964)
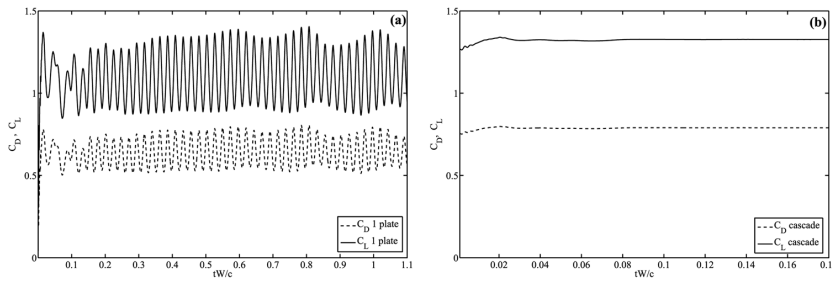
Figure 2.10: Computed temporal evolutions of C_L and C_D for the same cases of Fig. 2.7, but for $\alpha = 30^o$
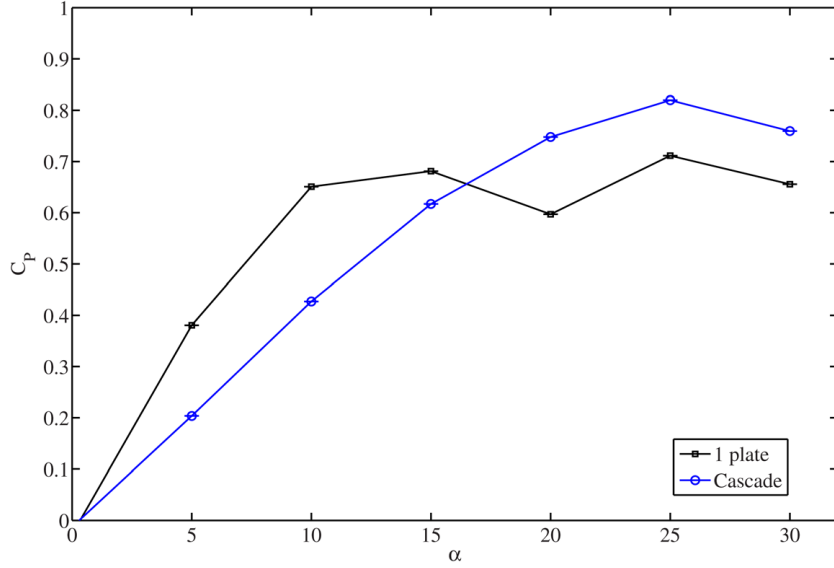
Figure 2.11: Comparison between C_p vs. α for an isolated plate and for a cascade with $\sigma = 1$ and $\xi = 1$ (sAR)=3, $Re_W = 8\dot{1}0^4$). Only the mean values are plotted for the isolated plate

This qualitative behavior as the angle of attack is varied is not the general rule for all the values of σ and ξ considered in this work. For instance, for the same $\sigma = 1$ but for larger $\xi = U/V$ (e.g., $\xi = 2.5$, see Fig. ??), the maximum value of C_P is higher for an isolated plate than for a plate in the cascade, and in both cases this maximum is reached for a similar, relatively low, value of the angle of attack α. This is due to the fact that the role of the drag C_D in C_P becomes more important as ξ increases (see (6), and note also in Fig. 2.1 that the angle θ increases with ξ), so that the maximum of C_P is reached in both cases at low values of α for which C_L for an isolated plate is larger, and so is C_P (see Fig. 2.12). On the other hand, for $\xi = 1$ and $\sigma \simeq 1.43$ (Fig. 2.13), which corresponds to a smaller separation s between the plates in the cascade, the situation is qualitatively similar to that depicted in Fig. 2.11, but now the maximum value of C_P for a single plate is slightly larger than for

a plate in the cascade because C_L remains lower in this last case even in the range of values of α where $C_{P,max}$ is reached for the cascade. The reason for this different behavior has to be found in the flow through the cascade, which is shown in Fig. 2.14 for $\alpha = 25^o$, corresponding roughly to the maximum of C_P. Comparing Fig. 2.14(a) and (b) with Fig. 2.7 (c) and (d), the main difference is that the recirculation region above the plates is larger when the separation between plates is smaller ($\sigma = 1.43$ in Fig. 2.14(a)) due to the larger speed between the plates in the cascade. As a consequence, the lift coefficient is smaller than for $\sigma = 1$ (compare Fig. 2.8(d) with Fig. 2.14(d)), and so it is $C_{P,max}$.
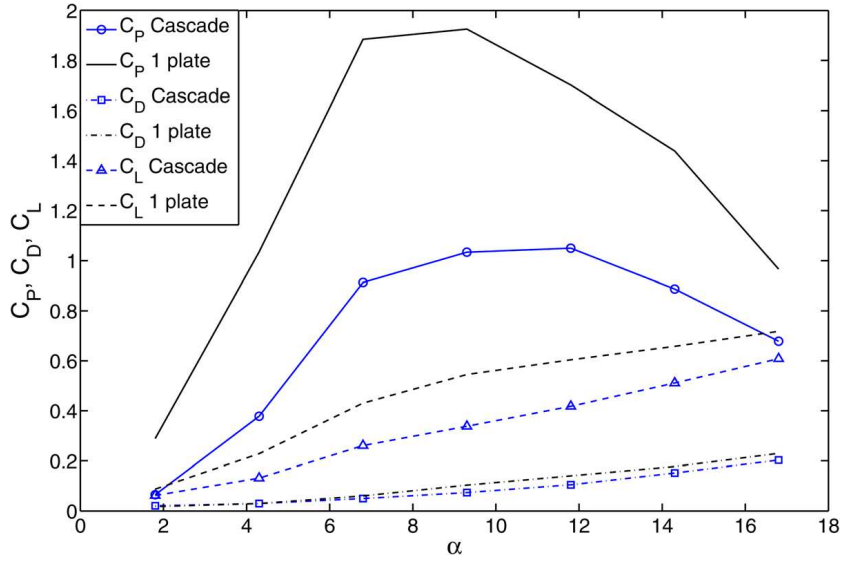
Figure 2.12: Comparison between C_P, C_L, and C_D vs. α for an isolated plate and for a cascade with $\sigma = 1$ and $\xi = 2.5$

Fig. 2.15 summarizes $C_{P,max}$ for all the values of ξ and σ considered in this work. In particular, curves of $C_{P,max}$ as functions of ξ are plotted for different values of the solidity σ (in fact, the non-dimensional plate separation σ^{-1}). Also included is the curve of $C_{P,max}$ for an isolated plate as a function of

ξ. Obviously, this last curve approaches that of a plate in the cascade when the separation is very large ($\sigma^{-1} \longrightarrow \infty$ note that the curve for $\sigma^{-1} = 10$ is already quite close to that of a single plate). It is observed that $C_{P,max}$ for a plate in the cascade is larger than for an isolated plate only in a small range of values of σ close to unity, provided that ξ is also near unity.
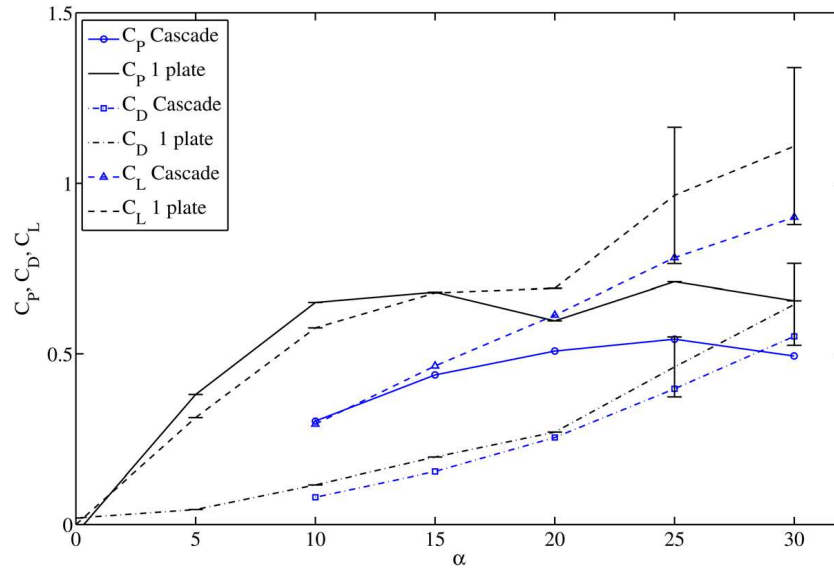
Figure 2.13: Comparison between C_P, C_L, and C_D vs. α for an isolated plate and for a cascade with $\sigma = 1$ and $\xi = 2.5$
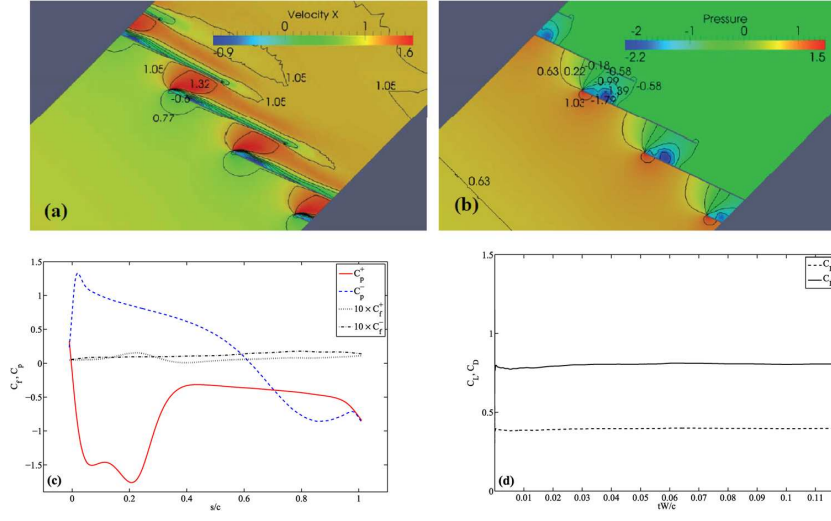
Figure 2.14: Plan view of the computed non-dimensional streamwise velocity component (a) and pressure (b) contours on a portion of the middle plane $z = 1.5c$ for the final steady state of the 3D flow through a cascade with $\xi = 1$; $\sigma \simeq 1.43$ and $\alpha = 25$ (sAR=3, $Re_W = 8 \cdot 10^4$). The velocity is 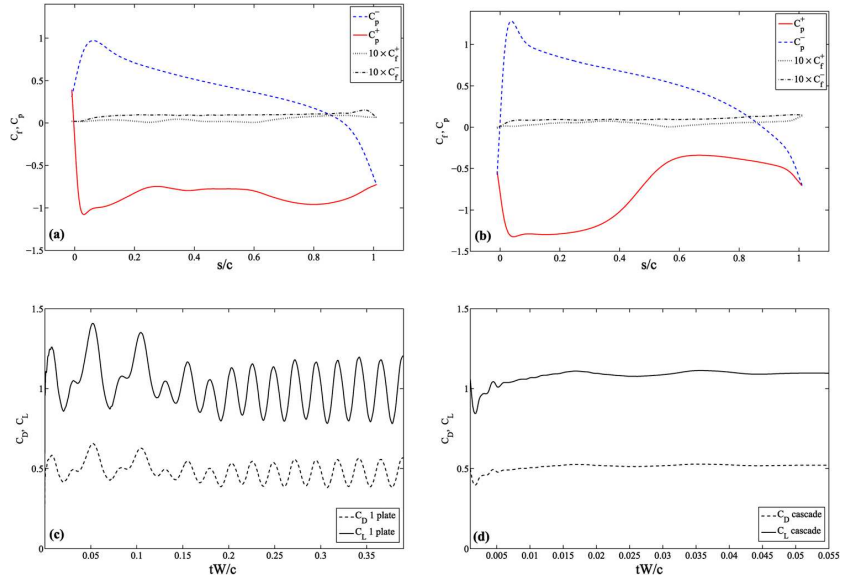non-dimensionalized with W and the pressure with $\frac{1}{2}\rho W^2$. (c) Distribution of the pressure and friction coefficients, C_p and C_f , on the upper ($^+$) and lower ($^-$) surfaces of a plate in the cascade for the same time (s is the coordinate along the plate, $z = 1.5c$). (d) Computed temporal evolutions of C_L and C_D for a plate in the cascade.
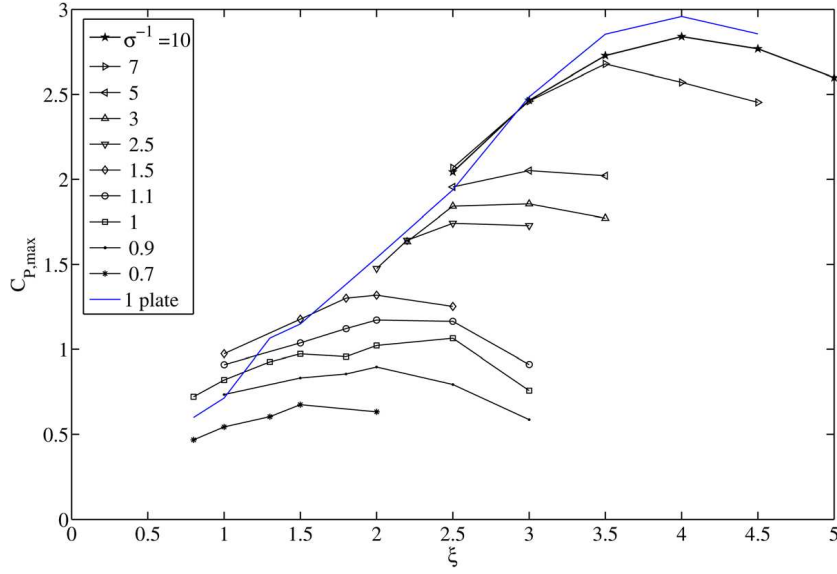
Figure 2.15: $C_{P,max}$ as a function of ξ for different values of σ^{-1}. Also included is the curve for a single plate as a function of ξ. (sAR=3, $Re_W = 8 \cdot 10^4$)

Fig. 2.16 depicts the angles of attack a corresponding to the $C_{P,max}$ in Fig. 2.15. For large ξ the values of α_{max} for a plate in the cascade are relatively small and quite similar to the values for an isolated plate, as explained above. As ξ decreases, α_{max} increases for both the cascade and the isolated plate. Note the "zigzag" behavior of the curve for the isolated plate in the low ξ region, which is due to the fact that α_{max} is within the stalled region for a single plate. The cascade results in Fig. 2.16 are almost independent of σ and can be approximated by the relation $\alpha_{max} \simeq 24.874\xi^{-0.876}$.
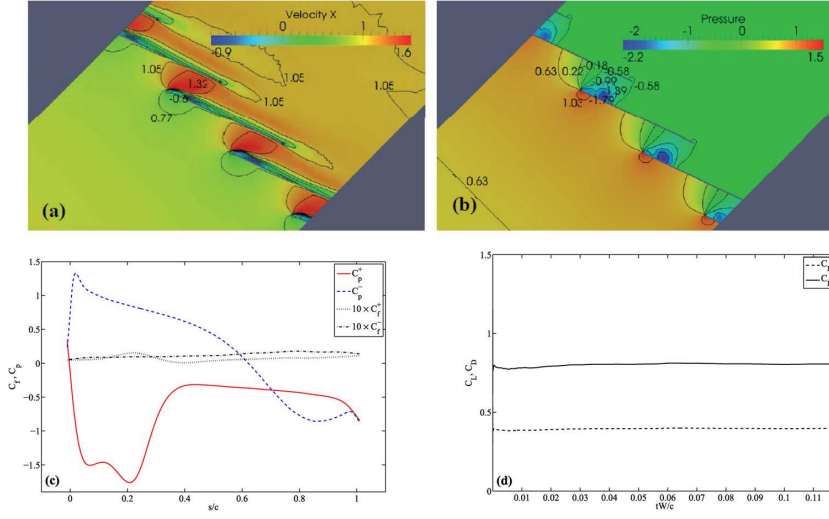
Figure 2.16: Values of the angle of attack $\alpha(^\circ)$ corresponding to the $C_{P,max}$ in Fig. 2.15

The results in Fig. 2.15 show that $C_{P,max}$ increases as r decreases (the separation between plates increases) and ξ increases, approaching the values for an isolated plate as $\sigma^{-1} \longrightarrow \infty$. However, $C_{P,max}$ is not very appropriate for selecting the optimum values of σ and ξ because one has to take into account that the total power carried by the cascade obviously increases with the number of plates per unit length; i.e., it increases linearly with the solidity, or blade packing density, σ. For this reason, it is convenient to define a new power coefficient,

$$\overline{C}_P \equiv \sigma C_P = (C_L - \xi C_D)\xi\sqrt{1+\xi^2}\sigma, \qquad (2.10)$$

which is proportional to the nondimensional power extracted per unit length of the cascade of plates. The maximum values of this quantity with respect to α as ξ is varied, for selected values of σ, are plotted in Fig. 2.17. It is clear from this figure that the optimum value of σ (yielding the highest values of $C_{P,max}$) is close to unity. This can be explained as a compromise

between small values of σ, for which $C_{P,max}$ is larger but the blade packing density is smaller, and high values of σ, for which the proximity between blades diminishes the lift coefficient of each blade, as we have seen above. Within $\sigma \approx 1$, the optimum performance is reached for ξ between 2 and 2.5. However, these values of ξ are perhaps too large for practical interest, and one may select the other relative maximum observed in Fig. 2.17 for $\sigma = 1$ around $\xi = 1.5$. All this is better appreciated in Fig. 2.18, where the maximum values of $\overline{C}_P$ are potted in a contour map in the plane (σ^{-1}, ξ) by interpolating the curves shown in Fig. 2.17. The top value of $\overline{C}_P$ is reached for σ between 0.9 and unity when ξ is between 2 and 2.5. However, there is another relative maximum, also with σ close to unity, when $\xi \approx 1.5$, which is probably preferred because $\xi \gtrsim 2$ might not be attained from a practical point of view. These two maxima of $\overline{C}_P$ for $\sigma \approx 1$ are related to the shift discussed above from small optimum angle of attack α_{max} , when ξ is large and the drag coefficient is more relevant for $\overline{C}_P$, to higher values of α_{max} when ξ diminishes (see Fig. 2.12 and Fig. 2.11, respectively). In any case, this figure tells us that the best operating conditions are in a broad region with σ between 0.8 and unity and ξ between 1.5 and 2.5, approximately.

To find out the optimum values of the stagger angle $\gamma = \alpha + \theta$ of the plates corresponding to these top values of $\overline{C}_P$, Fig. 2.19 shows the contour map of γ_{max} in the plane (σ^{-1}, ξ) corresponding to the maximum of $\overline{C}_P$ depicted in Fig. 2.18. Remember that $\theta = \arctan(\xi)$, so that γ_{max} basically increases with ξ, except for the additional variation of α_{max} with ξ and σ (Fig. 2.16). For $\sigma \approx 1$ and $\xi \approx 2.5$ the optimum value is $\gamma_{max} \approx 79^o$, while for $\xi \approx 1.5$; $\gamma_{max} \approx 75^o$. Note that the decrease in α_{max} as ξ increases commented on above is more than compensated by the increase of θ with ξ, resulting in a similar value of γ_{max} for both optimum values of ξ.
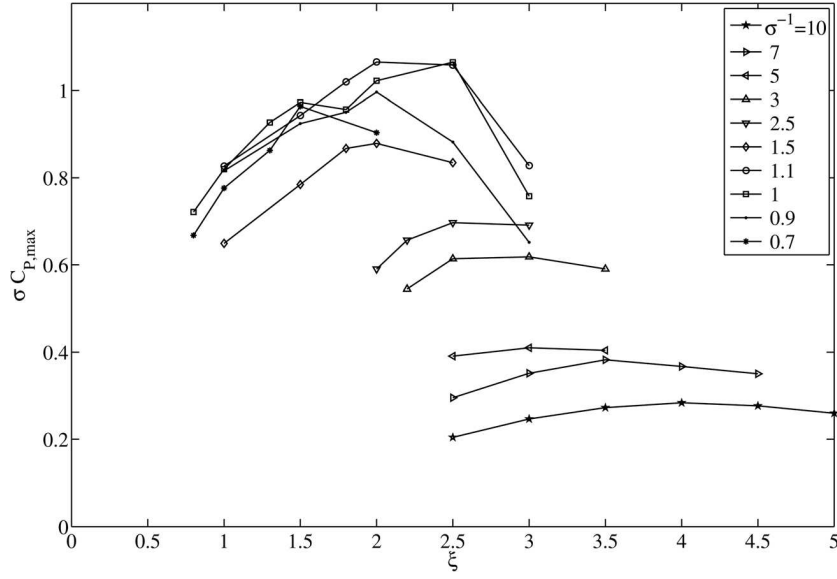
Figure 2.17: $\overline{C}_{P,max} \equiv \sigma C_{P,max}$ as a function of ξ for different σ.
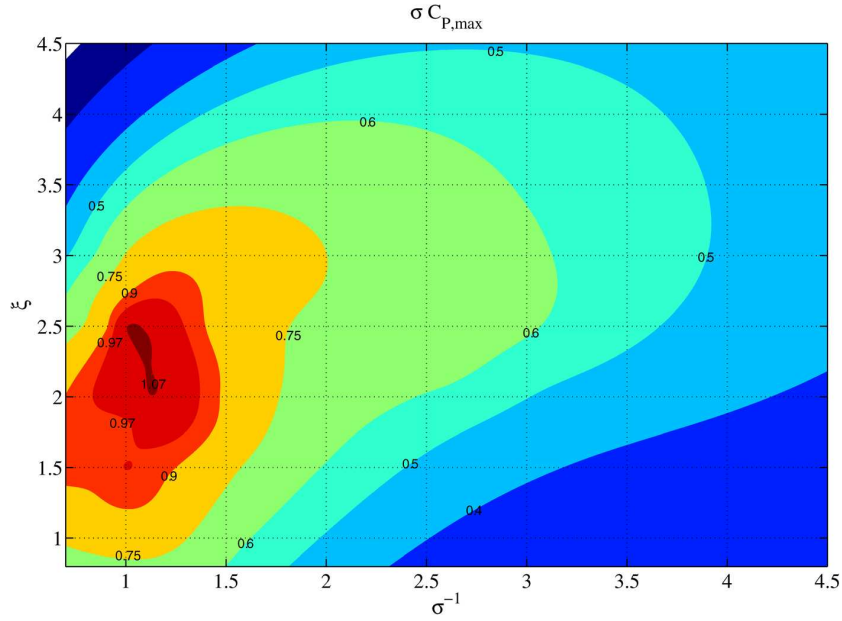
Figure 2.18: Contour plot of $\overline{C}_{P,max}$ in the (σ^{-1}, ξ)-plane.

It is interesting to plot the distribution of turbulence kinetic energy for the case of maximum power, and compare it with some other configurations,

since it yields useful information about the intensity of the vortices and it has been shown in wind turbines that its vertical flux is of the same order of magnitude as the power extracted by the wind turbines Cal *et al.* (2010). It is seen in Fig. 2.20 that the turbulent kinetic energy is highly concentrated above the leading edge of the blades, Subhra Mukherji *et al.* (2011) and it is slightly larger in the case where a relative maximum of the power coefficient is reached (for $\xi = 1.5$ and $\sigma = 1$) than in the other two cases for which the power coefficient is smaller ($\xi = 1$ and two different values of σ; note that Fig. 2.20(b) and (c) correspond to the same cases plotted in Fig. 2.14 and Fig. 2.7, respectively).
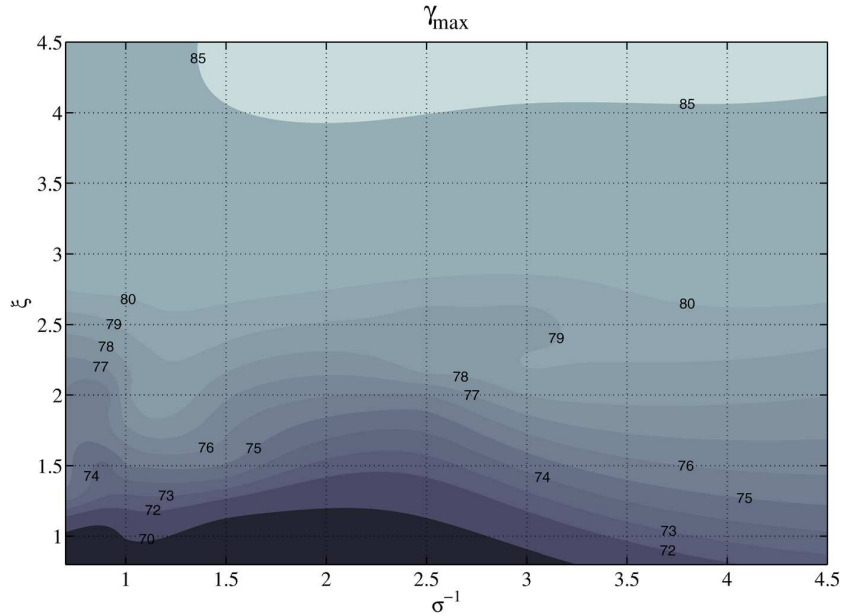
Figure 2.19: Contour plot of $\gamma_{max}(^{\circ})$ in the (σ^{-1}, ξ)-plane corresponding to $C_{P,max}$ in Fig. 2.18
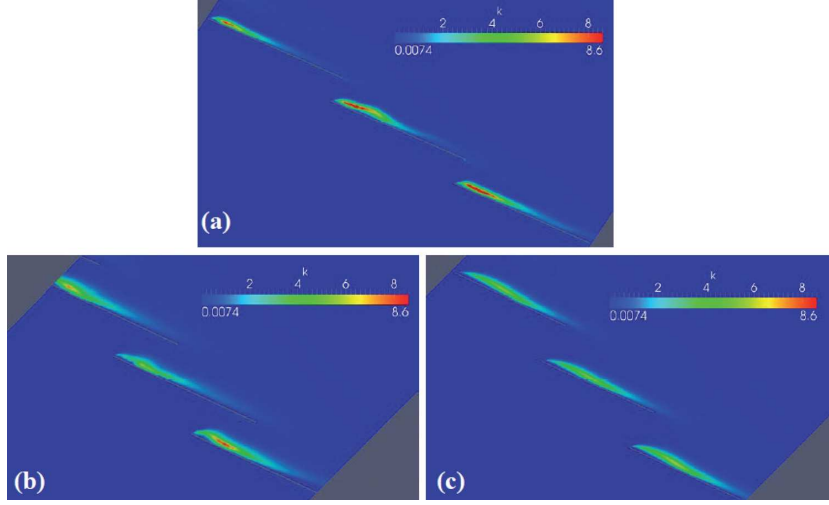
Figure 2.20: Plan view of the computed turbulence kinetic energy k (m^2/s^2) on a portion of the middle plane $z = 1.5c$ for the final steady state of the 3D flow through a cascade with $\sigma = 1$; $\xi = 1.5$ and $\alpha = 35$º (a), $\sigma = 1.43$, $\xi = 1$ and $\alpha = 25$º (b), and $\sigma = 1$, $\xi = 1$ and $\alpha = 25$º (c). (sAR=3, $Re_W = 8 \cdot 10^4$, $k_\infty = 0.0074$m^2/s^2)

2.5   Summary and conclusions

In this study, we have performed a series of detailed CFD simulations with the objective of finding out the optimum hydrodynamic configuration of a particular device for extracting energy from tidal or river currents, TidalSail S.A. (2014) using a simplified model of the device consisting of a cascade of flat plates moving perpendicularly to the current. The nondimensional parameters which have been varied in the present study are the angle of the blades (stagger angle γ in relation to the tidal current), the separation between blades (solidity $\sigma = c/s$) and the blades speed ($\xi = U/V$), while the Reynolds number Re of the tidal current and the (semi)-aspect ratio (sAR) of the blades have been kept constant. We have chosen values of

Re and sAR which are in the range of interest for the tidal energy device under consideration, and for which there exists reliable experimental data for a single plate to validate the numerical simulations. Thus we selected the turbulence model and the values of their upstream turbulent parameters that best fitted these experimental results, in addition to the optimum number of mesh cells for the computations in each case.

For the particular configuration selected that moves perpendicularly to the tidal current, and for flat plates with the given aspect ratio and selected Reynolds number, we find that optimal results (maximum power coefficient per unit length of the cascade $\overline{C}_P$) are obtained when the solidity $\sigma \approx 1$, the stagger angle $\gamma \approx 79^{\circ}$ and the blades speed, related to the the tidal current, $\xi \approx 2.5$. A second best configuration, with a relative maximum value of $\overline{C}_P$ slightly smaller, is $\sigma \approx 1$, $\gamma \approx 75^{\circ}$ and $\xi \approx 1.5$. This last configuration is preferred because its smaller value of n would be more easily obtained from a practical point of view. In either case, the optimum solidity is about unity and the best stagger angle around 75°. Although the hydrodynamic performance of the device will obviously improve if airfoils with more sophisticated profiles than a simple flat plate were used in the cascade, we believe that the present aerodynamic study fulfills the basic objective of finding out a first approximation for the optimal cascade configurations in terms of γ, σ, and ξ. Further studies, both experimental and computational, using blades with different profiles and aspect ratios, and moving in a cascade at different angles in relation to the tidal current, with different Reynolds numbers, are needed to refine the optimal configurations here obtained, which may be used as starting points.

Chapter 3

Methodology and validation of a 3D surface reconstruction technique by image processing

3.1 Introduction

The interest of digitizing 3D underwater surfaces is with the aim of obtaining a quantification of the scour commonly generated by the moving sails of devices used to extract tidal energy explained in the Sec. 1.2. Once the dimension of the device are known, it is possible to act accordingly to thereby minimize the environmental impact. To that end, we will try to quantify the erosion on a sandy bottom due to the presence of the sail in a tidal current depending on the proximity between the sail and the bottom, and on the angle of attack between the current and the sail.

The main problem one has to overcome dealing with 3D underwater surface reconstruction is the poor visibility due to light scattering in the media (Schechner & Karpel, 2004). There are many techniques to reconstruct the

non-uniform surface of a sandy bottom by means of image manipulation (see Kocak & Caimi, 2005, for a review).

In general, there are multiple methodologies in the literature for digitizing bodies (Pavlidis *et al.*, 2007; Rocchini *et al.*, 2001). Perhaps, one of the best known methods is the surface reconstruction by taking pictures from different shot angles, and use the commonly known as the Structure-From-Motion (SFM) and Dense Multi-View 3D Reconstruction (DMVR) algorithms to get the real magnitude of the surface (Liu & Zhang, 2014; Koutsoudis *et al.*, 2014; Westoby *et al.*, 2012). To use this type of methodology, one has just to work with an open source software that allows easily to scan surfaces (see VisualFSM, 2014). Although it would be ideal to use this method in this work, these techniques carry out the 3D reconstruction of the surface by manipulating multiple images at different angles and without considering the refraction of light due to water-air media change. For that reason, in this work we develop a technique that allow to work with the water-air media change.

There are other reconstruction techniques by using the method of density of points. They can calculate the distance between points according to their intensity on image (Gühring, 2000; Munro & Dalziel, 2005; Lv *et al.*, 2013). This technique requires a light source under the sand bed that allows to have regions with different light intensities according their different depths. This method is, however, very complicated in our hydraulic channel due to its dimensions, so there is not enough space to place the light bulbs under the sand. In addition, the technique here developed is cheaper.

Some authors work exclusively with the underwater 3D surface reconstruction, but they do not take into account the change from one media (air) to other (water). To that end, all the devices they use to capture the images

are under the water (Bruno *et al.*, 2011). As it has been said previously, the size available in our laboratory to digitize the scour generated on the seabed of the channel is very tiny to introduce the large objects this technique requires. However, there are other non-intrusive methods that solve the change of air-water media, but they need very expensive licenses to be used with full features, such as the ones described by Munro *et al.* (2004).

Therefore, we have considered necessary to develop a new non-intrusive technique to extract the 3D information of a sand bed deformation originated by any mechanism and without introducing large objects inside the channel or reservoir, allowing both the capture of images through the change of air-water media and the decrease in cost of the experimental methodology to reconstruct the 3D surface of a eroded, or non uniform, sandy bottom.

3.2   Taking pictures in the laboratory

The proposed method in this work consists, mainly, in a technique for underwater surface reconstruction by transforming a known point target and projecting lines on the surface to scan. First, the target is set in the closest projected line to the camera and a photo is taken, Fig. 3.1(a). A second photo of the target located in a different line is then taken see Fig. 3.1(b). It is important to remark that during the different steps of the methodology the camera can not be moved. Once the images of the targets have been taken with a certain angle between the camera and the horizontal, they are processed in a computer using the same point pattern but with all the points aligned horizontally and vertically, Fig. 3.1(d). Then, a group of matching points are pointed on two pictures. In the first one, the target appears distorted, as taking by the camera, and standing on the surface to scan, while

in the second picture the same pattern appears alone with the points aligned with the horizontal and vertical. As a result of the pattern point matching, a bilinear transformation is obtained, which will be later apply to the picture of the projected lines on the sand to get the real magnitude of the surface on which they are projected.

(a)

(b)

(c)

(d)
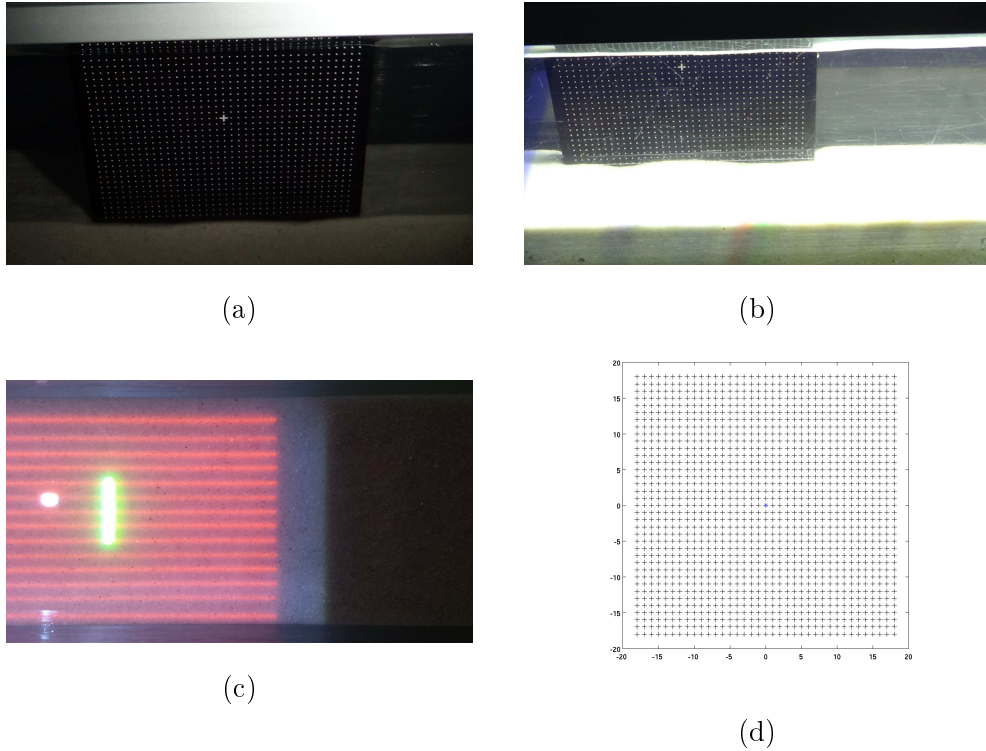
Figure 3.1: Images needed to start the surface reconstruction methodology: (a) Pattern of points in the first projected line; (b) Pattern of points in the last visible projected line; (c) Picture took from the plan view of the set of lines (XZ plane). The green line indicates the position of the plate; (d) Known Pattern with horizontal and vertical points

This technique needs, to work properly, some other devices, as it can be seen in Fig. 3.2. They are going to be described briefly in what follows:
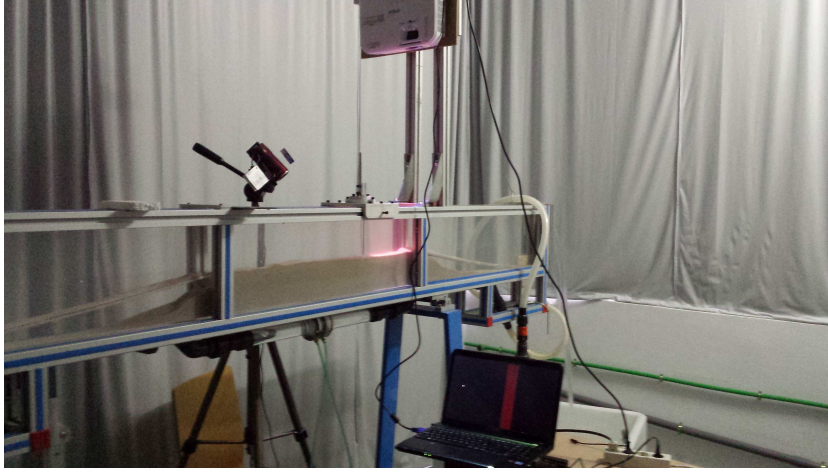
Figure 3.2: Overview of the whole 3D reconstruction system.

A video projector, that is used to draw lines on the surface to be reconstructed. These lines must cover all the surface to be scanned. A camera and a tripod, that are used to take images of both the targets and the deformed surface where the lines are projected. And a computer, that is used to send the lines to be projected to the video projector, and later used to carry out the image manipulation.

Although this technique can be applied to other contexts, and not just for surfaces submerged in water, in this work it will be used to analyze and study the scour generated by a flat plate located at a known distance from the bottom and with a given angle of attack with respect to the tidal current. To do this, we have a sediment hydraulic channel and a static object (in our case, the flat plate, or sail, used to extract the energy from the tidal current). Once the flat plate is located in the middle of the channel, it is considered as an obstacle for the current. The flow acceleration, due to the reduction in section, will be the reason for the scours and dunes to appear. These scours have a depth and size stable for a specific current (or Reynolds number), distance from the plate to bottom, and angle of attack of the flat plate.

To reconstruct the surface, it is important to indicate the coordinate axis used during the process. In particular, the ones used throughout this chapter are established in Fig. 3.3, where the x-axis indicate the streamwise direction, the y-axis corresponds to the perpendicular to the sand plane (gravity direction), and finally the z-axis is the spanwise coordinate, perpendicular to the flow direction.

Figure 3.3: Cartesian coordinates to be used during the reconstruction processes.

The steps of the proposed method are the following:

The first thing to do is to flatten the seabed in the hydraulic channel, so that it is as horizontal level as possible. On the sand, a series of lines, that serve to scan the surface, will be drawn thanks to the projector. The more lines one projects, the more accuracy is achieved when reconstructing the surface. The limit is on the number of lines the camera is able to capture without mixing pixels of different lines. It is important that all these lines are parallel and start at the same x coordinate. When the image processing finishes, all the graphs will be drawn from the beginning of the line and it will be given the coordinate, say, zero. The thickness of lines and their separation

will be proportional to the final error of the results. Thus, it has sense to use lines as thin as possible as long as they are captured by the camera and no information is lost.

The next step is to set the tripod oriented to the zone where the scour is expected to happen after the experimental test simulation. To start, the user has to take three photos, two of the targets and a plan view of the projected lines, see Fig. 3.1. These three pictures must be taken only once and they are enough to calibrate the system for digitizing pictures. The first picture is with the target on the first line, the closest one to the camera trying that all the points are placed as horizontal and vertical as possible, Fig. 3.1(a). The second one is the same image but with the target another line, the last one, if possible, Fig. 3.1(b). Thanks to these two images, we can measure any distance in the XY plane along the first and last line and, by linear extrapolation, it can be also calculated for any line between them. The third image is the one that has to be done in a different angle out of the tripod. Actually, it is a plan view of all the projected lines, as it can be seen in Fig. 3.1(c). With this image, any distance in the XZ-plane can be known, and thus the separation between the projected lines and the distance from the flat plate to their beginning, point chosen as x=0.

From now, we could say that there are two variations in methodology and in the way of obtaining the reconstruction of the scanned surface. The difference between both variations is whether it is taken an image of the flat bottom at the beginning of the experiment or not. In the first case, when an initial image is not taken, it is only necessary to take an image of the deformed bottom, Fig. 3.4(b) and, initially, the bottom must be as more uniform and horizontal as possible, thing that the user must ensure. In the other option, it is also necessary to take an image before the test

starts with the flat and uniform bottom, Fig. 3.4(a) and Fig. 3.4(b). This last methodology will allow us to see the real differences with respect to the initial state of the bottom, although it must be as more horizontal as possible, as it has previously been said, but in this case this fact is not so critical. Once the experimental simulation has finished, the erosion and thus, the shape of the bottom can be calculated taking just a new and last picture with the projected lines on it. The second option, and the most recommended, allows to the software to calculate the difference between the bottom lines before and after the erosion process took place. This last option also avoids errors in making a good flattening of the sandy bottom and inaccuracies in the horizontally of the patterns. In the end, all these pictures are processed in a computer for its analysis.

(a)   (b)
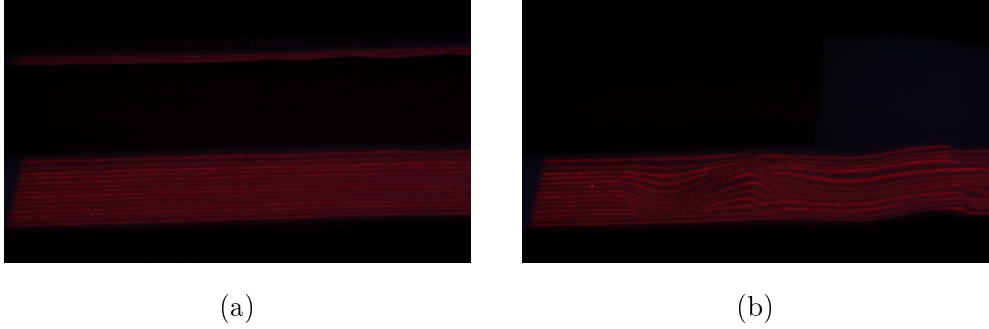
Figure 3.4: Images of the projected lines on the sand: (a) Before the erosion process; (b) After the erosion took place.

3.3 Analysis of the projected lines and surface reconstruction.

The software developed for reconstruction of the surface by means of the projected lines has been programmed in Matlab (Matlab, 2014). The code

only needs the three above mentioned initial images, the two target images and the plan view of the lines, as shown in Fig. 3.1, together with one, or two, or more, depending on the methodology finally used of the bottom illuminated with the projected lines, as shown in Fig. 3.4. When the user wants to know the relative differences of the eroded bottom with respect the initial state, the two pictures are needed.

At the beginning of the software, a initialization file is called to load the options needed for the code and initializes the objects (patterns and tests) with their own information. In this moment, the software loads the initial settings. Then, the first library "patternZ" is loaded. With it, the information of the plan view is loaded, that is the ZX-plane, as shown in Fig. 3.1(c). Thanks to the known width of the channel, appearing in the plan view image, it is possible to know the real separation between the lines, the position of the flat plate with respect to their beginning and the total amount of lines that will be digitally processed, because any of them could lie out of the channel width.

Afterwards, the information of the XY-plane is loaded, and shown in a Matlab figure, by means of the library "patternXY". First of all, the image with the pattern placed in the first line is loaded, with whichever angle the camera has, Fig. 3.1(a), together with another image that has the same point pattern but with all the points placed in horizontal and vertical, as shown in Fig. 3.1(d). Now, the user is asked to use the mouse to match pairs of the same points in both pictures, being necessary, at least, six points. One instant of this process can be seen in Fig. 3.5. After this, a bilinear transformation is used to transform the image of the target in the channel in order to have all its points seen without distortion, that is, to have the target seen by the camera but projected in a vertical plane. This is done by a transformation

matrix given by:
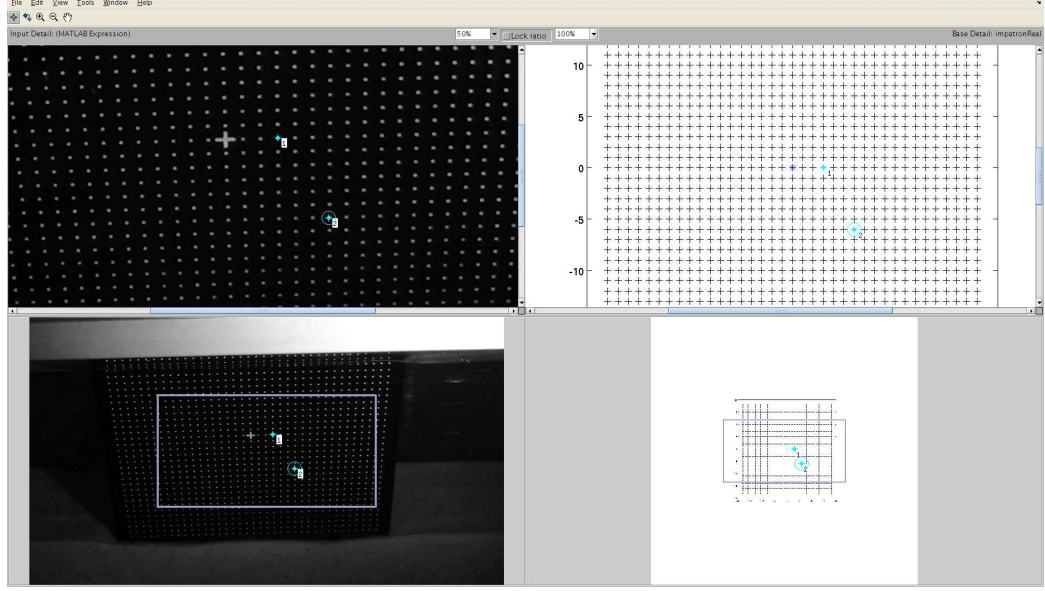
Figure 3.5: Selecting the matched points.

$$\begin{bmatrix} u & v \end{bmatrix} = \begin{bmatrix} 1 & x & y & x*y & x^2 & y^2 \end{bmatrix} * \begin{pmatrix} a & b & c \\ d & e & f \\ g & h & i \end{pmatrix}, \qquad (3.1)$$

where u and v are the coordinates of the matched points in the distorted image to transform, and x and y are the coordinates of the points in the image with the aligned points. The matrix coefficients (a,b,c...) are 12 unknowns needed to make the matrix of transformation, and that is the reason why, at least, 12 points (six pairs) are needed. The corresponding subroutine to do this is commented in Appendix B.

Once the coefficients are known, it is possible to project any image to the vertical plane, as it can be seen in Fig. 3.6, where the bilinear transformation is applied to one of images of the target. Since the angle of the camera does not change during the test, this transformation can be also applied to the

last image taken by the camera, that with the lines projected on the eroded bottom.

<div align="center">(a)   (b)</div>
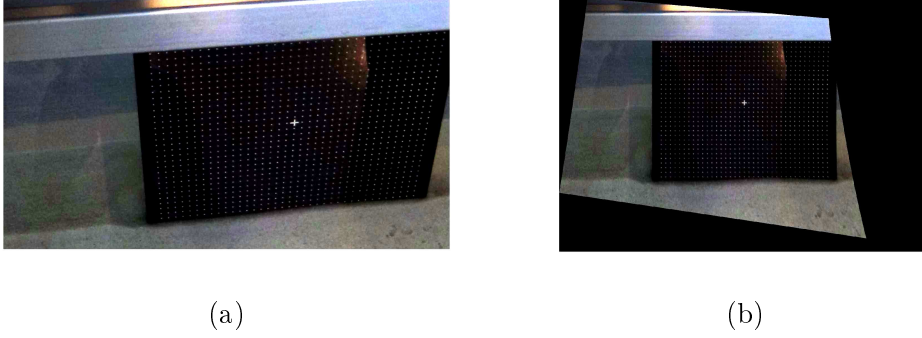
Figure 3.6: Target transformation to be vertically projected: (a) Seen by the camera; (b) After the bilinear transformation is applied.

Next, the code converts the images loaded in pixels to length dimensions, mm in our case, in order to be able to have dimensional profiles of the eroded bottom as well as of the size of the eroded region. To do that, a ratio pixel-mm must be found. The only important thing one has to take into account is that different lines will have different pixel-mm ratios, but this ratio is linear with depth (x coordinate) and the code is able to calculate it. To do it, the code needs, at least, another different image of the target to calculate the pixel-mm ratio. That is the reason why a second image of the target, located in the last projected line, must be taken. In order to know the pixel-mm ratio, the software asks the user for known distances in both target images, the ones shown in Fig. 3.1(a) and Fig. 3.1(b), and since the relative location of the dots in the targets are known, they will be used to obtain pixel-mm ratio in both planes and also its linear variations with depth.

The next step the software does is the automatic recognition of the projected lines on the sandy bottom. The value of the light intensity of each pixel of the image is extracted and is considered only as part of a line if it

exceeds a threshold value set by the user at the initialization step. There is an iterative process where the user can modify these parameters until a good result is obtained. It is important that the lines have a greater luminous intensity than the rest of the image, so that the code is able to automatically identify which pixels are part of a line. There are further information of the automatic recognition of the lines in the Appendix C. Once the line recognition is made, the code shows a figure with the lines as differentiated objects by colours of agglomerates of isolated pixels, as can be seen in Fig. 3.7, where the projected lines of Fig. 3.4(b) have been recognized. At the end, a filter is applied to remove objects with a number of pixels below a user defined value, and to avoid fake objects due to noise in the image.
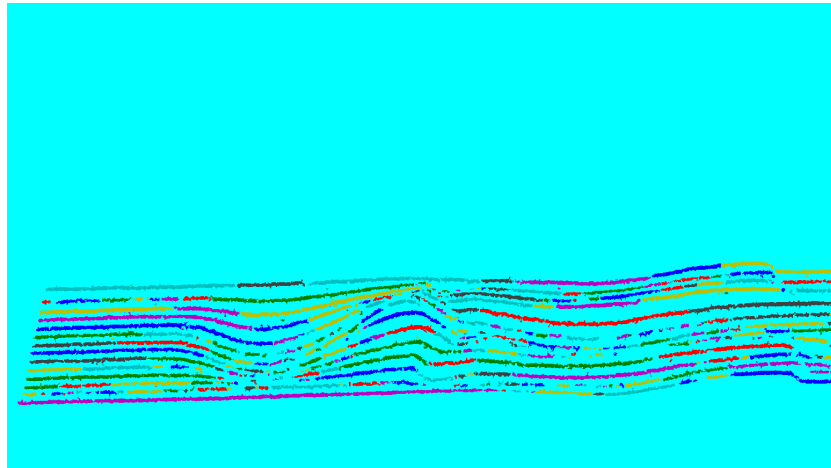
Figure 3.7: Projected lines once they have been recognized by the software. Different colours indicate different objects.

Now, and by means of an iterative process, the threshold value of the luminous pixel intensity to be considered as part of an object is modified automatically, as well as the minimum number of pixels an object must have in order to be accepted as such entity.

The next step is to specify which objects belong to the same projected

line. Thanks to this process, the lines are finally defined as a unique entity
and next, the user specifies the number of visible lines in the image in order
to know the real distance along the z-axis from the first to last one.

Next, the code calculates the lines as a set of points in two ways, de-
pending on the choice the user did at the beginning of the process. The first
option is that which uses just one image corresponding to the steady state
of the eroded bottom. What the software does with this image is to convert
the pixels of the same lines into points with their corresponding coordinates.
The second option uses the image at the beginning and at the end of the
test. Again, the pixels are converted into points and, the different between
both states can be calculated, see Appendix D for further information.

The way the software obtain the coordinates of the points of the lines is
by automatically detecting a whole line and getting, for each x-coordinate
of the line, a mean y-value based on its thick. With this step, not only the
mean y-coordinate is obtained, but also its corresponding error proportional
to the thick of the line. If a line had hidden parts, they are interpolated with
the other visible parts of it, as it is described in Appendix D.

Once all the operations are done, the x,y,z coordinates of the eroded
3D surface are known, and from them, any information related with the
surface, such as, their maximum or minimum values, contour curves, volume
of eroded regions, plots of longitudinal profiles along any coordinate, etc, can
be obtained.
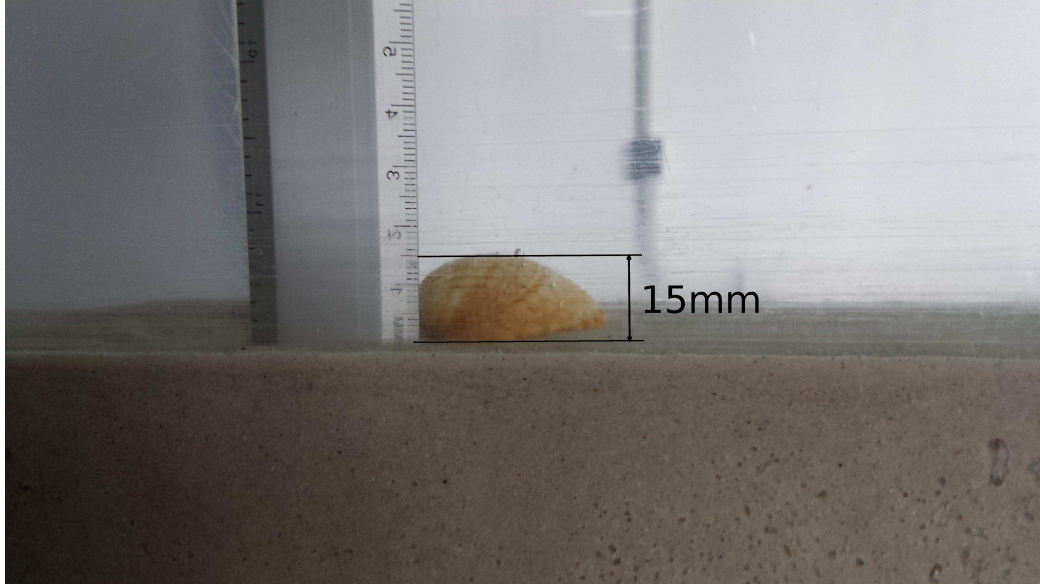
Figure 3.8: Frontal view of the seashell.

3.4 Validation of the methodology. Shape reconstruction of a seashell.

A seashell, located underwater in a sand bed, has been selected to validate the methodology to reconstruct 3D underwater surfaces. The seashell has known dimensions, thus we have digitized it using the technique developed in this Thesis, which will allow us to draw its level curves, reconstruct its 3D surface and also calculate the volume of the seashell.

The seashell, located on the sandy bottom of the channel together with a ruler to have an idea of its dimensions, can be seen in Fig. 3.8 and Fig. 3.9. From them, it is easy to see that the seashell has 15 mm high, 37 mm wide and 40 mm long. As it has been said previously, the reconstruction process needs some images to work correctly. In particular, once the camera has been set with an angle with respect to the channel, two images of the target must be taken, Fig. 3.1(a)-(b), and a plain view of the projected lines on the
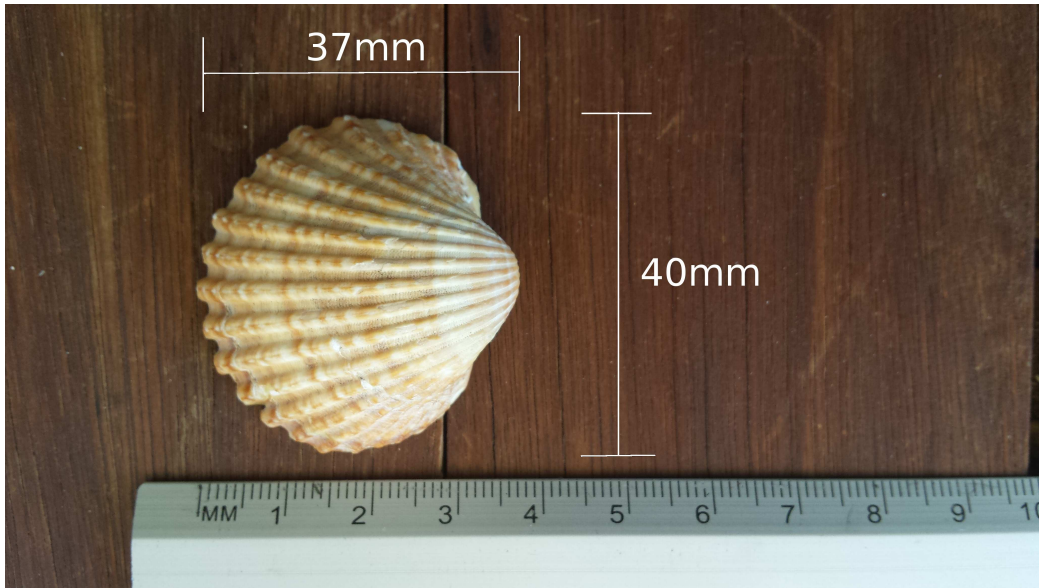
Figure 3.9: Plan view of the seashell.

flat bottom, Fig. 3.1(c). Once the two targets are analyzed and the bilinear transformation obtained, it is applied to the image of the seashell, which gives the result shown in Fig. 3.10. From this figure the different lines can be extracted as objects and its pixels converted in mm by means of the pixel-mm ratio obtained from the target images. When this is done, the surface can be reconstructed, but for now, with just the same number of lines projected on it. And, all this profiles can be also plotted together in a x-y plot (Fig. 3.11). This set of profiles can now be used to interpolate the height (y-coordinate) of any point in the x-z plane. Thanks to this, a 3D surface (Fig. 3.12), or a contour of iso-surfaces of constant height (Fig. 3.13) can be obtained. From these figures, the reconstructed values of its width, height and length can be obtained, giving 14.5 mm height, 37 mm width and 42 mm long, very close to the real ones of the object under study. From the digitized lines projected on the surface, the seashell in our case, the software also gives the error of each points which depends on the width of the line. In Fig. 3.14 is depicted
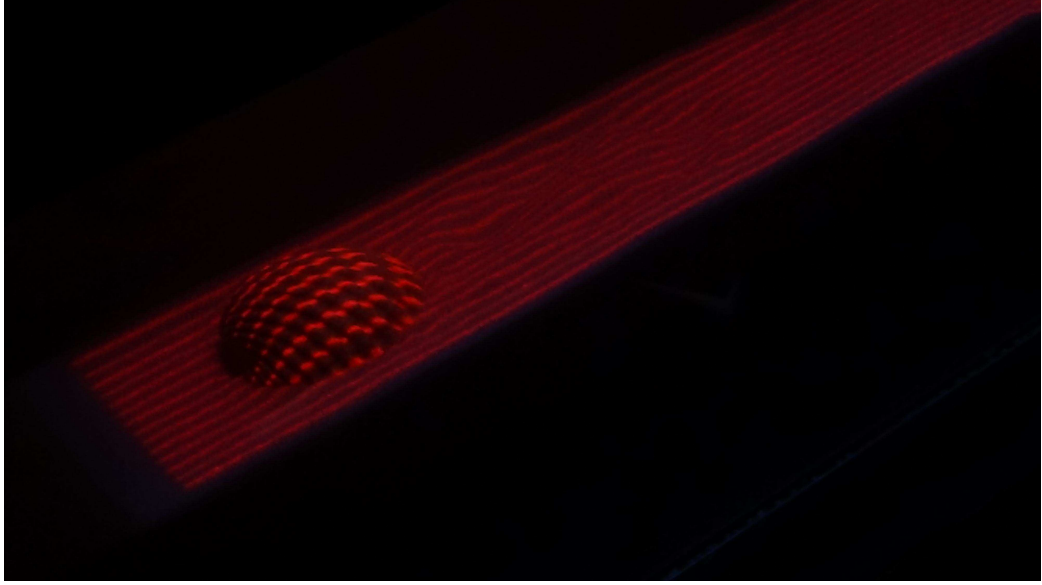
Figure 3.10: Seashell lighted by the projected lines

the profile of the seashell along its middle with the corresponding errorbars. The mean error for this profile was 0.5952, while for all the seashell surface was 0.6170.

In addition, the software can also calculate the volume of a certain region of the surface. In our case, the volume inside the seashell will be calculated in order to compare it with the real one to have an idea of how accuracy of the proposed methodology is. First of all, this volume has been calculated experimentally with a syringe and fulling of water the cavity of the seashell, see Fig. 3.15. The result of the experimental measured volume inside the seashell was 7068 mm^3. And the result given by the software was 7290 mm^3, which means an error of about 3%. The difference with respect to the real value is due to the thick of the seashell, that it has not been taken into account in the experimental calculation.
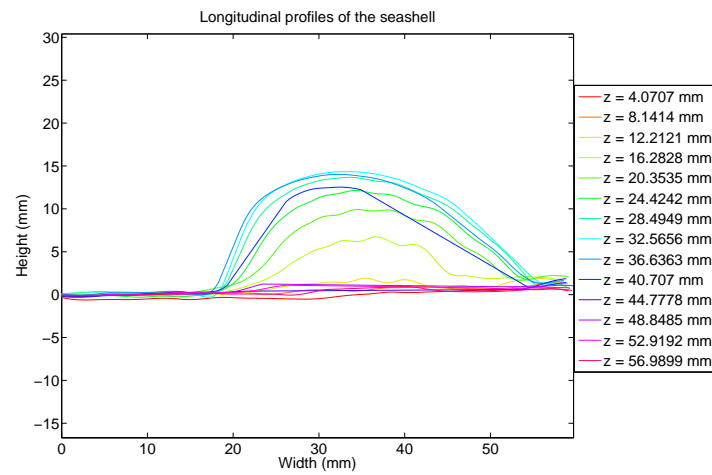
Figure 3.11: Longitudinal profiles of the seashell shape for the z values given in the legend.
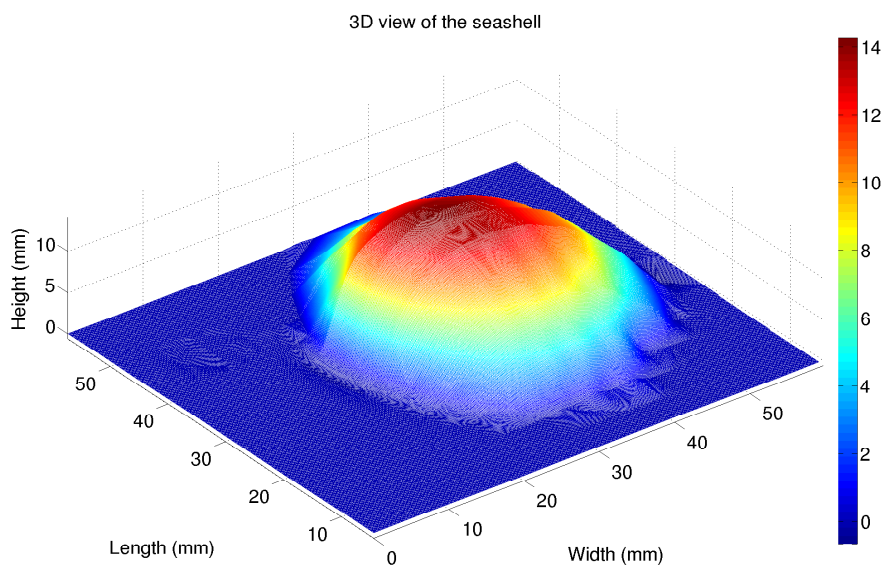
Figure 3.12: Reconstructed 3D surface of the seashell.
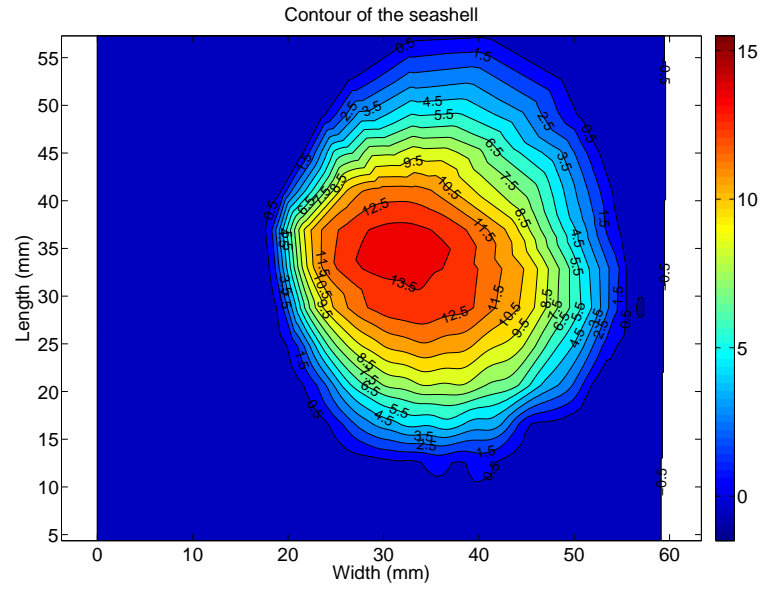
Figure 3.13: Contour curves of the seashell.
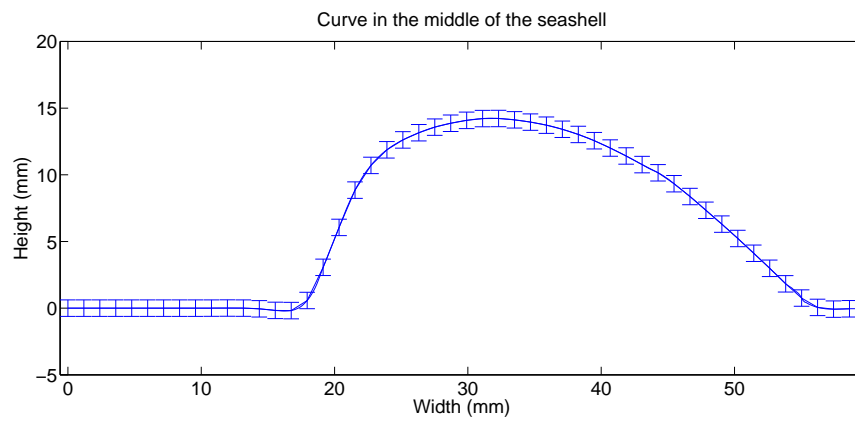
Figure 3.14: 2D profile in the middle of the seashell with the error bar.

Figure 3.15: Method to calculate the volume of the seashell cavity.

3.5   Summary and conclusions

To analyze digitally the eroded surface by the presence of flat plates in a tidal current, it has been necessary to develop a method and a computer program to reconstruct 3D underwater surfaces. The method has been validated with the dimensions of a seashell and it has been shown to be valid for scanning 3D surfaces with an accuracy proportional to the thickness of the lines projected on the surface to reconstruct. The error did not exceed the value of 1 mm in the validation sample (5% with respect to the flat plate chord). The software also can calculate the maximum and minimum values of the surface in the vertical direction, either absolute or in a small region, as well as, calculate volumes of different regions of the surface.

This methodology may be accepted with these results knowing that the error is less than 5%, depending the thick of the projected line, and assuming that the final picture does not have hidden parts of the lines. If this happens, the hidden parts can be interpolated.

Finally, we can conclude saying that this method is valid for digitizing

continuous surfaces, without too much sharp edges, as long as the image taken by the camera have not too much hidden parts, in order to minimize the error. This method is also recommended for studies of surfaces which have difficult access to take the images of their surface, avoiding also the problems of the diffraction of light due to the media change. Another important advantage of this technique is that the error is really tiny and proportional to the line thickness and space between them, getting errors of the order of 1 mm (5% with respect to the flat plate chord).

Chapter 4

Experimental measurements of the scour generated by a flat plate over a sand bed

4.1 Introduction

Scours on the sea or river beds, originated by the presence of either floating or touching structures near their bottom, is the focus of interest of many researches in order to protect not only the environment but also the structure (Whitehouse, 1998). There are, for instance, a lot of previous works that have studied the scour generated by submerged pipelines on the seabed either experimentally (Mao, 1987), or numerically (Brørs, 1999; Li & Cheng, 1999), or even there are empirical functions to predict the maximum scour depth due to submerged pipelines for a given current (Chiew, 1991). Others authors, however, have studied the scour made by submerged piles when they are anchored to the bottom (Melville & Coleman, 2000; Roulund *et al.*, 2005; Khosronejad *et al.*, 2012). However, the lack of detailed suspended object

studies inside the water and close to the sea/river bottom encourages the present research. Only very few works have been found about this topic, such as the ones done by Gao *et al.* (2006),Gonzalez-Juez *et al.* (2009). But, this is not our only motivation, because tidal energy converters frequently use sails to extract energy from the current and they could be so close to the bottom that the effect on it could be important. Thus, from an environmental point of view, it can be interesting to know the height above which the impact on the bottom can be neglected.

In this chapter, we use the software and methodology developed and explained in Chapter 3 to reconstruct underwater 3D surfaces and so digitize the scour produced by the flat plate model described in the Chapter 2.

The goal in this chapter is, thus, to be able to quantify the erosion on a sandy bottom due to the presence of a steady flat plate in a tidal current, and located close to the bottom. The governing parameters of the problem are the angle between the flat plate and the current, α, and the separation of the flat plate with respect to the sandy bottom, h. It is also considered to be perfectly flat, so that any disturbance on it will be assume to be due to effect of the flow around the plate. Regarding the sand used in the sediment channel (SiO_2 with M.=60.09), it has got a mean diameter of $d_{50} = 0.3$ mm, a loss on drying of 0.2%, and the soluble matter in HCl is 0.2%(a size considered as medium sand) (Merriam, 2003; Krumbein & Aberdeen, 1937).

4.2   Experimental set-up

The study described in this chapter has been carried out in a sediment water channel, with the sand located at its bottom. In fact, only a central fraction of the channel was used, with a wedge at the beginning and end of the sand

region to gradually adapt the flow to and from the sand region. An sketch of the experimental set-up can be seen in Fig. 4.1, where not only the channel but also the hydraulic circuit, the camera to take the photos, and the video projector to draw the lines on the sand, are shown.
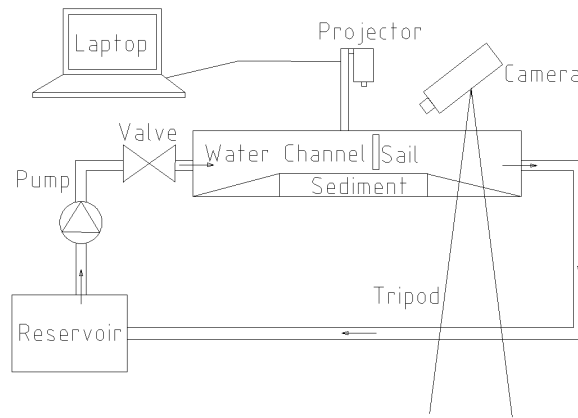
Figure 4.1: Sketch of the water channel.

Water flows through the channel thanks to a pump with a maximum flow rate of 5330 l/h. This flow can be regulated by a valve. In this work the maximum flow rate is used in order to have a Reynolds number as big as possible. A reservoir, located on the laboratory floor, allows to close the hydraulic circuit, storing the water to be recirculated later during the experiment. As one can see in Fig. 4.1, the flat plate is located above the sand, and it is mounted in a mechanism which allows to adjust both the angle of the plate and its distance to the sand. A video projector, fixed on the channel structure, is used to project the lines on the sand that will serve to scan the 3D eroded surface, as explained in the Chapter 3. The projected image with the lines can be generated by any commonly used graphic software (see Fig. 3.1(c)) and it is sent to the projector by a computer, which also will be used later to process all the images. Finally, a camera, mounted on

a tripod, and with an angle with respect to the channel, is used to take the photos needed to reconstruct the shape of the 3D surface. It must be noted that the camera must remains steady (its relative position to the channel and its angle) during the time the experiment takes place.

The channel is 65 mm wide and 260 mm high. Its total length is 2580 mm, while the central test region with a sand is only 95 mm high and 775 mm long (see Fig. 4.1). The height of the sand layer is 130 mm, so that the water depth in the sand region is 130 mm. Using the maximum pump flow rate of around 5330 l/h and the water channel section above the sand of around 65x130 mm one can calculate the mean (characteristic) velocity of the water, U, giving a value of around 0.18 m/s. Taking also into account the kinematic viscosity, ν, of water at working temperature and using the chord, c (= 20 mm), of the plate as the characteristic length, the Reynolds number of the flow, defined as

$$Re = \frac{Uc}{\nu},\tag{4.1}$$

is around 3500. All the results have been obtained at this maximum Reynolds number. So that, for future works, it is recommended to try to increase this value to see how different the erosion process and the resulting eroded surface are.

For this Reynolds number, it has been observed that when the water flows without any submerged obstacle at the maximum pump flow rate, it is not able to resuspend the sand, or in other words, to make any erosion, so we can assume that any scour generated on the sand surface is made by the presence of the obstacle (the flat plate in our case). Regarding the size ratio between the sand and the plate, the former is about 67 times smaller than chord of the latter, which is considered as a representative case of a real tidal energy extraction system mounted above the seabed compared with a fine sand.

In Fig. 4.2 is depicted a sketch of the experimental configuration, with two views of the central region of the channel just where the plate is mounted. Here, it is easy to see the angle α between the plate and the current, and the distance h from the plate to sand. The plate is 1 mm thick and made by steel.

(a) Plan view

(b) Front view
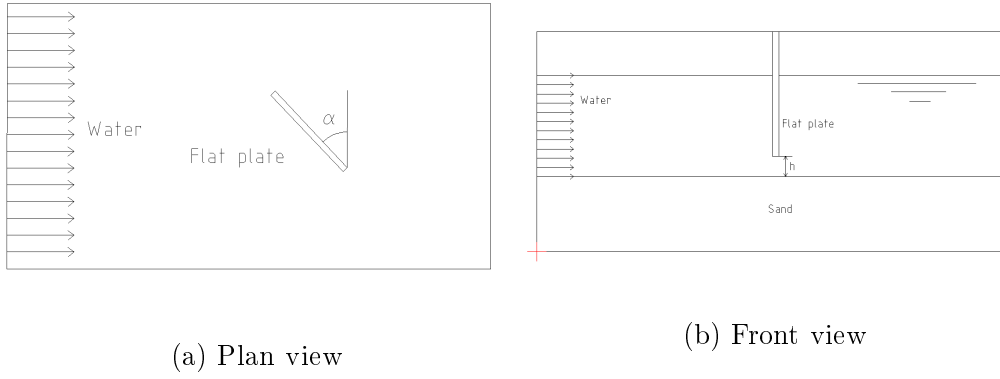
Figure 4.2: Sketch of the problem to study in the hydraulic channel

We have carried out a set of experiment with different angle values of the plate, starting at 0°, which is the one that causes the maximum erosion, as it will be shown later. Other angles used are 30°, 45°, and 60°, the later causing very little erosion on the sand. We have also tested, for each angle, different plate-to-sand distances, starting from 0 mm, with the plate standing just on the sand, and increasing the distance every 2 mm until no erosion is observed.

4.3   Results and Discussion

The results for a series of experiments for $Re \simeq 3500$ and different values of α and h are presented here. For this Reynolds number, and as we will see later, it is important to take into account that the vortices emerging from

both sides of the plate could play an important role on the erosion process.

When manipulating images to extract from them information, as we are going to do, it is important to think about the most important sources of error: a right lighting projector, the image quality and resolution, the good horizontal and vertical alignment of the targets before shotting the camera to get an image of them, the initial flatness of the sand, independently the method chosen uses, the difference between the initial and final sand state, the thickness and number of the projected lines, and the angle of the camera to be able to capture the whole lines avoiding, if possible, their hidden parts. However, the most important, because it has a high impact on the results, is the error due to the thickness and number of projected lines. This error will be quantify later for each experiment.

We have studied 4 values of the angle of attack α (=0º, 30º, 45º, 60º), and 9 plate-to-sand distances, ranging from $0c$ to $0.8c$, at intervals of $0.1c$. However, for each angle, the highest distance used is that for which no erosion on the sand was found, so that above it, the sand bed remains unchanged. As it will be shown later, the highest distance for that to happen decreases when the angle increases, that is, it decreases with the alignment of the plate with the current. That is the reason why at large angles the number of studied distances are fewer. The discussion of the results will be done by means of the reconstructed 3D surfaces of the sandy bottom given by the software developed in this Thesis.

In Fig. 4.3 is depicted the 3D surface for a plate configuration and it is going to be used to define some sand structures observed in all experiments, such as the first and second scours, first dune, side scours, and side and longitudinal dunes, as well as, some comments about the colours of the surface. Regarding the later, green colors indicate the unperturbed origi-
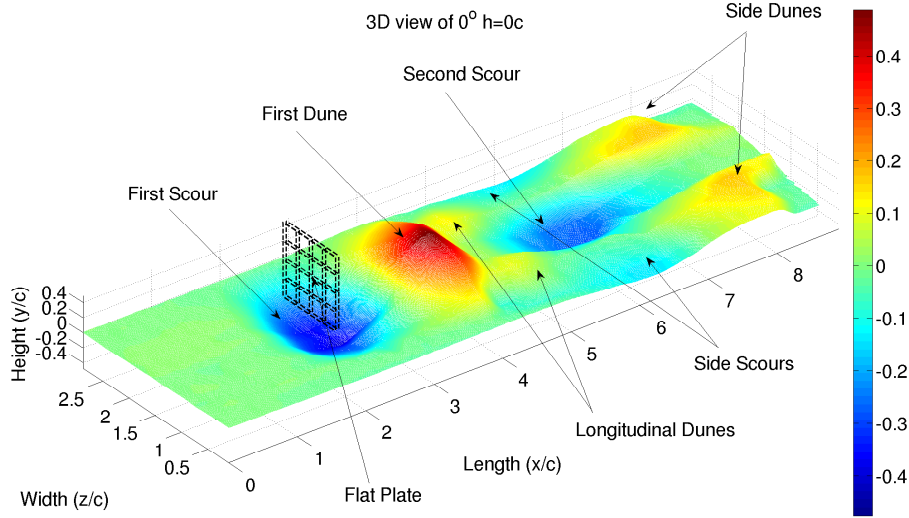
Figure 4.3: Reconstructed 3D surface of bottom for $\alpha = 0^{\circ}$ at $h = 0c$. Some comments have been included to identified the structures of the sand.

nal sand, whereas blue ones erosion zones and reddish yellow deposition of eroded sand (mountains). In addition to this, the software also draws the real position and orientation of the plate, as a transparent grid, for a better understanding of the results. For all plate angles, the axis scale in all figures will be the same in order to be able to compare the resulting erosion on the sand. To start with, the angle $\alpha = 0^{\circ}$, and the different studied distances from the plate to sand bed, $h = 0c$, $0.1c$, $0.3c$ and $0.6c$, will be presented. However, most of the subsequent result are presented in Appendix E. The bottom reconstruction, once the sand reaches a steady state, can be seen in Fig. 4.4. As one can see, all figures present a symmetry line along the middle (symmetry line) of the channel, and the observed pattern of the sand in the steady state is quite similar in all of them. Starting with the plate standing on the sandy bottom, Fig. 4.4(a), what one observes is that, first

of all, a deep scour appears just under the flat plate, whose depth decreases, as it will be seen later, when the plate-to-sand distance increases. Secondly, and downstream the first scour, a sand elevation or dune appears, which is thought to be originated by the sand re-suspension from the first scour. Thirdly, a second scour appears downstream the first dune due to the flow acceleration when leaving it. This second scour is also surrounding by two small longitudinal dunes, which extend from the first dune to two new side dunes located downstream the second scour and preceded by two side scours. These two both side dunes and scours seem to extend until the lateral walls of the channel. This fact means that the channel walls are playing an important role on how the sides of the eroded bottom looks like. If the channel had been wider what we would have found is also a wider erosion zone. Nevertheless, the main changes on the bottom, those like the first and second scour, and the first dune, are not affected by the channel lateral walls. Probably, both the side dunes and scours would have been wider, but still appearing as effect of the presence of the plate. In this point, it is important to wonder about the mechanism responsible of the side scours and dunes. It is believed that these side structures are due to the tip vortices emerging from the flat plate sides, giving rise to the first dune not to extend laterally too much, and, downstream of it, to a sand suspension (side scours) and then to its deposition (side dunes). This explanation will be reinforce later when other flat plate angles are discussed.

What one observes when the distance between the plate and the sand is increased is that all sizes of the different dunes and scours are reduced, as it can be seen in Fig. 4.4, for distances ranging from $0.3c$ to $0.6c$. This effect can be also seen in Fig. 4.5, where longitudinal sand bed profiles for 3 different values of z, $z_m \equiv z = 1.625c$ (the middle of the channel) and $z = z_m \pm 0.8125c$,

are depicted for all plate-to-sand distances. However, since the axis scale is the same in all figures, it is remarkable that when $h = 0.3c$ the side scours are a little deeper than for the smaller previous separation. This is thought to be because, for this distance between the sand and the plate, the tip vortices are stronger than for any other distance, having the highest erosion capacity. To see this effect clearly, in Fig. 4.6 is depicted the spanwise sand profile at $x = 6c$, around $3.6c$ from the plate, of the flat plate, where the side scours have their maximum depth. As commented on and shown in Fig. 4.6, for $h = 0.3c$ the side scour is the deepest.

Next, how the angle of attack of the plate, α, affects on the sand erosion will be commented. To that end, only some new pictures of the 3D bottom surface will be included in what follows, being all the remaining images included in Appendix E. When $\alpha = 30^o$, the size of the eroded region is smaller in comparison with respect to $\alpha = 0^o$, not only in the streamwise direction, but also in the spanwise one. In Fig. E.4(a) is depicted the 3D surface of the bottom when $h = 0c$, and one can see the depth, height and width of the eroded region is smaller than when $\alpha = 0^o$ (see Fig. 4.4(a)). However, and as it before happened for $\alpha = 0^o$, when the plate-to-nozzle separation increases, all the sizes of the dunes and scours decrease. It is important to notice, how the eroded region takes place just behind the plate, being also smaller across the channel, loosing even the symmetry it had when $\alpha = 0^o$. One can also see in Fig. E.5(e),(f), how the needed plate separation from sand to not erode the bottom is smaller when the angle increases, and for this $\alpha = 30^o$ when h is greater than $0.6c$ the bottom is hardly eroded, see Fig. E.5(e),(f). In addition to all this, it can also be observed the role of the tip vortex from the plate sides, as Fig. E.4(g),(h) reveals, where side scours and dunes due to that phenomenon again appears downstream the plate. When the angle
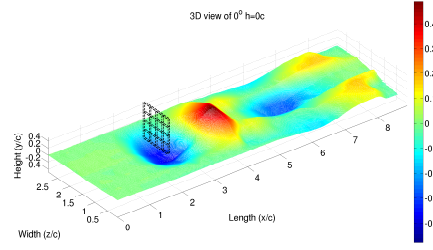
(a) $h = 0c$
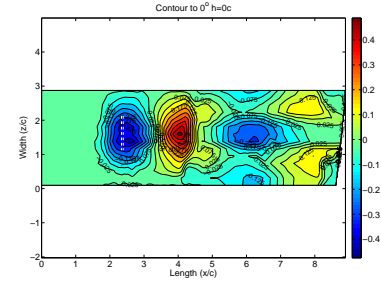
(b) $h = 0c$
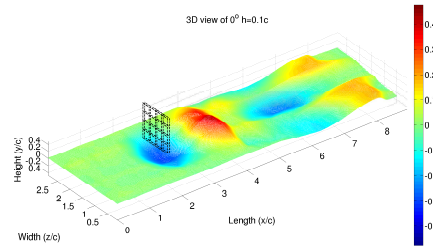
(c) $h = 0.1c$
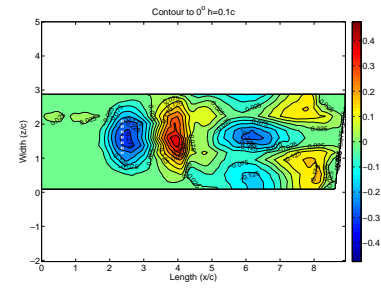
(d) $h = 0.1c$
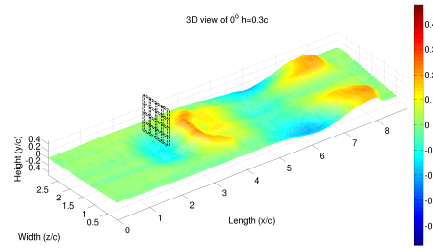
(e) $h = 0.3c$
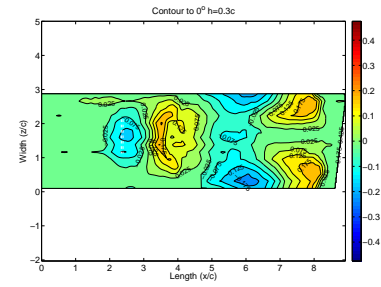
(f) $h = 0.3c$
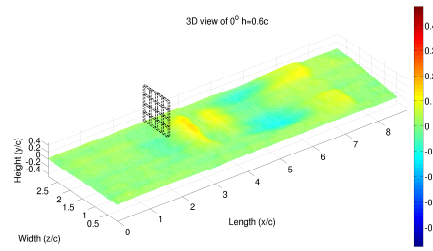
(g) $h = 0.6c$
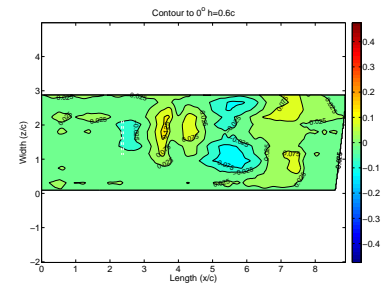
(h) $h = 0.6c$

Figure 4.4: Reconstructed 3D images of the surface and the contour for $\alpha = 0^{\circ}$ and the values of h indicated.
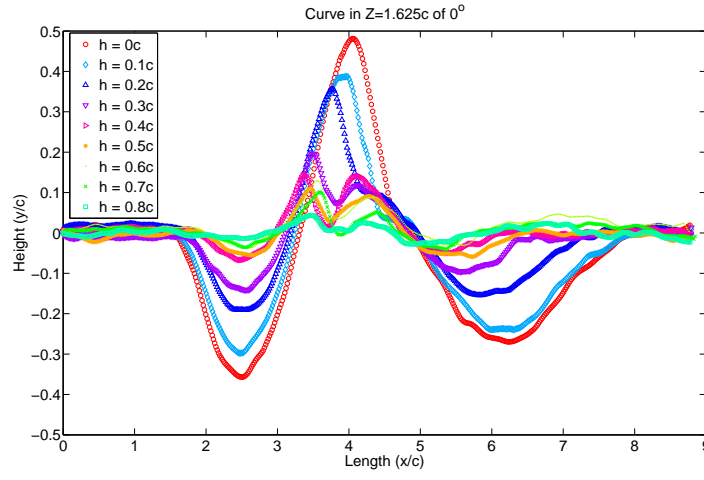
(a) $z = 1.625c$
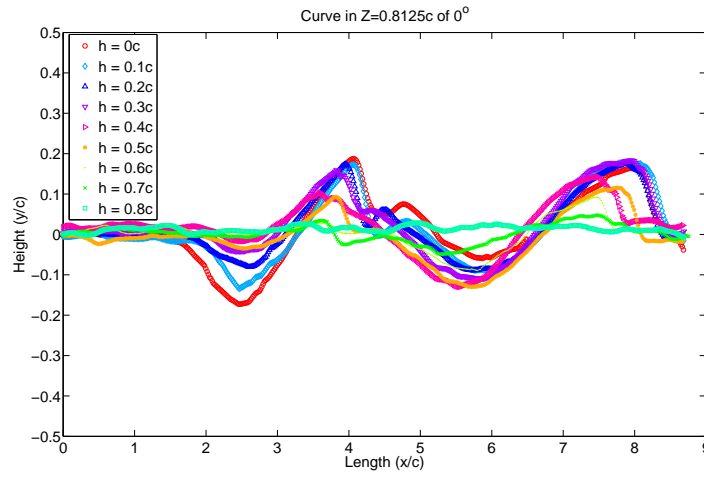
(b) $z = 0.8125c$
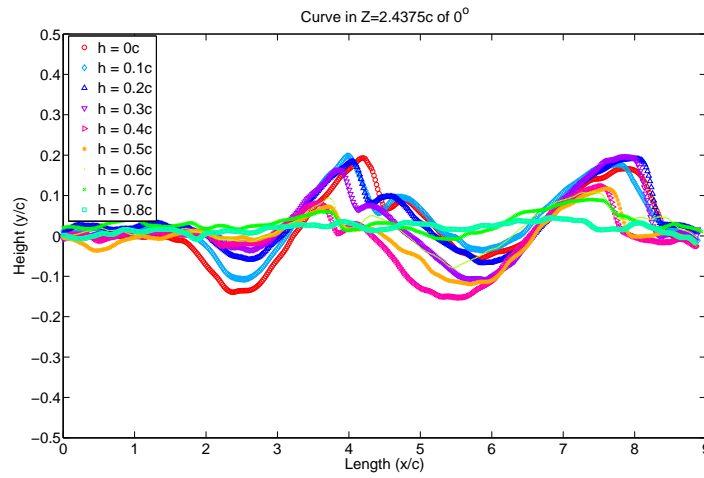
(c) $z = 2.4375c$

Figure 4.5: Sand bed profiles in (a) the middle of the channel (b) 1/4 of the channel width (c) 3/4 of the channel width with $\alpha = 0^o$
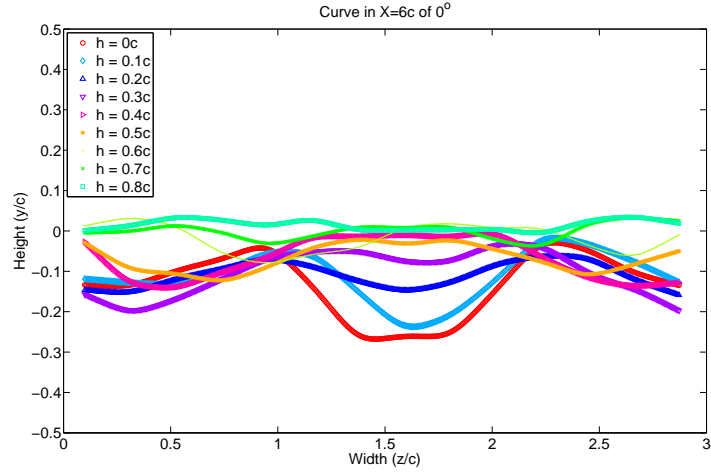
Figure 4.6: Spanwise profiles for $\alpha = 0^o$ and the plate-to-sand distances indicated in the legend.

of the plate continues to increase to 45° (or 60°) the size of the eroded region decreases, and even more when the nozzle-to-plate distance increases, as it can be seen in Fig. E.6(a),(b),(e),(f) and Fig. E.8(a),(b),(e),(f), for $\alpha = 45^o$ and 60°, respectively, where the surface shape for $h = 0c$ and the highest value of h, for each angle, is shown.

Once the results for each of the studied angles have been independently discussed, in what follows, we are going to compare the erosion produced for a given nozzle-to-plate separation as a function of the angle of attack of the plate. There are three distances ($h = 0c$, $0.1c$ and $0.2c$) that were studied for all angles, so it is going to be drawn stream and spanwise profiles of the bottom in order to compare relatively the produced erosion on the sand. On the one hand, Fig. 4.7 depicted the streamwise profile of the bottom along the middle of the channel, whereas Fig. 4.8, Fig. 4.9 and Fig. 4.10 depict spanwise profiles at three x locations from the flat plate position at $0c$, $1c$ and $4c$. These figures also include and sketch the flat plate in dash lines. If
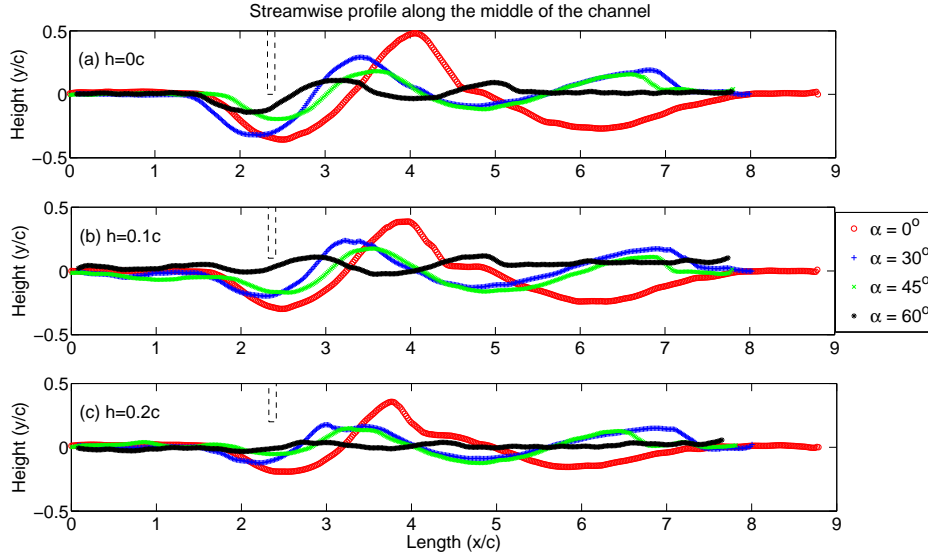
Figure 4.7: Streamwise profile of the bottom along the middle of the channel for different angles: (a) $h = 0c$; (b) $h = 0.1c$; and (c) $h = 0.2c$.

we look along the symmetry line of the channel, Fig. 4.7, it is observed that for $h = 0c$, subfigure (a), the first dune length is different depending on the angle of attack of the plate, and the higher the angle is, the closer the dune is to the flat plate. In addition, there is a second dune as soon as the flat plate has a different angle of 0º, because of the symmetry of the erosion, that it has been broken for $\alpha = 30$º, 45º and 60º. However, for $h = 0.1c$, subfigure (b), there is a reduction in size of the scour and the dune generated for all the angles, and for $h = 0.2c$, subfigure (c), in the case of $\alpha = 60$º the scour is nearly null, while for the other angles the eroded surface has the same shape but different dimensions. All these comments can be also supported by the contour surfaces for constant values of y shown in Fig. 4.11 for $h = 0c$ and all angles, where it has also been included a sketch of the plate. These figures show how the size of the eroded region is smaller as the angle of the plate increases.
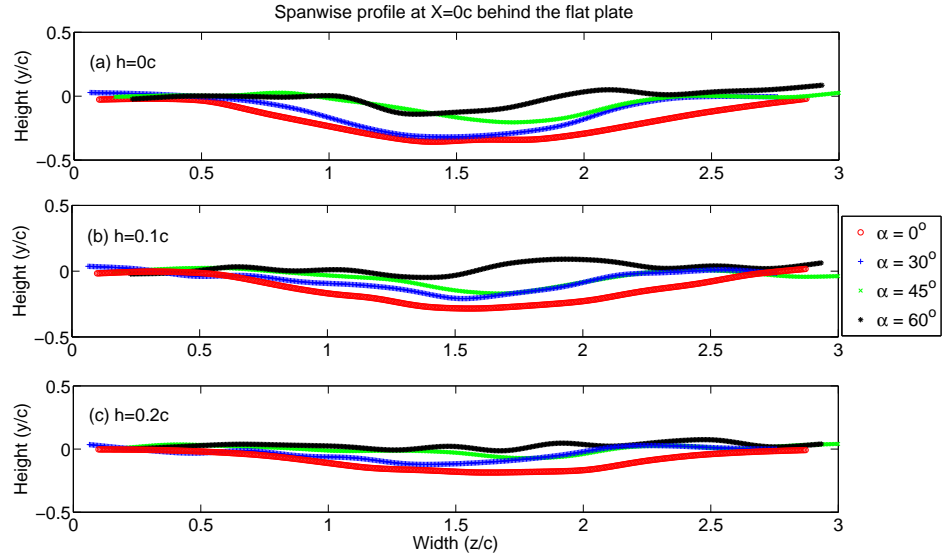
Figure 4.8: Spanwise profile of the bottom at a distance $0c$ downstream the flat plate for different angles: (a) $h = 0c$; (b) $h = 0.1c$; and (c) $h = 0.2c$.
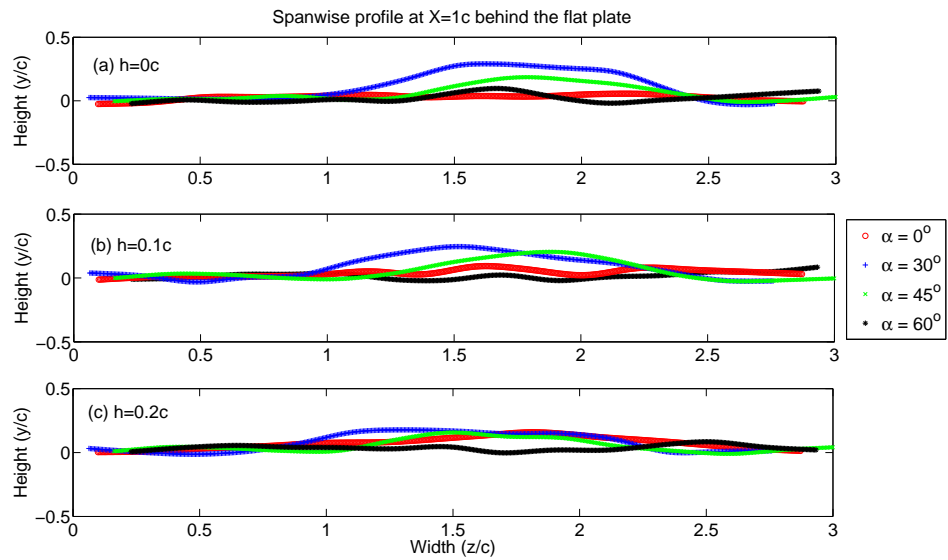
Figure 4.9: Spanwise profile of the bottom at a distance c downstream the flat plate for different angles: (a) $h = 0c$; (b) $h = 0.1c$; and (c) $h = 0.2c$.
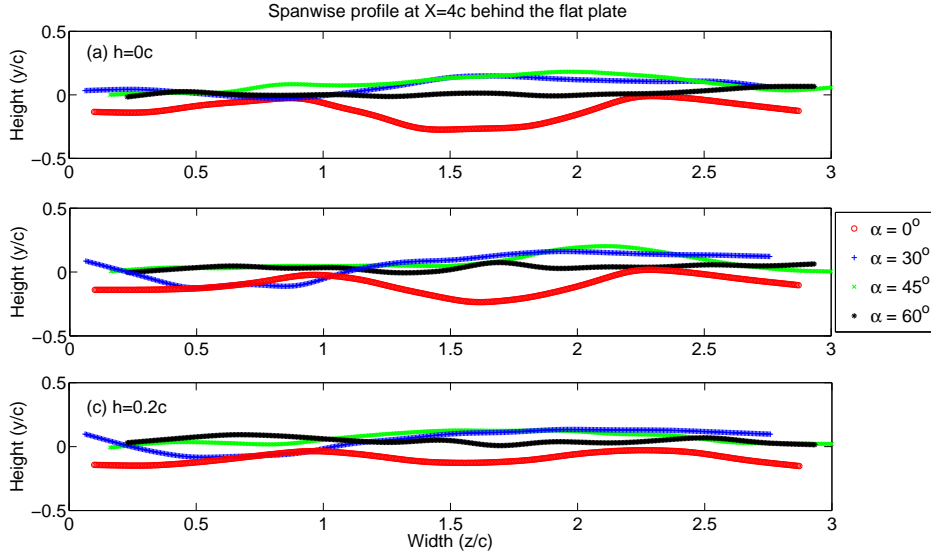
Figure 4.10: Spanwise profile of the bottom at a distance $4c$ downstream the flat plate for different angles: (a) $h = 0c$; (b) $h = 0.1c$; and (c) $h = 0.2c$.

On the other hand, regarding the spanwise profiles, the first ones are extracted from just under the plate, at $x \simeq 2.4c$, Fig. 4.8, and the other two a little downstream, that is at $x = 1c$ and $4c$ from the flat plate, Fig. 4.9 and Fig. 4.10, respectively. As one can see, the higher the value of the angle, the higher the scour depth, under the flat plate, see Fig. 4.8. However, downstream the plate, at $x = 1c$, the dune height is higher with the flat plate angle of $\alpha = 30°$ than for $\alpha = 0°$, because this distance is not the top of the dune for $\alpha = 0°$ but is for the $30°$. At $4c$ downstream the plate, Fig. 4.10, the second scour has its maximum depth for $\alpha = 0°$, while for the other angles there is a dune. However, for an angle of $60°$, the surface is nearly flat regardless of the plate-to-sand distance.

Thanks to the software developed, we can also calculate the maximum and the minimum values of non-uniform surface, as well as the volume of the scours and dunes generated on the sand.

(a) $\alpha = 0^o$

(b) $\alpha = 30^o$

(c) $\alpha = 45^o$

(d) $\alpha = 60^o$
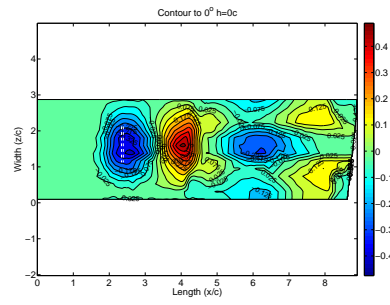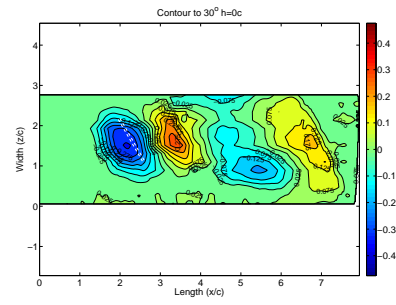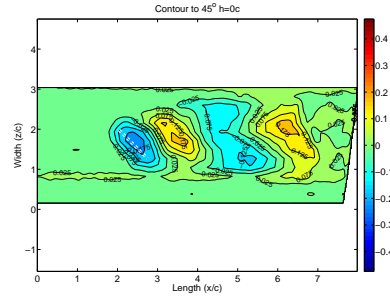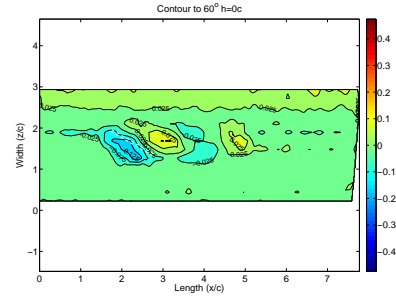
Figure 4.11: Isosurfaces of constant height for $h = 0c$ and the values of α indicated.
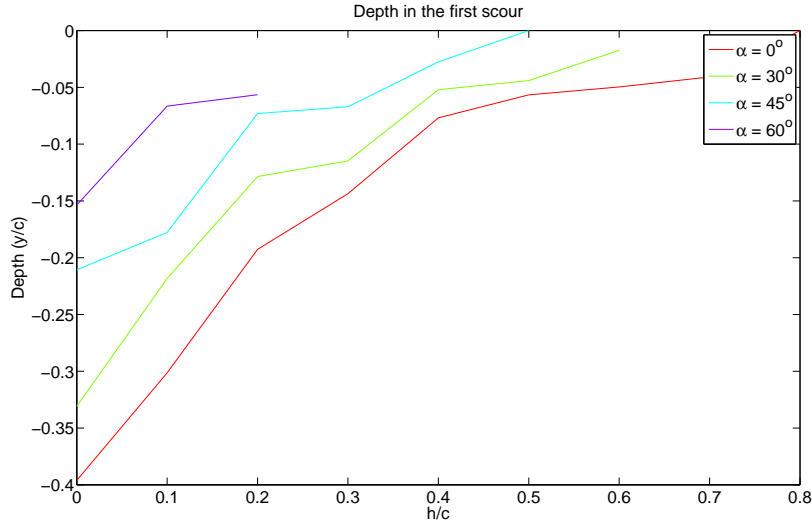
Figure 4.12: First scour depth for $\alpha = 0^o$, 30°, 45° and 60° as a function of h.

However, instead of plotting the absolute maximum of the surface, it is better to obtain the maximum depth of the first scour to see how it changes with h and α. Its evolution is depicted in Fig. 4.12. Once more, it is confirmed that the higher the angle of attack, the lower the depth of the first scour.

Downstream the first scour a dune is generated by the sand re-suspension. In Fig. 4.13 is depicted how its maximum height to see how it changes with h and α. As expected, the higher the value of α, the smaller the height of the dune for whatever value of h.

It could be also interesting to know the volume of sand extracted from the eroded scours and that of the generated dunes. This can be also obtained from the software developed. Fig. 4.14 shows the sand volume evolution of the first scour under the flat plate as a function of h for each angle of the plate. It can be seen how the size of the scour, and then its volume, decreases rapidly when the angle increases, being, as expected, the angle 0 the one with
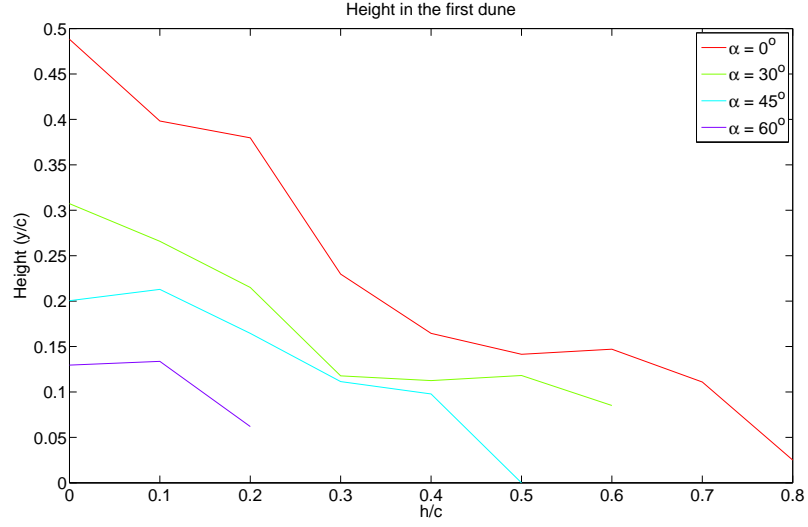
Figure 4.13: Height in the first scour for $\alpha = 0°$, $30°$, $45°$ and $60°$ as a function of h.

more capacity of erosion.

If we now represent the volume of the first dune, we will have the evolution shown in Fig. 4.15, where it is remarkable the nearly linear change of volume with the separation h, when $\alpha = 0°$.

It is important to have an idea the error of the above results. They can also be obtained from the software and depend mainly on the size of the digitized lines projected on the sand. The lower the width of these lines, the lower the error of the results. The mean error obtained in all experiments are summarized in Table 4.1, where one can see that are all quite similar. This is so because the thickness of the lines, the amount of these, and the separation are the same in all cases. The error is expressed in millimeters and the total average result of 0.4782 mm, which represents a 2.4% if it is made relative to the flat plate chord.
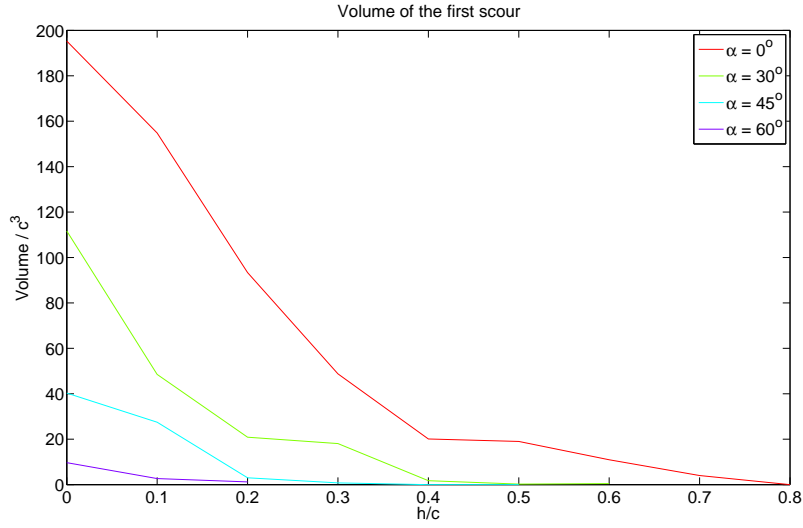
Figure 4.14: Volume of the first scour for $\alpha = 0^o$, 30°, 45° and 60° as a function of h.

Figure 4.15: Volume of the first dune for $\alpha = 0^o$, 30°, 45° and 60° as a function of h.

h (mm)	$\alpha = 0^{\text{o}}$ (mm)	$\alpha = 30^{\text{o}}$ (mm)	$\alpha = 45^{\text{o}}$ (mm)	$\alpha = 60^{\text{o}}$ (mm)
0	0.3896	0.4822	0.495	0.4417
2	0.5099	0.4833	0.5245	0.4761
4	0.3731	0.5368	0.521	0.4274
6	0.4659	0.4483	0.5223	-
8	0.4741	0.4623	0.5179	-
10	0.4563	0.5251	0.5189	-
12	0.4561	0.4754	-	-
14	0.4991	-	-	-
16	0.5176	-	-	-

Table 4.1: Mean error in the experimental tests (dimensions in mm)

Chapter 5

Closure

This chapter summarize all the results obtained in the work done in this doctoral thesis and propose a number of possible future works for further researches.

5.1 Conclusions

Throughout the work of the doctoral thesis, the effort has focused on improving the aerodynamics of a device used to extract energy from tidal currents, and on mitigating its environmental impact. Following these motivations, we have obtained the following results that are also explained in the respective chapters of this thesis:

- Different numerical simulations have been performed of a simplified model of the device that extract energy from a tidal current. This model consists on a cascade of flat plates moving perpendicular to the flow. In the simulations the Reynolds number and the semi-aspect ratio of the flat plates were kept constants, $Re = 5.66 \cdot 10^4$, and $sAR = 3$, respectively. The variables were the separation between the flat plates,

or solidity, σ, the velocity of the cascade relative to the current, ξ, and the blade angle of attack with respect to the current, γ. To carry out the numerical simulations it was also necessary to tune different turbulent model parameters to the experimental results of the flow around a single flat plate. In addition, a grid convergence study was done to find the optimum number of grid cells to perform simulations efficiently.

- An optimal configuration that extracts the maximum power, $\overline{C}_P$, from the current was found with the above constraints. It occurs when the stagger angle is $\gamma \approx 79^\circ$, the solidity is $\sigma \approx 1$ and the blades speed is $\xi \approx 2.5$. However, there is a second relative maximum value of $\overline{C}_P$, slightly smaller, when $\sigma \approx 1$, $\gamma \approx 75^\circ$ and $\xi \approx 1.5$ which is much more interesting for the configuration of the cascade of flat plates because the lower relative speed of the cascade. In either case, the optimum solidity is about unity and the best stagger angle around 75°.

- To analyze the eroded surface by the presence of flat plates in a tidal current, it has been necessary to develop a technique and a computer software to reconstruct 3D underwater surfaces. The method has been validated using a seashell of known dimensions, and it has been shown to be valid for scanning 3D surfaces with an accuracy error proportional to the thickness of the lines. From the image processing, the error did not exceed 1 mm in the validation sample (2.5% of the seashell chord). The developed software also gives the user possibility of getting quantitative data from the 3D surface such as the maximum and minimum values of the eroded surface, the volume of scours or dunes in different regions of the surface, etc.

- Regarding the potential erosion capacity of flat plates once they are running in a tidal energy extraction device, a hydraulic channel has been used to study experimentally the erosion by an isolate flat plate for a fixed value of the Reynolds number and for different heights of the flat plate with respect to the sandy bottom, and different angles of attack. Two different phenomena are found to develop the scour. The first one is the current flowing between the flat plate and the bottom, that generates a first scour under the plate, a dune downstream the scour, and a second scour. As the height of the flat plate with respect to the seabed is increased, the volume of eroded regions, given mainly by that of the first scour, decays exponentially. Moreover, the volume of the first dune also decreases linearly with h, specially for small angles of attack α. The second phenomenon involved is related to the vortices generated at both sides of the flat plate, responsible for the three scours for small angles α, between 0° and 30°. Above $\alpha = 30^{\text{o}}$, only two scours are generated and by the flat plate side vortices. We have quantitatively characterized in this thesis the sizes and distribution of these sand-bed scours and dunes as the angle of attack α and the distance from the plate to the bed h are varied.

5.2   Suggestions for future works

This thesis covers only some hydrodynamic aspects regarding a tidal energy system device based on submerged sails, leaving open for future research many other aspects. With respect to the aerodynamic of a cascade of flat plates, the possible future works could focus on the next points:

- Comparison of the numerical results with the experimental data for the

same configurations that have been studied numerically in this work.

- New numerical simulations of the flat plate cascade for different realistic Reynolds numbers to find out new configurations for which the maximum power can be extracted from the cascade.

- The semi-aspect ratio of the flat plate in the numerical situation has been kept constant with a value of three, so it will also be interesting to try different semi-aspect ratios.

- Although we do not expect substantial changes in the results with different profiles of the blades or sails, it could be possible to do a study of the aerodynamic of a cascade but using different flat plate shapes. What we have studied here can be considered as a first approximation for the optimal cascade configurations in terms of γ, σ, and ξ.

Regarding the second part of this thesis, we have worked with an hydraulic channel to see the surface variations on a sandy bottom generated by a single flat plate immersed in a tidal current, but obviously this work can be extended or improved to consider several other aspects:

- In order to validate and to be sure of the experimental results, we have started developing a numerical code to simulate the settling of sand in liquid media. But it needs more time to be improved and tuned for the characteristics of the hydraulic channel used here, so a future PhD student could continue with these tasks.

- Compare experimental and numerical results.

- Different sorts of sand, with different sizes and densities, could be tested.

- To use more than one flat plate to simulate the sand bed erosion of a real cascade of sails. Thus, one could optimize the distance from the flat plate to the sand bed in relation to the solidity and other characteristics of the cascade.

- The shape of the flat plate could be changed in order to know its influence on the erosion process.

Appendix A

APPENDIX: TURBULENCE MODELS

Two different turbulence models are used in this work: a RNG $k-\epsilon$ model, Yakhot *et al.* (1992) and a SST $k - \omega$ model, Menter (1994). In the RNG$-k - \epsilon$ model, the equation for the dissipation ϵ accounts for the different scales of motion through changes to the production term, while the equation for the kinetic energy k does not differ from that of the standard $k - \epsilon$ model, Rodi (2000) and Cebeci (2004). For a constant density flow,

$$\frac{\partial k}{\partial t} + \nabla \cdot (k\mathrm{v}) = \nabla \cdot [(\nu + \frac{\nu_t}{\sigma_k})\nabla k] + P_k - \epsilon, \qquad (A.1)$$

$$\frac{\partial \epsilon}{\partial t} + \nabla \cdot (\epsilon\mathrm{v}) = \nabla \cdot [(\nu + \frac{\nu_t}{\sigma_\epsilon})\nabla \epsilon] + C_{1\epsilon}\frac{\epsilon}{k}P_k - C_{2\epsilon}^{*}\frac{\epsilon^2}{k}. \qquad (A.2)$$

In this model, the kinematic eddy viscosity is given by

$$\nu_t = C_\mu \frac{k^2}{\epsilon}. \qquad (A.3)$$

The energy production term is

$$P_k = \nu_t S^2, \tag{A.4}$$

with $S = \sqrt{2\mathrm{S} : \mathrm{S}}$, the modulus of the mean rate-of-strain tensor, $\mathrm{S} = [\nabla \mathrm{v} + (\nabla \mathrm{v})^T]/2$, and

$$C_{2\epsilon}^* = C_{2\epsilon} + \frac{C_\mu \eta^3 (1 - \eta/\eta_0)}{1 + \beta \eta^3}, \eta = \frac{Sk}{\epsilon}. \tag{A.5}$$

For the nondimensional constants in the above expressions we use the following common values, which differ from those commonly used in the standard $k - \epsilon$ model, Yakhot *et al.* (1992) and Cebeci (2004): $C_\mu = 0.0845$, $\sigma_k = \sigma_\epsilon = 0.7194$, $C_{1\epsilon} = 1.42$, $C_{2\epsilon} = 1.68$, $\eta_0 = 4.38$, and $\beta = 0.012\mathrm{S}$.

The SST$-k - \omega$ model is directly usable all the way down to the wall through the viscous sub-layer without any extra damping functions, being more appropriate than the $k - \epsilon$ model for low Reynolds number turbulence, and is equivalent to a $k - \epsilon$ model in the free-stream, avoiding the common $k - \omega$ problem that the model is too sensitive to the inlet free-stream turbulence properties, Cebeci (2004) and Menter (1994). The maximum of the kinematic eddy viscosity, which in the standard $k - \omega$ model is given by $\nu_t = k/\omega$, is limited by forcing the turbulent shear stress to be bounded,

$$\nu_t = \frac{a_1 k}{\max(a_1 \omega, S F_2)}, \tag{A.6}$$

where $a_1 = 0.31$ and F_2 is an auxiliary function of the wall distance y given by

$$F_2 = \tanh \left\{ \left[\max \left(\frac{2\sqrt{k}}{\beta^* \omega y}, \frac{500\nu}{y^2 \omega} \right) \right]^2 \right\}. \tag{A.7}$$

The equations for the turbulent kinetic energy k and the specific dissipation rate ω can be written, for a constant density flow, as

$$\frac{\partial k}{\partial t} + \nabla \cdot (k\mathrm{v}) = \nabla \cdot [(\nu + \sigma_k \nu_t)\nabla k] + P_k - \beta^* k\omega, \qquad (A.8)$$

$$\frac{\partial \omega}{\partial t} + \nabla \cdot (\omega \mathrm{v}) = \nabla \cdot [(\nu + \sigma_\omega \nu_t)\nabla \omega] + \alpha S^2 - \beta \omega^2 + 2(1 - F_1)\sigma_{\omega 2}\frac{1}{\omega}\nabla k \cdot \nabla \omega, \; (A.9)$$

where now

$$P_k = \min(\nu_t S^2, 10\beta^* k\omega), \qquad (A.10)$$

and $\beta^* = 9/100$,

$$F_1 = \tanh\left\{\left\{\min\left[\max\left(\frac{\sqrt{k}}{\beta^* \omega y}, \frac{500\nu}{y^2 \omega}\right), \frac{4\sigma_{\omega 2}k}{CD_{k\omega}y^2}\right]\right\}^4\right\}, \qquad (A.11)$$

$$CD_{k\omega} = \max\left(2\sigma_{\omega 2}\frac{1}{\omega}\nabla k \cdot \omega, 10^{-10}\right). \qquad (A.12)$$

If we denote any of the model coefficients β, α, σ_k, and σ_k as ϕ, they are defined by blending the coefficients of the original $k - \omega$ model, denoted as ϕ_1, with those of the transformed $k - \epsilon$ model, denoted as ϕ_2, through

$$\phi = F_1 \phi_1 + (1 - F_1)\phi_2, \qquad (A.13)$$

The specific values of the non-dimensional parameters used here are, Menter (1994): $\alpha_1 = 5/9$, $\alpha_2 = 0.44$, $\beta_1 = 3/40$, $\beta_2 = 0.0828$, $\sigma_{k1} = 0.85$, $\sigma_{k2} = 1$, $\sigma_{\omega 1} = 0.5$, and $\sigma_{\omega 2} = 0.856$.

In Sec. 2.3 we selected the upstream values of k, ϵ and ω for each model that best fit the experimental data for an isolated plate, but we used the common values of the turbulence model constants given above.

In relation to the boundary conditions on the plate walls, we used several standard wall functions (see, e.g., Pope (2000)) implemented in the OPEN-FOAM toolbox. In particular, these boundary conditions are applied at a distance to the wall $y = y_p$ in the log-law region where y^+ is around 50, where $y^+ \equiv y/(\nu/u_*)$ is the distance to the wall in wall units. They are

$$\frac{\partial k}{\partial y}|_{y=y_p} = 0, \epsilon = \epsilon_p = \frac{C_\mu^{3/4} k_p^{3/2}}{\kappa y_p}, \omega = \omega_p = \sqrt{\omega_{vis}^2 + \omega_{log}^2}, \qquad (A.14)$$

$$\omega_{vis} = \frac{6\nu}{\beta y_p^2}, \omega_{log} = \frac{k_p^{1/2}}{C_\mu^{1/4} \kappa y_p}, \qquad (A.15)$$

with $k_p = k$ at $y = y_p$, and $\kappa = 0.41$ the von Kármán constant. In our computations with the medium mesh (e.g., case 6 in Table 2.1), the minimum value of y^+ was 0.1 and its medium value for the wall grid cells was 3.1. The corresponding minimum cell area in a constant z plane was $3.1 \times 10^{-6} c^2$, where c is the chord length.

Appendix B

APPENDIX: Code to select matched points and transform image

The selection of the matched points is an important task to carry out when an image seen by a camera with a certain angle must be projected to the vertical plane. Matlab has different libraries that can help us with this task and it is possible to transform an image in a few lines of code:

```
% get the pattern in the first line pattern1
im=imread(pattern1.path);
% get the real pattern with the points aligned to
% the horizontal and vertical
imRealPattern=imread(imRealPattern.path);

%display both image and match points in common
[inputPoints,basePoints]=cpselect(im(:,:,3),imRealPattern,'Wait',true);
set(gcf,'units','normalized','outerposition',[0 0 1 1]);
```

```
% Calculation of the second order transformation matrix
t=cp2tform(inputPoints,basePoints,'polynomial',2);%


% the transformation matrix is assigned to both pattern objects
pattern1.data.t =t;
pattern2.data.t =t;


% projection of the image in horizontal and vertical plane
fototrans_t=imtransform(im,t);
fototrans_t2=imtransform(im2,t);


% the horizontal and vertical image is assigned to both pattern objects
pattern1.data.fototrans_t =fototrans_t;
pattern2.data.fototrans_t =fototrans_t2;


%display the result
subplot(121)
imshow(im);
subplot(122)
imshow(fototrans_t)
set(gcf,'units','normalized','outerposition',[0 0 1 1]);
```

Once the matching of the points for the first pattern is done, then the same code will be loaded again for the second pattern.

Finally it is necessary to know the pixel-mm ratio from both patterns.

```
imshow(pattern1.data.fototrans_t)
```

```
set(gcf,'units','normalized','outerposition',[0 0 1 1]);
prompt={'Known distance in mm:',...
   'Number of iteration to calculate the average:'};
name='Get relation pixel/mm';
numlines=1;
defaultanswer={'2.5','3'};


answer=inputdlg(prompt,name,numlines,defaultanswer);
distPoints=str2num(answer{1});
d=str2num(answer{2});


j=1;
zoom on
uiwait(msgbox('Select HORIZONTAL known points',...
   'Get relation pixel/mm'));


for i2=d:-1:1,
    [x,y]=ginput22(2,'KeepZoom','k*');
    r=abs(x(2)-x(1));
    rel(j)=distPoints/r;
    j=j+1;
end
uiwait(msgbox('Select VERTICAL known points',...
   'Get relation pixel/mm'));


for i2=d:-1:1,
```

```
    [x,y]=ginput22(2,'KeepZoom','k*');

    r=abs(y(2)-y(1));

    rel(j)=distPoints/r;

    j=j+1;

end

close all


%relacXY is the pixel/mm ratio for the XY plane

relacXY=mean(rel);

desv=std(rel);

pattern1.data.relacXY = relacXY;

data=pattern1.data;

%save in a file

save(matfile,'data');
```

Finally when it is known the ratio from the two patterns, it can be calculated for whatever line in the spanwise direction:

```
%Parameters to calculate the relaction pixel/mm for whatever

%line using the equation relacXY=A+Bx

A=pattern1.data.relacXY;

B=(pattern2.data.relacXY-pattern1.data.relacXY)/pattern2.data.pos;
```

Appendix C

APPENDIX: Code to automatically select the lines in an image

The next code is used in the software to automatically select lines.

```
% get the image with the projected lines
im=imread(resultImage.path);


% ask for the filter parameters
prompt={'First intensity for the filter:',...
   'Pixel to be removed in isolated objects:'};
name='Select filter parameters';
numlines=2;
defaultanswer={num2str(i1),num2str(i2)};


answer=inputdlg(prompt,name,numlines,defaultanswer);
```

```
i1=str2num(answer{1});%First intensity for the filter
i2=str2num(answer{2});%Pixel to be removed in isolated objects

%first filter
%convert to gray
I=rgb2gray(im);


se = strel('disk',i1);
tophatFiltered = imtophat(I,se);
I = imadjust(tophatFiltered);

% Second filter
background = imopen(I,strel('disk',i1));

% Display the Background Approximation as a Surface
figure, surf(double(background(1:8:end,1:8:end))),zlim([0 255]);
set(gca,'ydir','reverse');


I2 = I - background;


I3 = imadjust(I2);

% Remove all objects in the image containing fewer pixels than i2 pixel
level = graythresh(I3);
im_bw = im2bw(I3,level);
```

```
im_bw = bwareaopen(im_bw, i2);


%paint in different color the bodies
cc = bwconncomp(im_bw, 4);
labeled = labelmatrix(cc);
Lrgb = label2rgb(labeled, @lines, 'c', 'shuffle');


%show the result
close all;
imshow(Lrgb)
title(textTitle);
set(gcf,'units','normalized','outerposition',[0 0 1 1])
```

Appendix D

APPENDIX: Code to calculate the points of a line using an image

The next code calculates the points of the lines using the curves generated in an image format.

```
% im is the projected image with a single line
im=curva.im_sel_proj;


% relacXY is the pixel-mm ratio in the XY plane
relacXY=curva.relacXY;


% xsol, ysol and zsol are the set of points for all the curves
xsol=[];
ysol=[];
zsol=[];
% errorsol is the error done by the line thick
errorsol=[];
% firstX is the value of the first pixel seen in the x-axis
```

```
firstX = -1;
% relfirstY is the position of the pixel where y must be 0
relfirstY=-1;
% loop to analyze all the pixel of the image
for x = 1:size(im,2)
    % retrieve an array with all the pixels where there is
    % part of the line
    y=find(im(:,x)==1);
    if isempty(y)==0
if firstX==-1
    % first time to retrieve an x value
    firstX=x;
end
%xsol is added to the array of x values, and calculate x
% as the different between the origin pixel and the current
% pixel
xsol=[xsol;(x-firstX)*relacXY];
%y is calculated with the mean value between the highest y pixel
% position and the lowest y pixel position
y1=min(y);
y2=max(y);
y=(size(im,1)-mean([y1 y2]))*relacXY;
% first curve and value found for y in order to take it as
% reference and draw the curves for this value.
if firstY==-1
    firstY=y;
end
```

```
if relfirstY==-1
     relfirstY=firstY-y;
end
y=y+relfirstY-firstY;
ysol=[ysol;y];
%zsol is calculated using the position of the current line
% in the z-axis
zsol=[zsol;(curva.pos-1)*Zplane.distZ+Zplane.ZeroPoint];
%error
error=(y2-y1)/2;
errorsol=[errorsol;error*relacXY];
     end
end
% smoothing the curve
fo = fitoptions('method','SmoothingSpline','SmoothingParam',.1);
ft = fittype('smoothingspline');
% fitting with the mean value
cf1 = fit(xsol,ysol,ft,fo);
% fitting with the min and max value
cf2 = fit([xsol;xsol],[ysol-errorsol;ysol+errorsol],ft,fo);

% obtaining the height (y coordinate) from the fitting curve for each
% x coordinate value
ysoli=cf1(xsol);
xyz = [xsol ysoli zsol errorsol];
```
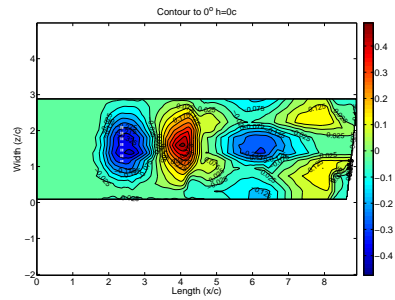
Appendix E

APPENDIX: Other figures

related to Chapter 4

In this Appendix all the 3D reconstructed surfaces will be shown for $\alpha =0^o$, 30°, 45° and 60°.
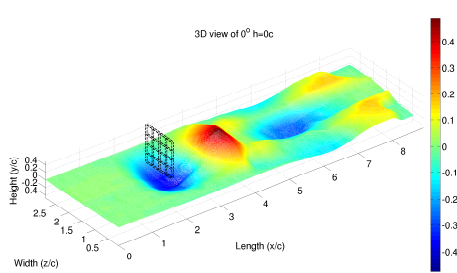
(a) $h = 0c$ (b) $h = 0c$

Figure E.1: Reconstructed 3D picture and contour of the surface for $\alpha = 0^o$ at $h = 0c$

(a) $h = 0.1c$

(b) $h = 0.1c$

(c) $h = 0.2c$

(d) $h = 0.2c$

(e) $h = 0.3c$

(f) $h = 0.3c$

(g) $h = 0.4c$

(h) $h = 0.4c$

Figure E.2: Reconstructed 3D pictures and contours of the surface for $\alpha = 0^{\circ}$ and from $h = 0.1c$ to $0.4c$

(a) $h = 0.5c$

(b) $h = 0.5c$

(c) $h = 0.6c$

(d) $h = 0.6c$

(e) $h = 0.7c$

(f) $h = 0.7c$

(g) $h = 0.8c$

(h) $h = 0.8c$

Figure E.3: Reconstructed 3D pictures and countours of the surface for $\alpha = 0^{\mathrm{o}}$ and from $h = 0.5c$ to $0.8c$

(a) $h = 0c$

(b) $h = 0c$

(c) $h = 0.1c$

(d) $h = 0.1c$

(e) $h = 0.2c$
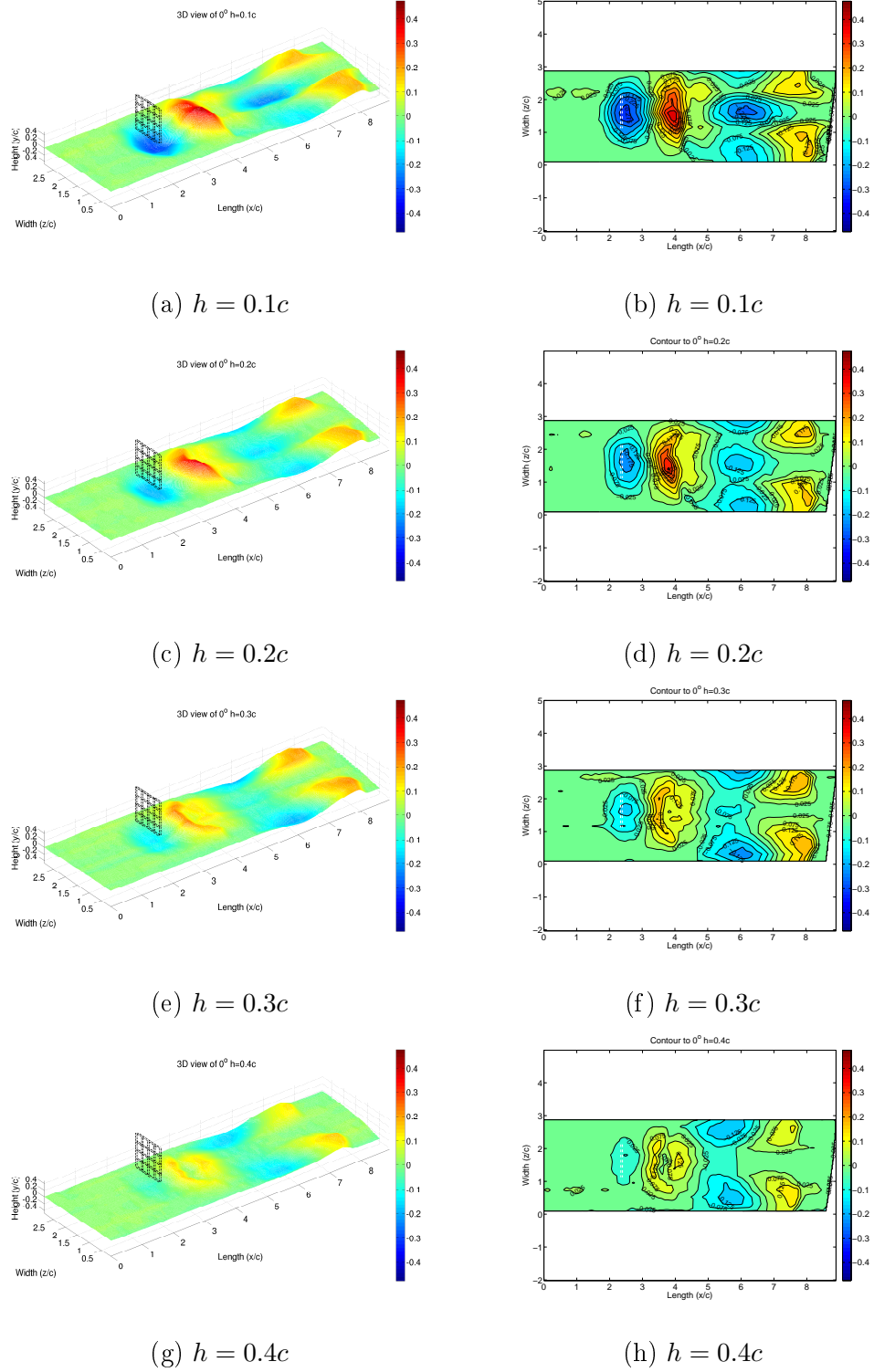

(f) $h = 0.2c$

(g) $h = 0.3c$

(h) $h = 0.3c$

Figure E.4: Reconstructed 3D pictures and contours of the surface for $\alpha = 30^{\circ}$ and from $h = 0c$ to $0.3c$
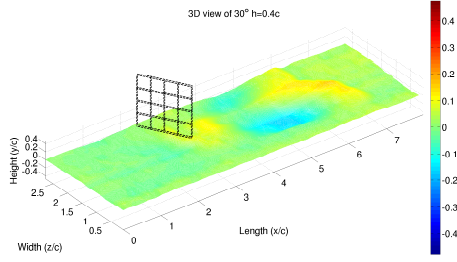
(a) $h = 0.4c$
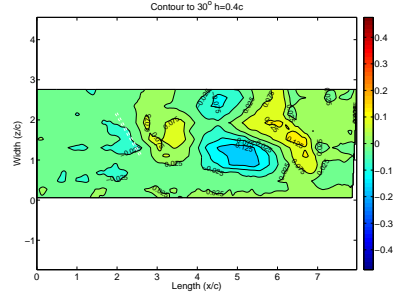
(b) $h = 0.4c$
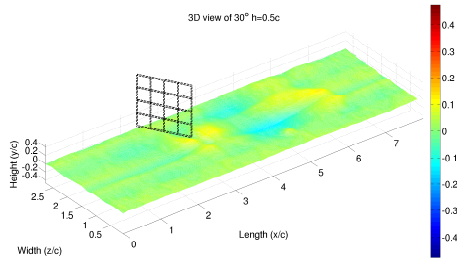
(c) $h = 0.5c$
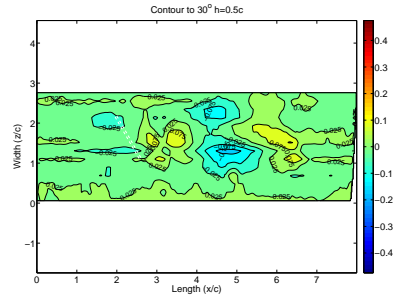
(d) $h = 0.5c$
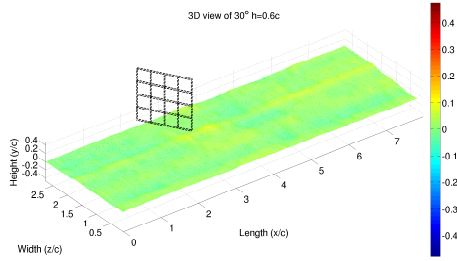
(e) $h = 0.6c$
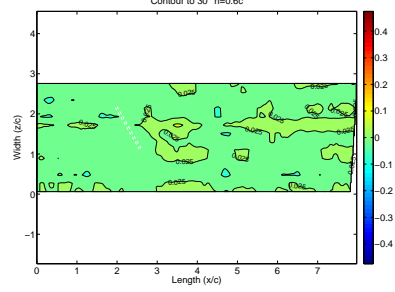
(f) $h = 0.6c$

Figure E.5: Reconstructed 3D pictures and contours of the surface for $\alpha = 30^{\circ}$ and from $h = 0.4c$ to $0.6c$
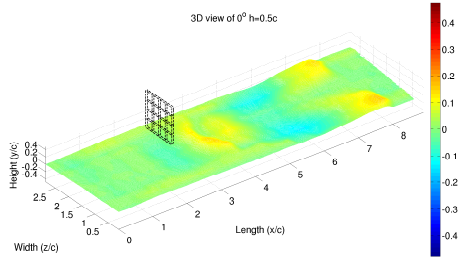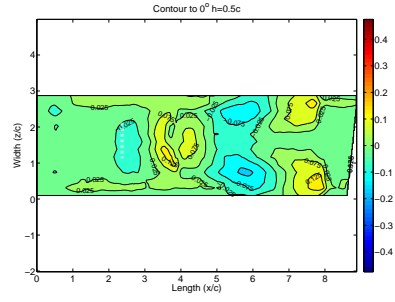
(a) $h = 0c$

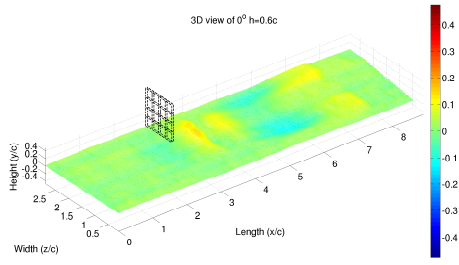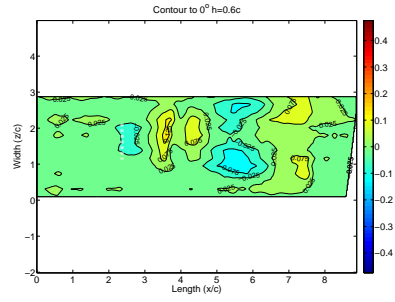(b) $h = 0c$

(c) $h = 0.1c$

(d) $h = 0.1c$

(e) $h = 0.2c$

(f) $h = 0.2c$
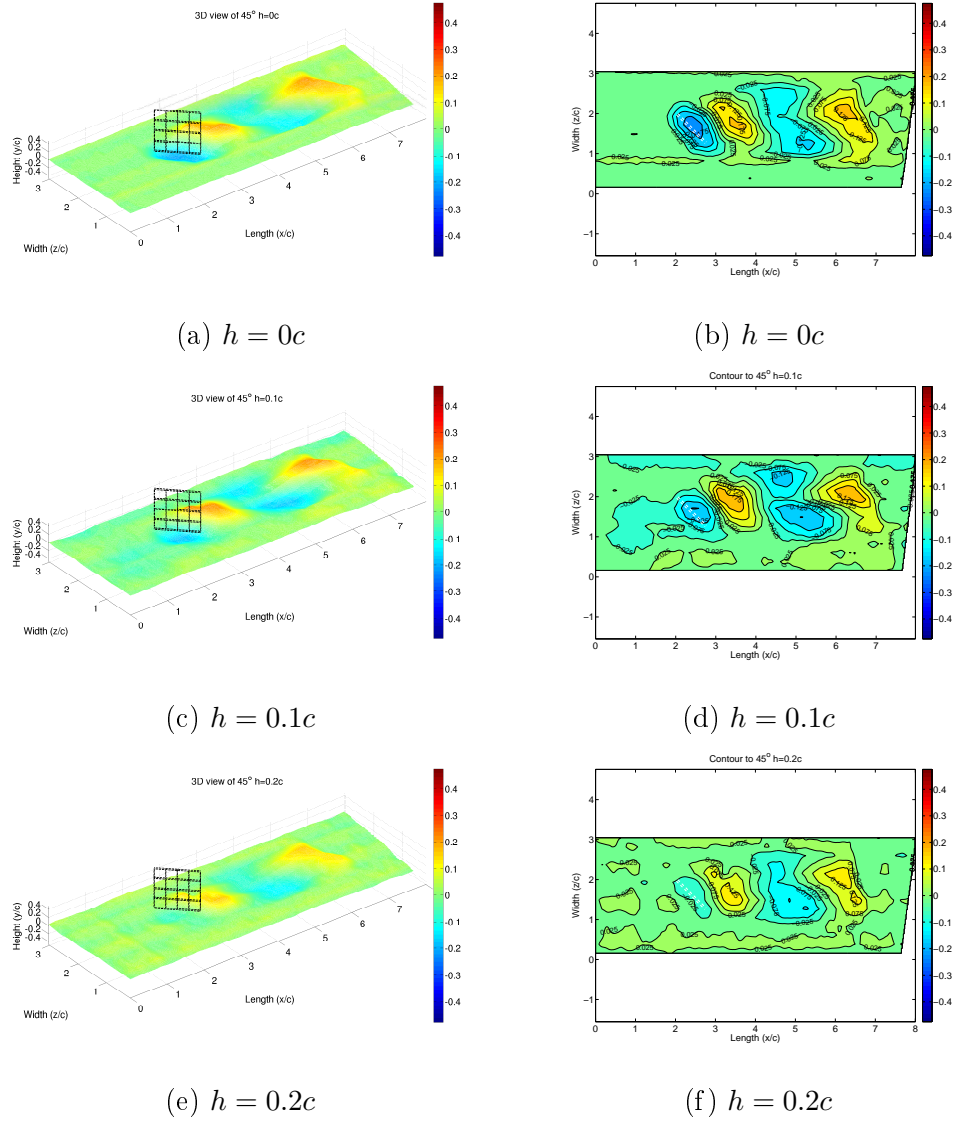
Figure E.6: Reconstructed 3D pictures of the surface for $\alpha = 45°$ and from $h = 0c$ to $0.2c$
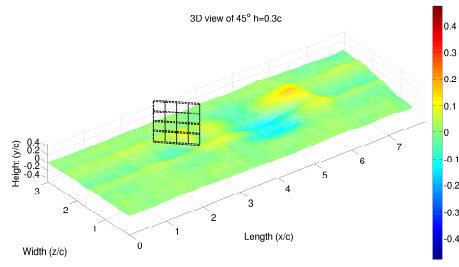
(a) $h = 0.3c$
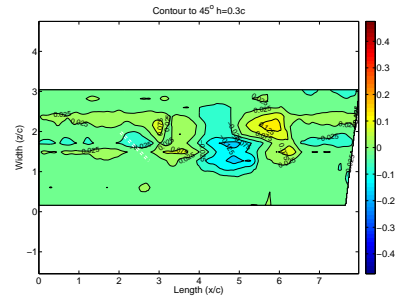
(b) $h = 0.3c$
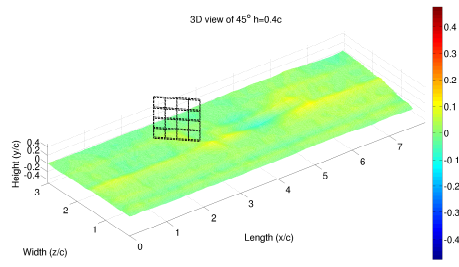
(c) $h = 0.4c$
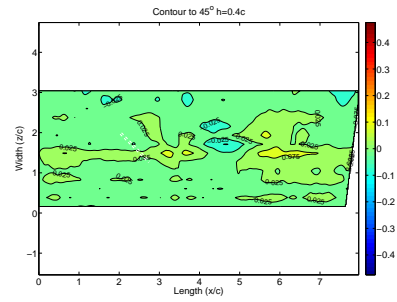
(d) $h = 0.4c$
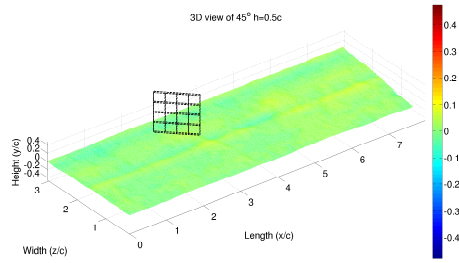
(e) $h = 0.5c$
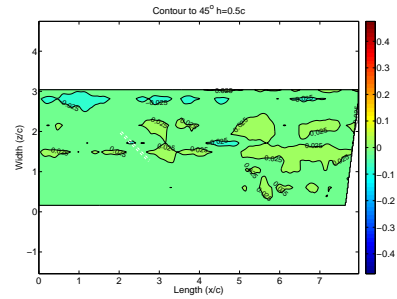
(f) $h = 0.5c$

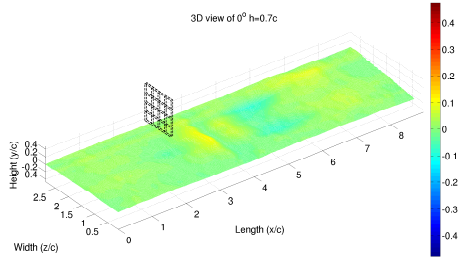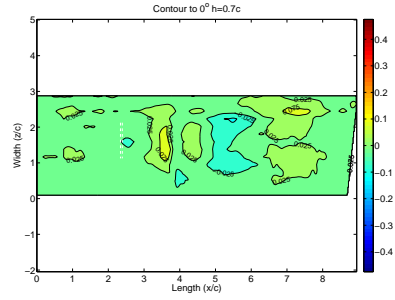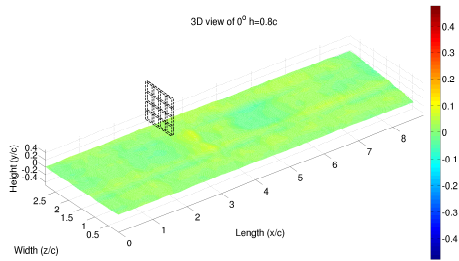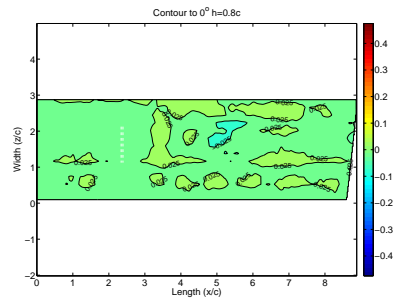Figure E.7: Reconstructed 3D pictures of the surface for $\alpha = 45^{\circ}$ and from $h = 0.3c$ to $0.5c$

(a) $h = 0c$

(b) $h = 0c$

(c) $h = 0.1c$

(d) $h = 0.1c$

(e) $h = 0.2c$

(f) $h = 0.2c$
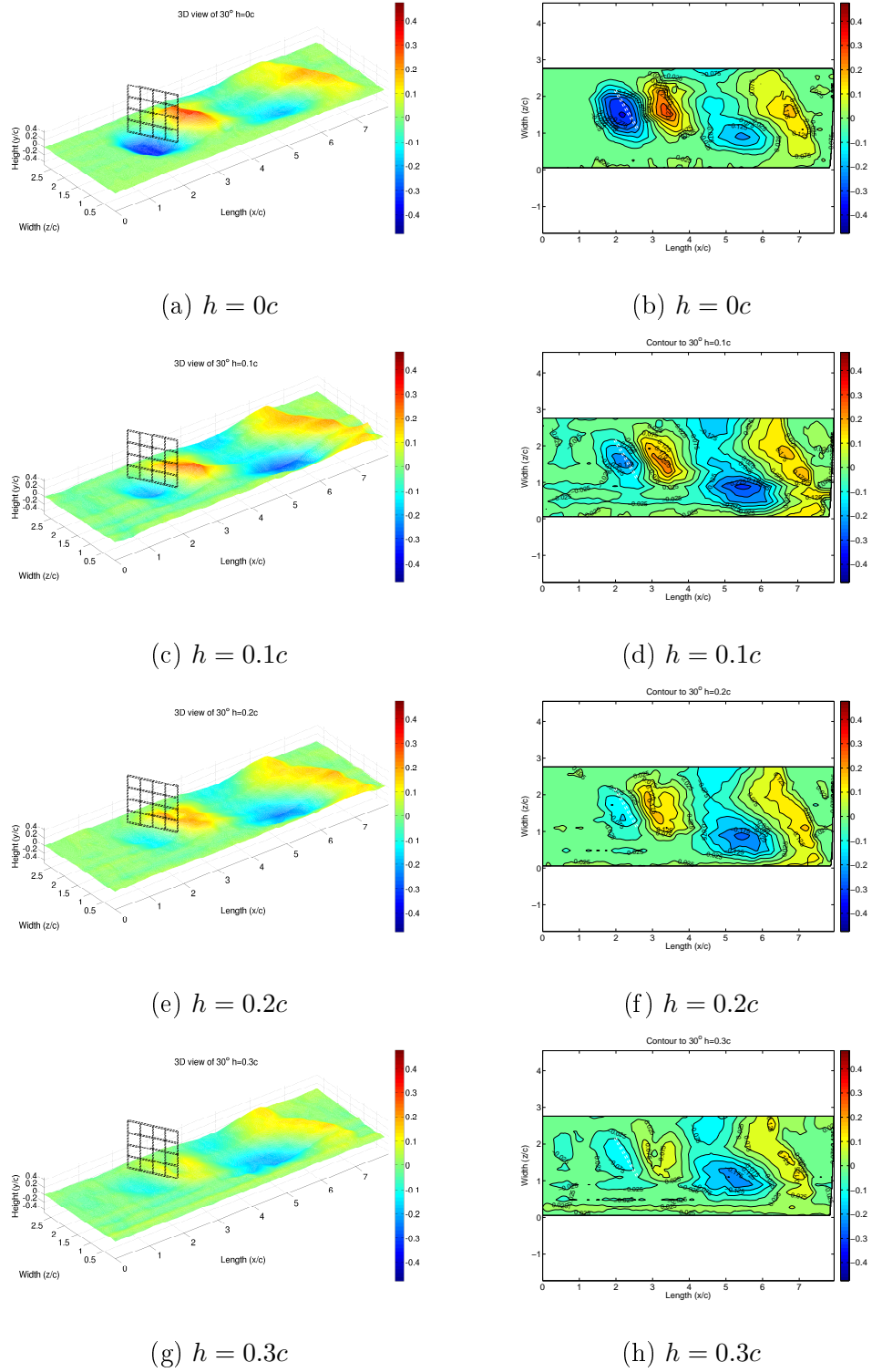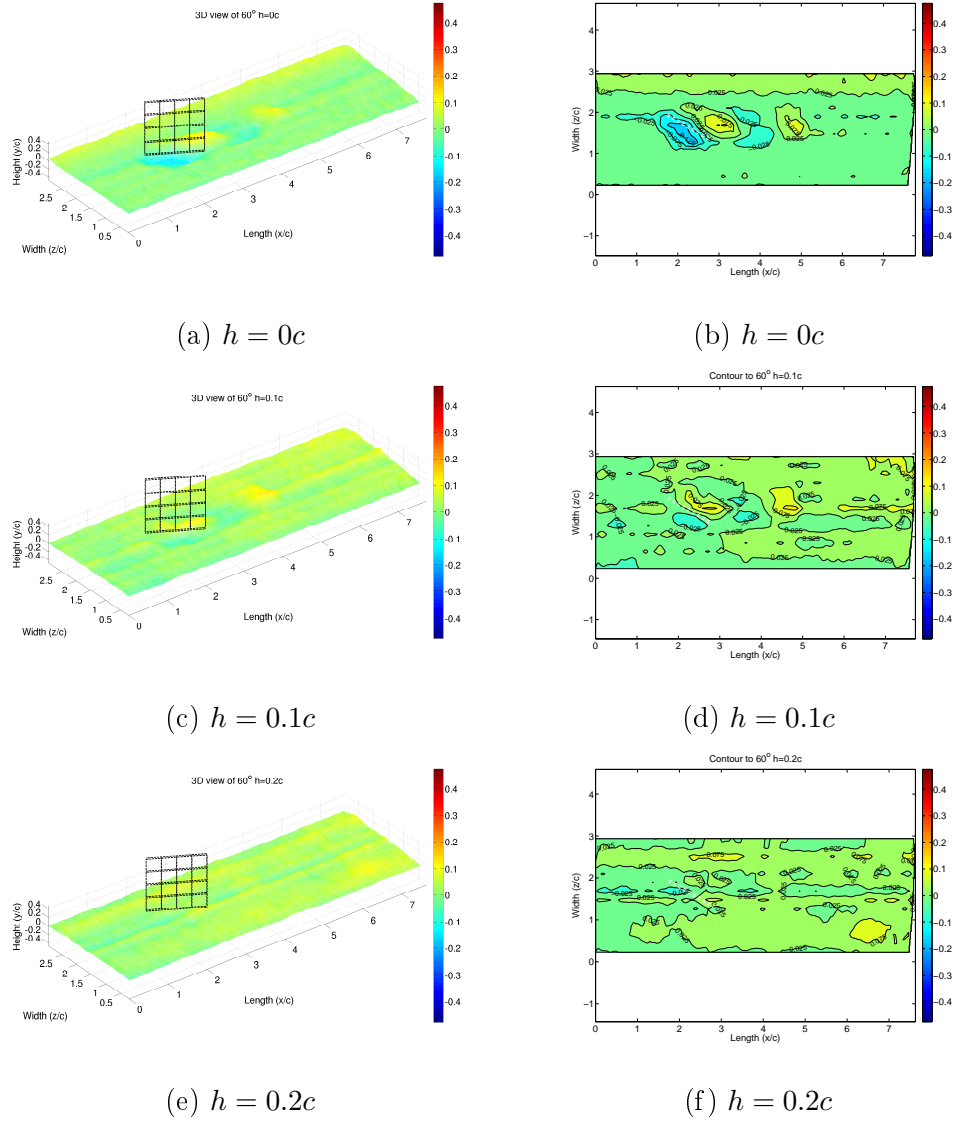
Figure E.8: Reconstructed 3D pictures of the surface for $\alpha = 60^{\circ}$ and from $h = 0c$ to $0.2c$

Appendix F

# APPENDIX: Resumen extendido

F.1   Introducción

Las energías marinas tienen un importantísimo papel en las energías renovables debido a que cerca del 71% de la superficie de la tierra está cubierta de agua, y los océanos poseen cerca del 96.5% del agua de toda la tierra (U.S. Geological Survey, 2014). Además, el vasto océano posee una energía suficiente para abastecer la demanda energética en el mundo con mucha mayor longevidad que otras fuentes energéticas como las fósiles (Pelc & Fujita, 2002). En este trabajo se pretende contribuir a las investigaciones que se están realizando actualmente sobre energías renovables y su obtención a partir de las corrientes de las mareas.

En este contexto, una empresa Noruega ha desarrollado un aparato sin turbina que consiste en un conjunto de velas dispuestas en cascada que se mueven con la corriente en una dirección establecida (ver Fig. 1.1) para finalmente generar electricidad (TidalSail S.A., 2014). Las velas están unidas a un raíl que las soporta y les permite el movimiento en una dirección, como se muestra en Fig. 1.2. Además, el raíl posee tres lados creando un triángulo

equilátero con amarradero en cada esquina (ver Fig. 1.3 para más detalles), de modo que es más eficiente con menor espacio. El sistema tiene características que lo hacen ventajoso con respecto a otros dispositivos similares para la captura de energía de las corrientes, tales como (ver TidalSail S.A., 2014, para más detalles):

- Las velas tienen un movimiento lo suficientemente lento que minimizan el impacto sobre la fauna marina. Un problema que poseen los dispositivos con turbinas.

- Optimizan su diseño; y por ello, es posible conseguir más potencia de la corriente con menor área. Además, la planta de producción es equivalente a 30 turbinas convencionales con un movimiento lento.

- El sistema es invisible para el ser humano y no posee por ello un impacto visual.

- El peso del dispositivo frente a la producción de energía es mucho menor que otros sistemas.

- Las partes móviles del dispositivo del aparato tienen tratamientos anticorrosivos y lubricantes que no dañan el medio ambiente.

- Las velas se auto-limpian, se auto-ajustan y operan muy lentamente.

- Esta estructura compactada permite extraer energía no solo del mar sino de los ríos.

En nuestro estudios se ha elegido este dispositivo de captación de energía de las mareas para estudiar la mejor configuración del mismo, tratando de generar la mayor potencia posible, sin erosionar el fondo marino y evitando dañar el medio ambiente (TidalSail S.A., 2014, ver). Para ello, y en una

primera parte, se ha estudiado la aerodinámica de las velas usadas en el mencionado dispositivo. El flujo de estudio es considerado incompresible con una corriente de entrada uniforme de velocidad $\mathbf{V}$ a través de una cascada de placas planas rectangulares de longitud de cuerda c y altura b moviéndose a una velocidad $\mathbf{U}$ perpendicular a la corriente $\mathbf{V}$ (ver Fig. 2.1(a)). La separación entre las placas paralelas es s y su ángulo de incidencia γ. Para las simulaciones numéricas es conveniente usar un marco de referencia que se mueva con las placas, en cuyo eje x coincide con la dirección de la velocidad relativa $\mathbf{W}$ (Fig. 2.1(b)). En este marco de referencia, el ángulo de ataque efectivo en relación a la velocidad relativa es $\alpha = \gamma - \theta$, donde θ es el ángulo entre la velocidad de la corriente $\mathbf{V}$ y la velocidad relativa $\mathbf{W}$.

Se ha fijado un número de Reynolds a $Re = 5.66 \times 10^4$ y una semi-relación de aspecto $sAR = 3$. El estudio de la aerodinámica de las velas se ha llevado a cabo mediante un código numérico que ha permitido realizar las simulaciones turbulentas, comparando una única vela con los resultados experimentales de Pelletier & Mueller (2000) y así validar y ajustar los parámetros turbulentos a la entrada. Para esta ejercicio se ha utilizado los resultados arrojados por dos modelos turbulentos: un modelo "Re-Normalisation Group" (RNG) $k - \epsilon$ y el modelo " Shear Stress Transport" (SST) $k - \omega$. De los dos, el $k - \omega$ se ha ajustado mejor a los datos experimentales, por lo que ha sido finalmente usado para simulaciones posteriores. Así, la validación del código numérico ha permitido que se pueda emplear para estudiar un tren de velas infinito, en forma de cascada, y analizar la mejor configuración aerodinámica del conjunto.

El trabajo llevado a cabo en la segunda parte de la tesis se ha centrado en estudiar experimentalmente la erosión que sobre un fondo arenoso producen las placas planas en un canal hidráulico; y con ello, buscar el efecto que la

separación entre las velas y el fondo pueden producir en la arena, y disponer de un conocimiento que nos permita tomar las mejores decisiones para producir el menor impacto ambiental. Para esto, el número de Reynolds ha sido fijado al máximo según nos permitía el propio canal hidráulico. Este posee unas dimensiones muy pequeñas y no permite utilizar técnicas estándares de reconstrucción de la superficie erosionada, ya sea porque introducen objetos en un espacio limitado, requieren de licencias muy caras, no tienen en cuenta la refracción de la luz o porque pueden distorsionar el resultado final. Por este motivo, se ha diseñado una metodología y realizado un código en Matlab que permite salvar estas dificultades y que, mediante patrones de formas conocidas y una serie de líneas paralelas proyectadas sobre la superficie erosionada a reconstruir, se obtiene la forma de dicha superficie sumergida en dimensiones reales. Gracias a las imágenes tomadas y al procesado de las mismas, se pueden obtener diversos resultados, como: el calculo de la cantidad de arena en unidad de volumen que se erosiona, la forma de las dunas que se generan, las curvas de nivel del fondo, la reconstrucción 3D de la superficie sumergida y los perfiles de la superficie en diferentes planos.

El método propuesto para la reconstrucción 3D de superficies sumergidas consiste, principalmente, en una técnica para la reconstrucción de superficies sumergidas mediante la transformación de un conocido patrón de puntos y una series de líneas proyectadas sobre la superficie a escanear. Primero, el patrón es colocado en la línea proyectada más cercana a la cámara y se toma una foto, Fig. 3.1(a). Se toma una segunda foto del patrón colocado en una línea diferente, ver Fig. 3.1(b). Es importante remarcar que durante los diferentes pasos de la metodología la cámara no puede moverse. Una vez las imágenes de los patrones han sido tomadas con un cierto ángulo entre la cámara y la horizontal, estas son procesadas en un ordenador usando

el mismo patrón de puntos, pero con todos los puntos alineados horizontal
y verticalmente, Fig. 3.1(d). Entonces, un grupo de puntos en común se
seleccionan entre las dos imágenes. Como resultado de la unión de los puntos, esta metodología permite aplicar una transformación de segundo orden,
dando como resultado una matriz de transformación que se utiliza sobre la
imagen de las líneas proyectadas en la arena para obtener en magnitud real
la superficie 3D.

Desde un punto de vista metodológico, el proyecto de tesis doctoral ha
utilizado el método anterior expuesto para calcular la altura de la placa plana
con respecto al fondo arenoso h y el ángulo de esta placa plana con respecto
a la corriente α. Realizando variaciones para minimizar la erosión producida
en el fondo marino, con valores constantes del número de Reynolds máximo
permitido por el canal hidráulico y el mismo ancho de la placa plana con un
único tipo de arena.

F.2   Conclusiones

Durante todo el proyecto de la tesis doctoral hemos centrado el esfuerzo en
mejorar la aerodinámica de un dispositivo de captación de energía de corrientes de marea o fluvial, y en la última parte se ha buscado mitigar el
impacto ambiental sobre el fondo arenoso de la zona en la que está el dispositivo. Siguiendo estas motivaciones se han obtenido los siguientes resultados
que son también explicados ampliamente en los respectivos capítulos de esta
tesis:

- Se han realizado simulaciones numéricas de un modelo simplificado del
  aparato de captación de energía de corrientes consistente en una cascada de placas planas moviéndose perpendicular a la corriente. En

los experimentos se ha mantenido constante el número de Reynolds de la corriente y la semi-relación de aspecto sAR de las placas planas se mantiene constante a $sAR = 3$. Sin embargo, se ha ido variando la separación relativa entre placas σ y el ángulo de ataque de las mismas relativo a la corriente α. Para ello, se han ido ajustando los parámetros turbulentos del modelo con los que mejor reproducían los resultados experimentales de una placa plana. Y además, tras un estudio de convergencia de malla, se ha encontrado el número de celdas óptimo para realizar las simulaciones de manera eficiente.

- Para la configuración anterior se ha encontrado un resultado óptimo que permite obtener máxima potencia $\overline{C}_P$ cuando el ángulo de ataque tiene un valor aproximado de $\gamma \approx 79º$, la compactación o separación entre las placas es $\sigma \approx 1$, y la velocidad de las velas con respecto a la corriente es $\xi \approx 2.5$. Sin embargo, aparece un segundo valor máximo de $\overline{C}_P$ ligeramente más pequeño para $\sigma \approx 1$, $\gamma \approx 75º$ y $\xi \approx 1.5$. Este último valor hace mucho más interesante la configuración de las placas planas en cascada porque, para igual valor de potencia en los dos máximos, se emplea un menor número de placas planas, reduciendo costes y espacio. En cualquier caso, la compactación óptima está cerca de la unidad, siendo el mejor ángulo de ataque aproximadamente 75º.

- Para poder analizar la superficie erosionada por las placas planas ha sido necesario elaborar un método de cálculo y un programa en Matlab para reconstruir superficies en 3D. El método ha sido validado calculando las dimensiones de una concha marina, demostrándose que es válido para escanear superficies 3D con un error de precisión proporcional al grosor de las líneas. El error cometido no supera el valor de

1 mm en el ejemplo de validación. Además, se ha comprobado que es posible obtener los valores máximos y mínimos de la superficie relativos y/o absolutos, y calcular volúmenes de diferentes regiones.

- Se ha usado un canal hidráulico para simular la erosión producida por una placa plana y la corriente, utilizándose un valor del número de Reynolds fijo para diferentes alturas de la placa plana con respecto al fondo marino, y diferentes ángulos de la misma con respecto a la corriente. Dos tipos de fenómenos se desarrollan en la erosión: el primero, aparece ocasionado por la corriente circulando por debajo de la placa plana y generando tres resultados: una primera erosión, una duna detrás, y una segunda erosión. A medida que se va aumentando la altura de la placa plana el volumen de erosión cae exponencialmente. Sin embargo, la altura de la primera duna que se genera lo hace de manera lineal. En un segundo fenómeno aparece debido a los vórtices que se originan en los laterales de la placa plana. Este segundo fenómeno es el último en desvanecerse, y conforme se gira el ángulo de la placa plana desaparece la tercera erosión que se produce en la parte trasera para ángulos con valores hasta 30°, fusionándose en dos erosiones, una por cada lateral de la placa plana.

F.3   Sugerencias para trabajos futuros

Por la amplitud de objetivos y aspectos abordados durante el proyecto de tesis realizado, a su conclusión nos encontramos con un amplio rango de posibilidades para continuar otras muchas investigaciones.

Con respecto a la aerodinámica del conjunto de placas planas formando una cascada se puede seguir trabajando en los siguientes puntos:

- Comparar los resultados numéricos con datos experimentales en un canal hidráulico para el mismo Reynolds que se ha usado en este trabajo.

- Probar diferentes Reynolds, para las mismas conclusiones que se han obtenido al variar la separación entre las velas, la velocidad del conjunto frente a la corriente y el ángulo de las placas planas con respecto a la corriente. De esta manera, se podría estudiar la diferencia respecto a usar Reynolds muy altos.

- La semi-relación de aspecto de la placa plana en las simulaciones numéricas se ha mantenido constante con un valor de 3, por lo que sería muy interesante probar diferentes semi-relaciones de aspecto.

- Aunque se espera que el resultado no varíe mucho con diferentes perfiles en lugar de placas planas, se podría hacer un estudio aerodinámico usando perfiles diferentes. En este trabajo se ha hecho una primera aproximación para la configuración óptima de una cascada de placas planas en términos de γ, σ, y ξ.

Con respecto a la erosión originada por las placas planas en el fondo marino se puede seguir trabajando en los siguientes puntos:

- Terminar la elaboración de un código numérico para simular la sedimentación, erosión y deposición de arena.

- Comparar los resultados experimentales de la segunda parte con las simulaciones numéricas que se pudieran realizar.

- Experimentar diferentes tipos de arena.

- Simular más de una placa plana y conocer dónde estaría la altura y el ángulo óptimo para una cascada de placas planas.

- Variar la forma de las placas planas para conocer su influencia sobre el proceso de erosión.

Bibliography

BRØRS, B. 1999 Numerical modeling of flow and scour at pipelines. *Journal of Hydraulic Engineering* **125** (5), 511–523.

BRUNO, F., BIANCO, G., MUZZUPAPPA, M., BARONE, S. & RAZIONALE, A.V. 2011 Experimentation of structured light and stereo vision for underwater 3d reconstruction. *{ISPRS} Journal of Photogrammetry and Remote Sensing* **66** (4), 508 – 518.

C., ROGER 2003 Sustainable co-generation from the tides: A review. *Renewable and Sustainable Energy Reviews* **7** (3), 187 – 213.

CAL, R.B., LEBRÓN, J., CASTILLO, L., KANG, H.S. & MENEVEAU, C. 2010 Experimental study of the horizontally averaged flow structure in a model wind-turbine array boundary layer. *Journal of Renewable and Sustainable Energy* **2** (1), 013106.

CEBECI, T. 2004 *Turbulence models and their application: efficient numerical methods with computer programs*. Springer.

CHIEW, Y. 1991 Prediction of maximum scour depth at submarine pipelines. *Journal of Hydraulic Engineering* **117** (4), 452–466.

DROEGE, P. 2008 Urban energy transition: An introduction. In *Urban Energy Transition* (ed. Peter Droege), pp. 1 – 14. Amsterdam: Elsevier.

122

FADAEENEJAD, M., SHAMSIPOUR, R., ROKNI, S.D. & GOMES, C. 2014 New approaches in harnessing wave energy: With special attention to small islands. *Renewable and Sustainable Energy Reviews* **29** (0), 345 – 354.

FEDOUL, F., PARRAS, L., DEL PINO, C. & FERNANDEZ-FERIA, R. 2014 Experimental study of the aerodynamic characteristics of a low-aspect-ratio flat plate array in a configuration of interest for a tidal energy converter. *Journal of Fluids and Structures* **48**, 487–496.

FERZIGER, J.H. & PERIĆ, M. 1996 *Computational methods for fluid dynamics*, , vol. 3. Springer Berlin.

GAO, F., YANG, B., WU, Y. & YAN, S. 2006 Steady current induced seabed scour around a vibrating pipeline. *Applied Ocean Research* **28** (5), 291–298.

GONZALEZ-JUEZ, E., MEIBURG, E. & CONSTANTINESCU, G. 2009 The interaction of a gravity current with a circular cylinder mounted above a wall: Effect of the gap size. *Journal of Fluids and Structures* **25** (4), 629–640.

GÜHRING, J. 2000 Dense 3d surface acquisition by structured light using off-the-shelf components. In *Photonics West 2001-Electronic Imaging*, pp. 220–231. International Society for Optics and Photonics.

HEIDE, D., VON BREMEN, L., GREINER, M., HOFFMANN, C., SPECK-MANN, M. & BOFINGER, S. 2010 Seasonal optimal mix of wind and solar power in a future, highly renewable europe. *Renewable Energy* **35** (11), 2483–2489.

IACCARINO, G., OOI, A., DURBIN, P.A. & BEHNIA, M. 2003 Reynolds averaged simulation of unsteady separated flow. *International Journal of Heat and Fluid Flow* **24** (2), 147–156.

JIA, Z., WANG, B., SONG, S. & FAN, Y. 2014 Blue energy: Current technologies for sustainable power generation from water salinity gradient. *Renewable and Sustainable Energy Reviews* **31** (0), 91 – 100.

KHAN, M.J., BHUYAN, G., IQBAL, M.T. & QUAICOE, J.E. 2009 Hydrokinetic energy conversion systems and assessment of horizontal and vertical axis turbines for river and tidal applications: A technology status review. *Applied Energy* **86** (10), 1823 – 1835.

KHOSRONEJAD, A., KANG, SEOKKOO & SOTIROPOULOS, FOTIS 2012 Experimental and computational investigation of local scour around bridge piers. *Advances in Water Resources* **37** (0), 73 – 85.

KOCAK, D.M. & CAIMI, F.M. 2005 The current art of underwater imaging– with a glimpse of the past and vision of the future. *Marine Technology Society Journal* **39** (3), 5–26.

KOUTSOUDIS, A., VIDMAR, B., IOANNAKIS, G., ARNAOUTOGLOU, F., PAVLIDIS, G. & CHAMZAS, C. 2014 Multi-image 3d reconstruction data evaluation. *Journal of Cultural Heritage* **15** (1), 73 – 79.

KRUMBEIN, W.C. & ABERDEEN, E. 1937 The sediments of barataria bay. *Journal of Sedimentary Research* **7** (1), 3–17.

LI, F. & CHENG, L. 1999 Numerical model for local scour under offshore pipelines. *Journal of Hydraulic Engineering* **125** (4), 400–406.

LIU, F. & ZHANG, D. 2014 3d fingerprint reconstruction system using feature correspondences and prior estimated finger model. *Pattern Recognition* **47** (1), 178 – 193.

LV, D., SUN, J., LI, Q. & WANG, Q. 2013 Point-based integration for 3d object reconstruction from ladar range images. *Optik - International Journal for Light and Electron Optics* **124** (23), 6318 – 6325.

MAO, Y. 1987 The interaction between a pipeline and an erodible bed. *SERIES PAPER TECHNICAL UNIVERSITY OF DENMARK* (39).

MATLAB 2014 http://www.mathworks.es/.

MELVILLE, B.W. & COLEMAN, S.E. 2000 *Bridge scour*. Water Resources Publication.

MENTER, F.R. 1994 Two-equation eddy-viscosity turbulence models for engineering applications. *AIAA journal* **32** (8), 1598–1605.

MERRIAM, D.F. 2003 Sedimentologists: William christian krumbein (1902–1979). In *Sedimentology*, pp. 1065–1066. Springer.

MUNRO, R.J. & DALZIEL, S.B. 2005 Attenuation technique for measuring sediment displacement levels. *Experiments in fluids* **39** (3), 602–613.

MUNRO, RJ, DALZIEL, SB & JEHAN, H 2004 A pattern matching technique for measuring sediment displacement levels. *Experiments in fluids* **37** (3), 399–408.

OPENFOAM 2014 http://www.openfoam.com.

OSSAI, C.I., BOSWELL, B. & DAVIES, I.J. 2014 Sustainable asset integrity management: Strategic imperatives for economic renewable energy generation. *Renewable Energy* **67** (0), 143 – 152.

PAVLIDIS, G., KOUTSOUDIS, A., ARNAOUTOGLOU, F., TSIOUKAS, V. & CHAMZAS, C. 2007 Methods for 3d digitization of cultural heritage. *Journal of Cultural Heritage* **8** (1), 93 – 98.

PELC, R. & FUJITA, R.M. 2002 Renewable energy from the ocean. *Marine Policy* **26** (6), 471 – 479.

PELLETIER, A. & MUELLER, T.J. 2000 Low reynolds number aerodynamics of low-aspect-ratio, thin/flat/cambered-plate wings. *Journal of Aircraft* **37** (5), 825–832.

POPE, S.B. 2000 *Turbulent flows*. Cambridge university press.

RAJAGOPALAN, K. & NIHOUS, G.C. 2013 Estimates of global ocean thermal energy conversion (otec) resources using an ocean general circulation model. *Renewable Energy* **50** (0), 532 – 540.

RICHARDSON, L.F. 1911 The approximate arithmetical solution by finite differences of physical problems involving differential equations, with an application to the stresses in a masonry dam. *Philosophical Transactions of the Royal Society of London. Series A, Containing Papers of a Mathematical or Physical Character* **210**, 307–357.

ROACHE, P.J. 1998 *Verification and validation in computational science and engineering*. Hermosa Albuquerque, NM.

ROC, T., GREAVES, D., THYNG, K.M. & CONLEY, D.C. 2014 Tidal turbine representation in an ocean circulation model: Towards realistic applications. *Ocean Engineering* **78** (0), 95 – 111.

ROCCHINI, C., CIGNONI, P., MONTANI, C., PINGI, P. & SCOPIGNO, R. 2001 A low cost 3d scanner based on structured light. In *Computer Graphics Forum*, , vol. 20, pp. 299–308. Wiley Online Library.

RODI, W. 2000 *Turbulence Models and Their Application in Hydraulics. A State-of-the-art Review*. CRC Press.

ROULUND, A., SUMER, B.M., FREDSØE, J. & MICHELSEN, J. 2005 Numerical and experimental investigation of flow and scour around a circular pile. *Journal of Fluid Mechanics* **534**, 351–401.

ROURKE, F.O., BOYLE, F. & REYNOLDS, A. 2010 Tidal energy update 2009. *Applied Energy* **87** (2), 398 – 409.

SAAD, Y. 2003 *Iterative methods for sparse linear systems*. Siam.

SAGAUT, P. & DRIKAKIS, D. 2010 Large eddy simulation. *Encyclopedia of Aerospace Engineering* .

SCHECHNER, Y.Y. & KARPEL, N. 2004 Clear underwater vision. In *Computer Vision and Pattern Recognition, 2004. CVPR 2004. Proceedings of the 2004 IEEE Computer Society Conference on*, , vol. 1, pp. I–536. IEEE.

SHIELDS, M.A., DILLON, L.J., WOOLF, D.K. & FORD, A.T. 2009 Strategic priorities for assessing ecological impacts of marine renewable energy devices in the pentland firth (Scotland, UK). *Marine Policy* **33** (4), 635 – 642.

SPALART, P.R. 2009 Detached-eddy simulation. *Annual Review of Fluid Mechanics* **41**, 181–202.

SUBHRA MUKHERJI, S., KOLEKAR, N., BANERJEE, A. & MISHRA, R. 2011 Numerical investigation and evaluation of optimum hydrodynamic performance of a horizontal axis hydrokinetic turbine. *Journal of Renewable and Sustainable Energy* **3** (6), –.

TIDALSAIL S.A. 2014 http://tidalsails.com.

U.S. GEOLOGICAL SURVEY 2014 How much water is there on, in, and above the earth?

VISUALFSM 2014 http://ccwu.me/vsfm/.

WEINIG, F.S. 1964 Theory of two-dimensional flow through cascades. *Aerodynamics of turbines and compressors* **10**, 13–82.

WESTOBY, M.J., BRASINGTON, J., GLASSER, N.F., HAMBREY, M.J. & REYNOLDS, J.M. 2012 'structure-from-motion' photogrammetry: A low-cost, effective tool for geoscience applications. *Geomorphology* **179** (0), 300 – 314.

WHITEHOUSE, R. 1998 *Scour at marine structures: A manual for practical applications*. Thomas Telford.

YAKHOT, V., ORSZAG, S.A., THANGAM, S., GATSKI, T.B. & SPEZIALE, C.G. 1992 Development of turbulence models for shear flows by a double expansion technique. *Physics of Fluids A: Fluid Dynamics (1989-1993)* **4** (7), 1510–1520.